

Automated Transverse Momentum Resummation for Electroweak Boson Production

Inauguraldissertation
der Philosophisch-naturwissenschaftlichen Fakultät
der Universität Bern

vorgelegt von

Monika Hager

von Zürich und Uster

Leiter der Arbeit:

Prof. Dr. Thomas Becher

Albert Einstein Center for Fundamental Physics
Institut für Theoretische Physik, Universität Bern

Originaldokument gespeichert auf dem Webserver der Universitätsbibliothek Bern



Dieses Werk ist unter einem
Creative Commons Namensnennung-Keine kommerzielle Nutzung-Keine Bearbeitung 2.5
Schweiz Lizenzvertrag lizenziert. Um die Lizenz anzusehen, gehen Sie bitte zu
<https://creativecommons.org/licenses/by-nc-nd/3.0/ch/> oder schicken Sie einen Brief an
Creative Commons, 171 Second Street, Suite 300, San Francisco, California 94105, USA.

Automated Transverse Momentum Resummation for Electroweak Boson Production

**Inauguraldissertation
der Philosophisch-naturwissenschaftlichen Fakultät
der Universität Bern**

vorgelegt von

Monika Hager

von Zürich und Uster

Leiter der Arbeit:

Prof. Dr. Thomas Becher

Albert Einstein Center for Fundamental Physics
Institut für Theoretische Physik, Universität Bern

Von der Philosophisch-naturwissenschaftlichen Fakultät angenommen.

Bern, 4. Juni 2019

**Der Dekan:
Prof. Dr. Z. Balogh**

UNIVERSITY OF BERN

Abstract

Faculty of Natural Sciences
Institut für Theoretische Physik, Universität Bern

Inauguraldissertation der Philosophisch-naturwissenschaftlichen Fakultät der
Universität Bern

Automated Transverse Momentum Resummation for Electroweak Boson Production

by Monika HAGER

The production of electroweak bosons, followed by leptonic decays, is among the most basic hard-scattering processes studied at hadron colliders. Such processes provide backgrounds to new physics searches, enable the study of possible anomalous gauge couplings and provide spectra for determining the W boson mass and the angle θ_W . At small transverse momentum q_T , the electroweak boson production processes involve disparate scales, namely the small q_T and the large mass M of the bosonic states. Fixed-order perturbative results suffer from large logarithms of the ratio of these scales and hence become unreliable. The appropriate treatment of these logarithms is their resummation.

This thesis presents a framework for transverse momentum resummation for quark-induced boson production processes with arbitrary electroweak final states. The resummation is performed in an automated way and is based on reweighting events generated using a tree-level event generator. The kinematics of the electroweak final states are accessible, and this allows for the analysis of general observables in the small transverse momentum region.

Making use of the event generator MadGraph5_aMC@NLO, the resummation is implemented at next-to-next-to-leading logarithmic accuracy and matched to next-to-leading fixed-order results. Results for Z and W boson production with leptonic decay as well as for WZ production are presented. The predictions are validated using an existing resummation code and compared to experimental measurements.

Acknowledgements

I thank my supervisor Thomas Becher for confronting me with a challenging framework and for entrusting me the task of automating a complex calculation. His office door was always open, in the literal and the figurative sense of the word, enabling discussions at any time. I thank my office mates Ramon Stucki, Markus Moser and Laetitia Laub for their pleasurable company and Lorena Rothen for start-up support. I thank Anita Krattinger for proof-reading the introduction, Marcel Balsiger for beta testing my code and Thomas Becher for cross checking some of my results. Of course, I particularly thank my friends and family for their unfailing interest and encouragement.

Contents

Abstract	i
Acknowledgements	ii
Contents	iii
List of Figures	vi
List of Tables	viii
1 Introduction	1
1.1 The Larger Picture: What it's all about	2
1.1.1 Why we Need Physics	2
1.1.2 A Roadmap to Physics	5
1.1.3 Environment of the Present Work	8
1.2 Tracking the Invisible: From the Cloud Chamber to the LHC	10
1.3 The Cosmic Dance: How Particles Interact	14
1.4 Soaring at the Right Altitude: Physics and Scale	16
1.5 Measuring the Universe: Precision Physics and New Physics	18
1.6 Invitation to Cooperate: On the Relation of Theory and Experiment . . .	22
1.7 Getting down to Business: An Example Scattering Process	23
2 Preparation of Tools	29
2.1 Going Beyond Tree Level: The Factorization Formula for Small Transverse Momentum	29
2.2 Knowing our Limits: Effective Field Theories	31
2.3 Deriving the Factorization Formula: An Adventurous Journey	32
2.3.1 The 2 to 2 Scattering Process	32
2.3.2 SCET Kinematics and Lagrangian	34
2.3.3 Matching of the Current	37
2.3.4 From PDFs to Beam Functions	41
2.3.5 The Collinear Anomaly	42
3 Calculation of the Cross Section	44
3.1 The Hard Function to One Loop and Resummation of Large Logarithms .	44
3.2 The Fourier Integral with Beam Functions to $\mathcal{O}(\epsilon)$	47

3.2.1	Factoring Out Dependencies on the Hard Scale and Double Logarithms	47
3.2.2	Scale Setting and Modified Power Counting	50
3.2.3	The Beam Functions as an Expansion in L_\perp	51
3.3	The Transition from Electromagnetic to Electroweak Interactions	53
4	Highlights of the Calculations	55
4.1	Improving the Measurement: The Observable ϕ^*	55
4.2	A Step Towards More Realism: Considering Recoil Effects	57
4.3	The Art of Physics: Matching to Fixed Order	60
4.4	Sampling of q_T -values	64
5	Implementation of the Method	66
5.1	Dressing LO Events with NLO and NNLL Contributions	67
5.1.1	Generating Tree-Level Events with an Event Generator	67
5.1.2	Computing the One-Loop Corrections for the Hard Function	68
5.1.3	Computing the Reweighting Factor	68
5.2	Extracting Observables From the Reweighted Events	69
5.3	Instructions for the Use of the Reweighting and Analysis Codes	70
5.3.1	Generation of Events at Tree Level	70
5.3.2	Virtual Corrections to the Hard Function	72
5.3.3	Reweighting of Events	73
5.3.4	Analysis of Events	74
5.3.5	Fixed-Order Events at NLO	74
5.4	Matching and Comparison to Experimental Data	75
6	Results and Discussion	77
6.1	Z Boson Production	77
6.2	Z Boson Production and Leptonic Decay	78
6.3	W Boson Production and Leptonic Decay	81
6.4	WZ Production and Triple Gauge Boson Coupling	82
7	Conclusion and Outlook	85
A	Calculations	87
A.1	Power counting	87
A.2	The Lagrangian of SCET	88
A.3	Gauge invariance and gauge transformations	90
A.4	Wilson lines	91
A.5	Computation of the two-loop functions $\mathcal{D}_{i \leftarrow j}(z)$	94
A.6	NLO-expansion of the resummed cross section	100
A.7	Correlation of q_T and ϕ^*	101
B	Ingredients for the resummed cross section	103
B.1	Evolution of the hard function	103
B.2	Exponent to absorb dependencies	104
B.3	DGLAP splitting functions, convolutions and remainder functions	104

B.4 Boost	105
Bibliography	107

List of Figures

1.1	Early scientific testimonies	3
1.2	The Cube of Physics	6
1.3	Origin and measurement of a gravitational wave	7
1.4	Illustration of the Standard Model	10
1.5	Cloud chamber with particle tracks	11
1.6	Feynman diagrams for fundamental interactions	16
1.7	Rotational curves of galaxies, Quantum Mechanical spin	19
1.8	Lepton universality: decay of the tau	20
1.9	Lepton universality: electronic decay	21
1.10	Lepton universality: B meson decay	21
1.11	Theory and practice	22
1.12	Drell-Yan scattering at tree level	23
1.13	Kinematics of the Drell-Yan process	25
1.14	Drell-Yan scattering at one loop	26
1.15	Parton distribution functions	28
2.1	The hard interaction at one loop, beam function	30
2.2	The hadronic and leptonic part of the hard interaction	33
2.3	Timelike and spacelike momentum	40
3.1	Calculation of the hard interaction at NLO	45
3.2	Single quark and gluon emission	51
3.3	Double quark and gluon emission	52
3.4	Electroweak interaction	53
4.1	Construction of the observable a_T	55
4.2	Factorization of the observable ϕ^*	57
4.3	Correlation of q_T and ϕ^*	58
4.4	Considering recoil	58
4.5	Naive matching	61
4.6	Transition function	61
4.7	Average transverse momentum, matching correction and transition function	62
4.8	Improved matching	63
5.1	Structure and kinematics of the factorization theorem	67
6.1	Comparison to CuTe for $pp \rightarrow Z$	78
6.2	Treatment of final-state photon radiation	79
6.3	Comparison of NLL and NNLL for $pp \rightarrow Z \rightarrow e^+ e^-$	80

6.4	Comparison to ATLAS data for $pp \rightarrow Z \rightarrow e^+ e^-$	80
6.5	Matched NNLL result for the electron momentum in $pp \rightarrow Z \rightarrow e^+ e^-$.	81
6.6	Muon energy spectrum for $pp \rightarrow W^\pm \rightarrow \mu^\pm \nu$	82
6.7	Feynman diagrams for $W^\pm Z$ production	83
6.8	Matched cross section for $W^+ Z$ production	83
6.9	Transverse momentum in $W^+ Z$ production	84

List of Tables

6.1	Kinematic cuts for $pp \rightarrow Z \rightarrow e^+ e^-$	79
6.2	Kinematic cuts for $pp \rightarrow W^\pm \rightarrow \mu^\pm \nu$	82

Chapter 1

Introduction

If you can't explain something to a first year student, then you haven't really understood.

Richard P. Feynman, 1918-1988

Man muss die Dinge so einfach wie möglich machen. Aber nicht einfacher.

Albert Einstein, 1879-1955

This chapter is written in a popular scientific way, the first formulas entering in the last section only. It is therefore traceable for the courageous layperson, relating the current work to historical and modern endeavors in theoretical and experimental elementary particle physics. I attempt to clarify the role of precision physics with respect to “New Physics”, introduce the concept of scale and pay special attention to the relation of theory and experiment. I do urge the non-professional reader to read through the whole chapter including the last section, to get a taste of the work of physics.

In the second chapter, I introduce the notion of the effective field theory, applicable to a certain aspect of a problem, as opposed to a more general theory claiming to explain “everything”. I show how a complex problem can be decomposed by reducing mutual dependencies of physical quantities, a technique known as factorization. Most of the second chapter is dedicated to the derivation of the factorization formula that will be used in the rest of this work.

While physical processes can be measured and provide well-behaved results, our theoretical calculations can involve infinite expressions and large unphysical quantities that need to be eliminated. In the third chapter I disclose these “mathematical beasts”, establish their cause and demonstrate their treatment, allowing us to keep heading for the desired result.

The fourth chapter is dedicated to refining the results by choosing observables that can be measured with more precision in the experiment and by considering effects that had not been treated in previous work [1–4]. I combine the method, which has been developed to work well for a specific range of energies, with other techniques in order to obtain a result valid for all energies of interest.

At the heart of the framework for automated transverse momentum resummation presented in this thesis are two codes that are made available for other researchers in the field. The first one is a general reweighting code, applicable for Z and W bosons produced through quark-anti-quark annihilation with leptonic decay. To run the reweighting code, only technical adaptations such as setting paths are necessary. The second one is an analysis code that is specific and needs to be tailored to the production and decay process of interest. These codes are featured in chapter five, along with detailed instructions.

In the second to last chapter, I apply the resummation method to various scattering processes to obtain qualitative and quantitative results for diverse observables. The results are validated using an existing resummation code and compared to experimental measurements, and the findings are discussed. I conclude with an assessment of the work performed and an outlook to possible applications and extensions of the framework.

1.1 The Larger Picture: What it’s all about

1.1.1 Why we Need Physics

It seems like humans have always been driven by the desire to understand who we are, where we came from and where we are going. This desire has led to multifarious activities such as the observation and exploration of our surroundings which led to the evolution of science. Archaeological relics corroborate astronomical observations dating back as far as the last ice age. The carvings on the 30’000 year old bone in Fig. 1.1 are thought to represent lunar phases.

The ancient Greeks laid the foundation for science to explain nature based on its intrinsic laws without involving heavenly powers to claim correctness of the explanations.



FIGURE 1.1: Left: 30'000 years old bone with carvings presumably representing lunar phases. Right: Determination of the earth's circumference by Eratosthenes. The large and the small circle segment are similar, as they share the same angle. Knowing this angle and the distance between Syene and Alexandria (marked as two points on the circle) suffices to determine the circumference of the earth. Illustrations from [5].

The Pythagorean Theorem¹, the principle of Archimedes on buoyancy, the formulas for surfaces and volumes of spheres, cubes and cones and many more topics of Greek provenance are taught in school to this day.

The Greeks were also active in astronomy and mapmaking. Let me trace the reasoning of Eratosthenes² to determine the circumference of the earth. Eratosthenes imagined a circle sector defined by the center of the earth and the positions of the two cities Syene and Alexandria, which as he knew are located at equal longitude. If he knew the angle of that circle sector and the length of the circular arc, the circumference could be calculated, because the ratio of the angle to the full angle of 360 degrees equals the ratio of the circular arc (the distance between the two cities) to the circumference of the earth, see Fig. 1.1. The distance between the two cities was measurable by the pace of a camel caravan from Syene to Alexandria needing 50 days when advancing approximately 100 stadia³ per day. But how to find out the angle? Eratosthenes assumed that the sun was directly overhead at noon on the summer solstice in Syene, because the reflection of the sun was visible on the surface of the water in deep wells. Since the two cities are located at equal longitude the sun reaches its highest point at the same time of the day in both of them. He noticed that the rod of a sundial in Alexandria threw a shadow at noon on the summer solstice. He assumed solar light rays to fall on the earth on parallel paths so that angles between these parallel rays and straight lines are equal. Using the straight line from the earth's center to Alexandria, he found a circle sector similar to

¹In a rectangular triangle the lengths of the sides relate as $a^2 + b^2 = c^2$, c being the longest side.

²Eratosthenes of Cyrene (around 276-194 BC) was a Greek mathematician and geographer.

³A stadium is an ancient Greek unit of length, corresponding to approximately 185 meters.

the first one: This sector was defined by the rod of the sun dial in Alexandria and its shadow. This allowed him to measure the desired angle. His result for the circumference of the earth was 10 to 15 percent off from today's value.

There is general agreement on the fact that in the medieval period vivid scientific activity took place rather in the Chinese, the Indian and the Islamic cultures than in Europe. One should still not overlook the wealth of inventions and enhancement of devices that era left behind in Europe such as the wheeled plough, the water mill, the compass, the foot-operated loom and spinning wheel, the wheel clock, the furnace, spectacles, the production of oil colors, acids and alcohol and lastly the letterpress, to name only a few.

The 16th and 17th centuries put forward a major scientific revolution and rang in a drastic change of the self-concept of mankind in the universe. Due to a variety of astronomical observations the idea that earth rests at the center of the universe could no longer be upheld. Galilei⁴ constructed a telescope to observe the nocturnal sky and discovered the phases of Venus. They were easy to comprehend assuming the planets revolve around the sun. The evolution from geocentrism to heliocentrism is referred to as the Copernican⁵ revolution.

Physics as it is taught at universities today starts after this revolution with Newtonian physics⁶. Newton's three laws of motion⁷ allow us to understand just about every physical phenomenon accessible by our senses. Want to construct an Eiffel Tower or a bicycle? The Laws of Newton suffice. Want to fly to the moon? The Laws of Newton together with his Gravitational Theory suffice⁸. Want to predict the flight path of a ball? The Laws of Newton suffice⁹. At this point, I need to clarify the term "mass", an important quantity in physics, and its relation to the everyday notion "weight". The mass of an object is constant throughout the universe, while its weight depends on gravitational attraction. Compared to your weight on the earth, you would feel six times lighter on the moon, because the moon exerts a gravitational force on masses which is six times smaller than the one on earth.

⁴Galileo Galilei (1564-1642) was an Italian physicist, mathematician and astronomer.

⁵Named after the Polish astronomer and natural scientist Nicolaus Copernicus (1473-1543).

⁶Isaac Newton (1643-1727) was a British mathematician, physicist and astronomer.

⁷First law: Any object either remains at rest or continues to move at a constant velocity, unless acted upon by a force. Second law: The vector sum of the forces F on an object is equal to the mass m of that object multiplied by the acceleration a of the object: $F = ma$. Third law: When one body exerts a force on a second body, the second body simultaneously exerts a force equal in magnitude and opposite in direction on the first body.

⁸This applies to the aspects of the construction of the spacecraft and making use of gravity, albeit not to the transmission of wireless signals or the use of computing devices necessary for such an endeavor.

⁹While playing with my dog I had been able to convince myself that she was well informed about the Laws of Newton. Albert Einstein also pondered on falling objects and the observation that gravity and acceleration had the same effect on masses led him to the equivalence principle which is at the heart of his Theory of General Relativity.

Another dramatic change in our idea of the world befell us some 100 years ago with the advent of Quantum and Relativistic Physics¹⁰. The millenia-old question¹¹, whether matter could be split up into smaller pieces endlessly or whether there existed some basic *elementary* building blocks no further reducible, was approaching an answer in the Bohr¹² model which postulates that matter consists of atoms comprising a nucleus and a shell. Based on the Standard Model, born 50 years ago, today's answer to this question is: "Yes, there are basic building blocks of matter - elementary particles that are indestructible and have no substructure." Though the effects of Quantum and Relativistic Physics are not relevant for our everyday life, we do use tools that are sensitive to their effects. The laser beam, widely in use in research and in industry, could not have been developed, were the principles of Quantum Physics still unknown. The Global Positioning System would be very inaccurate, were Relativistic Physics not considered¹³.

1.1.2 A Roadmap to Physics

After briefly touching upon basic concepts such as the Laws of Newton, the Standard Model and other physical terminology, let's look for some orientation in the multitude of physical theories. The *Cube of Physics* [6] is useful for relating physical theories to each other and to understand how they have evolved. It is spanned by three axes corresponding to three fundamental constants of nature, the *speed of light* c in vacuum, the *Planck constant* h ¹⁴ and the *gravitational constant* G , see Fig. 1.2. All physical theories attribute a value to each one of these constants, the shift of values documenting the ceaseless development of our understanding of nature.

According to the Special Theory of Relativity, the speed of light c in vacuum is constant throughout the universe. It can be measured accurately. Before the formulation of Special Relativity in 1905, it was thought to be infinite, meaning light was thought of as propagating instantaneously. One corner of the Cube of Physics is therefore located on the c -axis where the speed of light is infinite¹⁵. The Laws of Newton, also known as "Newtonian Mechanics", live on this corner of the cube. This corner approximately dates from the year 1700. Special Relativity dwells on the neighboring corner on the c -axis. The Laws of Newton are not in contradiction to Special Relativity, the latter

¹⁰The Swiss, German and US-American physicist and Nobel laureate Albert Einstein (1879-1955) conceived the Special and General Theories of Relativity.

¹¹Around 400 BC the Greek philosopher Democritus (460-371 BC) expected matter to consist of indivisible objects, the indestructible "atoms".

¹²Niels H. D. Bohr (1885-1962) was a Danish physicist.

¹³<https://www.srf.ch/sendungen/einstein/einstein/haetten-wir-ohne-einstein-kein-gps>

¹⁴Named after the German physicist Max Planck (1858 - 1947).

¹⁵ $c = \infty$, or, more precisely, $1/c = 0$.

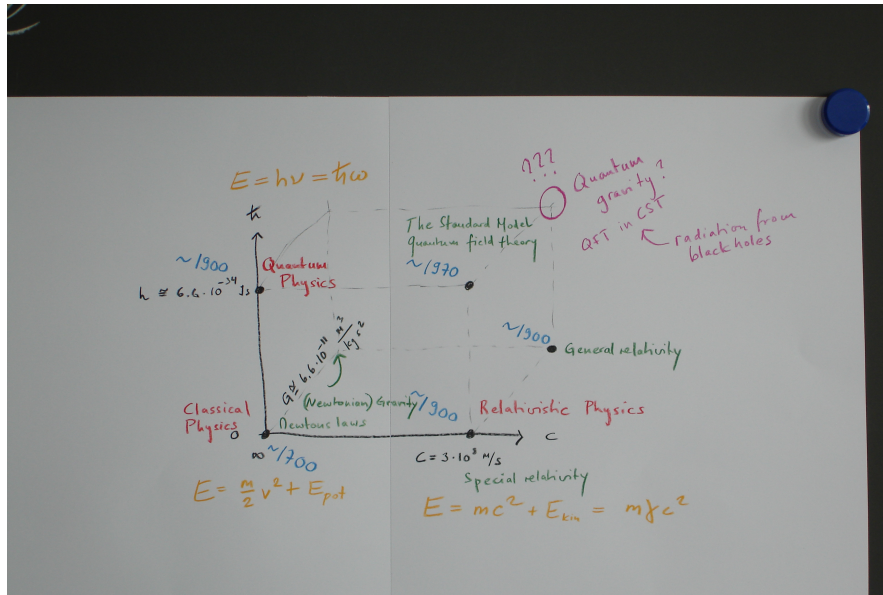


FIGURE 1.2: The Cube of Physics. Photograph and illustration M. Hager.

is simply a generalization of the former. A common wording in physics is: “Special Relativity reduces to Newtonian Mechanics if we set c to infinity”.

Now we turn to the vertical h -axis. The Planck constant h is the characteristic constant of Quantum Mechanics. It relates energy to frequency and provides a threshold for the fundamental uncertainty principle of Quantum Mechanics¹⁶. The constant h does not appear in the Laws of Newton, and it can be stated that “Quantum Mechanics reduces to Newtonian Mechanics if we set h to zero”. With these considerations, the neighborhood of Classical and Quantum Mechanics has been settled. The evolution from Newtonian Physics to Quantum and Relativistic physics took 200 years. The more recent corners can therefore be dated to the year 1900.

We are now in a position to set foot on the fourth corner of the c/h -plane. Here live the theories that have incorporated the findings both of Quantum Mechanics and Special Relativity, among them the Standard Model of Particle Physics and Quantum Field Theory, the two foundations on which the present thesis is based. We need to consider Special Relativity, because in the experiments performed in particle physics, also known as high energy physics, subatomic particles are accelerated to high velocities - nearly to the speed of light. Approaching the associated questions using Newtonian Mechanics alone would therefore not lead to meaningful results. We need to consider Quantum Mechanics, because atomic and subatomic particles behave very differently than the everyday-objects in the world around us. As sketched above, the latter can be satisfyingly studied using Newtons Laws, while the former have shown to be well

¹⁶The Uncertainty principle imposes a fundamental limit on the precision with which certain pairs of physical properties of a particle, e.g. energy and lifetime, can be determined.

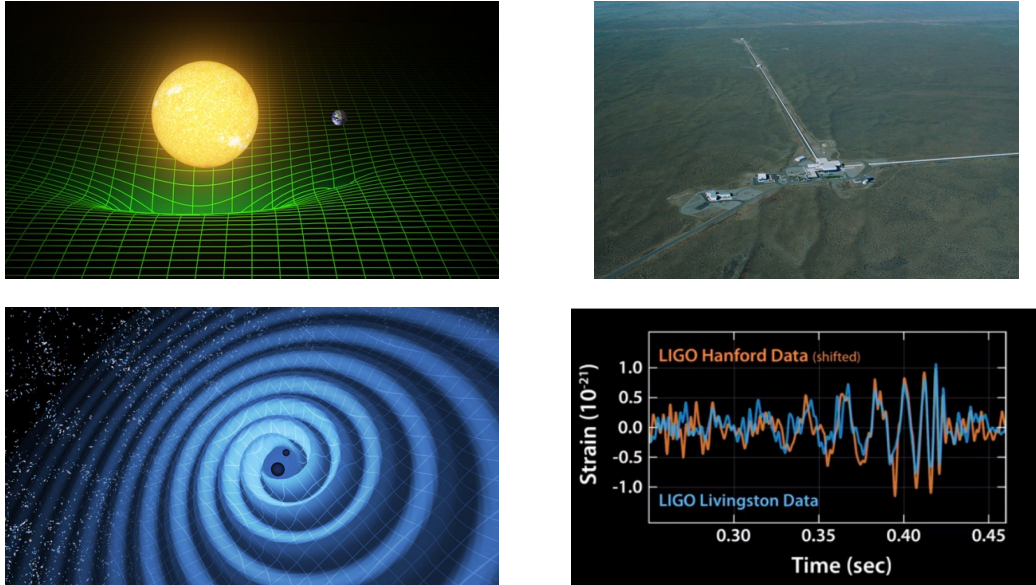


FIGURE 1.3: Upper left: Masses bend spacetime. Lower left: Moving masses cause gravitational waves. Upper right: Observation site in Hanford, USA, with arms of 4 km length each. Lower right: Measurement data from two observation sites. Illustrations Courtesy Caltech/MIT/LIGO Laboratory [7].

described by Quantum Mechanics. The Standard Model is about fifty years old; this corner can thus be dated with the year 1970.

The cube-neighborhood of Special Relativity is complete, whereby the remaining adjacent corner is inhabited by the General Theory of Relativity. This theory describes gravity as a geometric property of space and time and can be termed a generalization of Special Relativity and Newtonian gravitation. The characteristic constant of gravity is the gravitational constant G . While this corner can be dated to the year 1915, and General Relativity is well-established experimentally, the direct verification of one specific prediction of the theory was successful only 3 years ago with the detection of gravitational waves.

What is a gravitational wave? In Special and General Relativity, space and time are no longer considered independent properties of the universe. Instead, they are viewed as related to each other and are combined in the concept of *spacetime*. According to General Relativity, spacetime is bent by masses. A moving mass therefore causes a gravitational wave - a ripple of spacetime that spreads through the universe at the speed of light. Gravitational waves can be observed using so-called laser interferometers. As a rule, the smaller the effect to be measured is, the larger the observation apparatus needed. As the effect of a gravitational wave is tiny, the two "arms" of the interferometer must be of considerable length. Other local sources such as earthquakes or lightning could produce measurement results similar to those of a gravitational wave. At least two measurement sites are therefore needed to confirm an observation (see Fig. 1.3 for illustration).

How to combine General Relativity with Quantum Mechanics is an open problem - in fact it has been, still is and will remain a topic of vigorous research. The Cube of Physics is "under construction" to this date. No one knows how physics will evolve in coming decades. Maybe physics will be represented by another model in the future.

1.1.3 Environment of the Present Work

My work relies on the Standard Model, a theory that describes the elementary particles and their interactions. We have already discussed that elementary particles are the basic building blocks of matter. Where can they be found? Our contemporary physical world view as it has evolved over the last 300 years, based on countless observations, experiments, models and theories, is the following: Matter in and around us consists of atoms. A number of atoms can be bound to form *molecules*. Water, oxygen, proteins, plastic and starch are examples of molecules. The atoms are electrically neutral, while they are composed of electrically charged sub-particles. Negatively charged *electrons* are distributed in the shell of the atom, while positively charged *protons* and electrically neutral *neutrons* form the nucleus of the atom. The proton and the neutron are subsumed under the term *nucleons*. Electrons can be withdrawn or added to the shell, leaving behind an atom or molecule that is no longer electrically neutral, a so-called *ion*. The *ionisation* process can be induced naturally or by experiment. A natural processes involving ions is the rusting of iron. The main component of sea salt is a compound of sodium and chloride ions. Processes involving the atom are studied in Atomic Physics and in Chemistry.

The *nucleus* of the atom is likewise subject to natural or experimentally evoked modifications. The natural radioactivity in our surroundings is a manifestation of such an occurrence in the atomic nucleus. When potassium in our body decays to calcium, a neutron in the potassium nucleus decays spontaneously to a proton, hereby emitting an electron and leaving behind a calcium atom¹⁷. The processes involving the nucleus of the atom are studied in Nuclear physics.

Now that we have become acquainted with the electron, the neutron and the proton, let's reason whether they are elementary or composite particles. The radioactive decay can be taken as an indication that the neutron has some kind of substructure. But this is not enough, as we shall see in the following sections. There are particles that are elementary, yet decay all the same. Dedicated experiments in the sixties and seventies, where electrons were scattered from *positrons*¹⁸, protons from protons and electrons

¹⁷As a matter of fact a third particle is ejected, called a *neutrino*. This is an electrically neutral particle of vanishing mass that is challenging to detect. It is considered elementary.

¹⁸The positron is identical to the electron save for the electric charge which is opposite to that of the electron.

from protons, allowed to discern elementary from composite particles. The Standard Model considers the electron as an elementary particle, while the neutron is considered a composite particle. The radioactively decaying proton is also considered a composite particle¹⁹.

Evidently this leads to the question: Are protons and neutrons composed of elementary particles? The Standard Model answers: "Yes, protons and neutrons consist of *quarks*, which are elementary." Even though electrons and quarks are both elementary, there exist essential differences. The electron can be bound in the atomic shell, but it can also exist as a free particle. It is a stable particle that does not decay. It can be detected in a simple experimental setup, see Section 1.2. A single quark on the other hand does not exist as a free particle for more than the blink of an eye. Three quarks can be bound to form a proton or a neutron. There also exist short-lived particles made up of two quarks. Observing quarks requires considerable experimental effort.

We are now touching upon basic components of the Standard Model. Quarks come with positive or negative fractions of the electron charge and in three *generations*, see Fig. 1.4, differing only in mass from one generation to the next. The first generation of quarks with the *up* and the *down quark* make up the protons and neutrons of ordinary, stable matter. The next two generations have been found to form further short-lived particles. The electron, in conjunction with the *neutrino*, the aforementioned electrically neutral, almost massless particle difficult to detect, makes up the first generation of *leptons*. The *muon*, belonging to the second generation, is the heavier sibling of the electron. It will be introduced in Section 1.2 and featured in Section 1.5. The remaining particles postulated by the Standard Model, the mediators of the interactions amongst the elementary particles called *bosons*, are featured in Section 1.3.

Many physical phenomena can be understood by means of the Standard Model. It can describe ordinary matter and why matter sticks together even though it is mainly empty space, as we know from Atomic Physics. The Standard Model distinguishes elementary particles from composite particles and describes the latter's substructure. These questions have been investigated in collider experiments and many particles have been discovered in accordance with the Standard Model. However the Standard Model can not explain all physical occurrences. It has a so-called hierarchy problem that will be highlighted in Section 1.4. It neither can explain the "dark matter" nor the "dark energy" that seems to dominate our universe. A few recent experimental measurements show deviations regarding important quantities predicted by the Standard Model. More

¹⁹Protons and neutrons bound in the nucleus both decay radioactively. The situation is different for free neutrons and protons. Free neutrons can decay in the same manner as bound neutrons. On average free neutrons exist for about 15 minutes before they decay. Free protons on the other hand are considered stable, as no decay has ever been witnessed. In fact, experiments searching for free proton decay are ongoing.

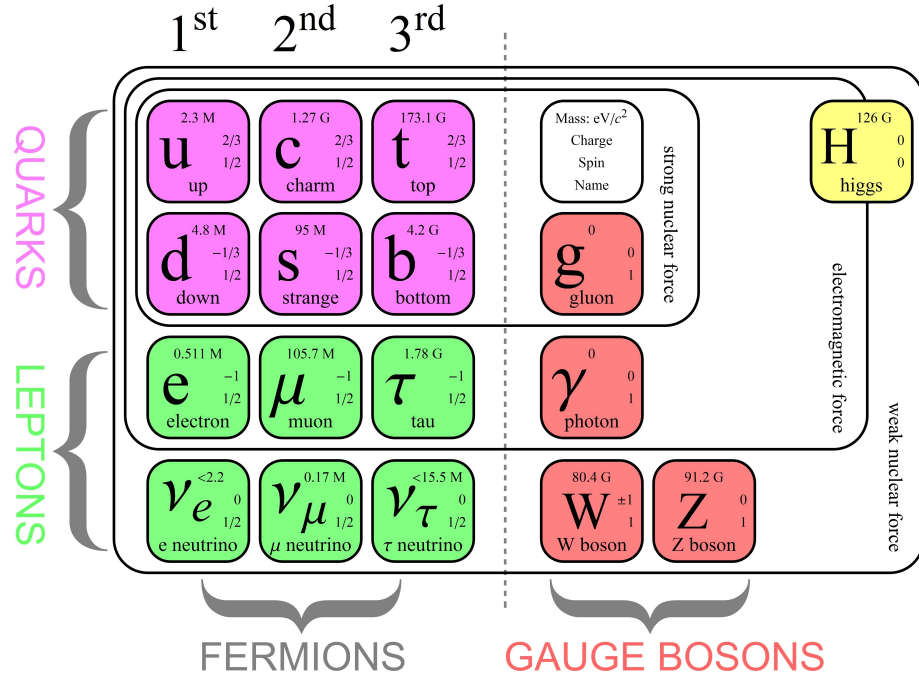


FIGURE 1.4: Illustration of the Standard Model [8].

precise measurements and theoretical studies are necessary in order to judge whether these deviations disclose "New Physics" or whether they stem from the inevitable uncertainties of calculations and measurements, see Section 1.5.

To sum up, the present work is based on Quantum Field Theory and the Standard Model. It belongs to the areas of research called "Collider physics", "Elementary particle physics" and "Precision physics" and aims at improving the precision of physical quantities relevant for the Standard Model.

1.2 Tracking the Invisible: From the Cloud Chamber to the LHC

One of the earliest detectors for radiation was the cloud chamber as used by Wilson²⁰. During my studies at the University of Bern, I had the opportunity to operate a simple version of the cloud chamber [9]. A ethanol soaked piece of paper is placed along the side of a plastic chamber similar to a bucket. The chamber is then sealed with a plastic foil at the top and placed in a cooling bath of liquid nitrogen. After about an hour droplet tracks become visible inside the chamber. What happened? The alcohol vaporizes from the paper at the top of the chamber, which is at room temperature. As the vapor approaches the significantly cooler region near the bottom of the chamber²¹ it condensates

²⁰Charles T.R. Wilson (1869-1959) was a British physicist.

²¹The liquid nitrogen is at its boiling point around -200° Celsius.

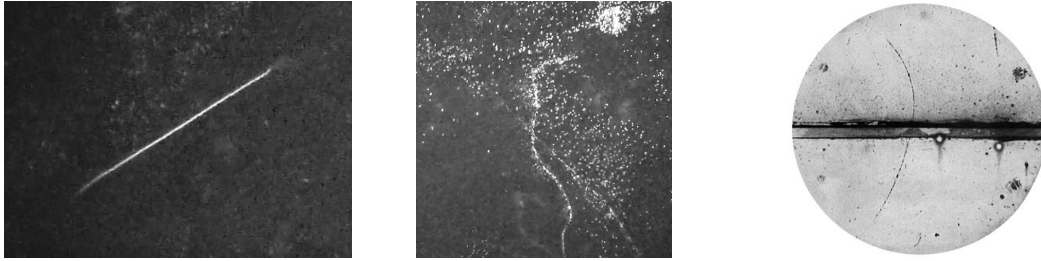


FIGURE 1.5: Left: Alpha decay. Photograph by A. Ariga. Middle: Beta decay. Photograph by A. Ariga. Right: The discovery of the positron. The radius of the curvature is larger on the lower side of the lead plate and smaller on the upper side. This shows that the particle went from the lower side to the upper side of the plate. The track of an electron would be bent the other way round. Illustration from [10].

to droplets. Specks of dust or charged particles can serve as condensation nuclei for the droplets. Dust particles lead to single droplets. Other droplets appear rapidly, one after the other, forming a track resembling a string of pearls. Why? Wilson hypothesized that *the condensation nuclei are charged particles knocked off the air molecules present in the chamber by some radiation permeating the chamber*. The droplet tracks indirectly verify the presence of charged particles and moreover of radiation producing these in the chamber. Fig. 1.5 shows two of the innumerable patterns that emerge and decay in this simple experimental setup, witnessing occurrences our senses are blind for, but are nonetheless accessible indirectly, provided we come up with an intuition how to reveal nature's secrets.

What exactly is this radiation apparent in our surroundings manifesting itself in the cloud chamber and where does it stem from? In the cloud chamber mainly *alpha* and *beta radiation* can be observed. The radiation can stem from the natural radioactivity in our surroundings. A beta decay occurs e.g. when potassium in our body decays to calcium: A neutron in the nucleus of the potassium atom decays spontaneously to a proton, hereby emitting an electron - the beta-radiation²². Electrons leave behind thin, crooked trails. This is because the light electrons are deviated when they collide with the heavy air molecules. The heavier and larger *alpha-particles*²³ hit many air molecules when passing the chamber and therefore show thick, straight tracks. Another source for the radiation observable in the cloud chamber is *cosmic radiation* consisting of highly energetic particles that reach the earth's atmosphere from outer space. These particles, mainly protons and atomic nuclei, interact with the molecules in the atmosphere, creating a particle shower composed of *mesons*, short-lived particles made up of two quarks. The mesons decay for their part, e.g. to a muon and a neutrino. The muon is the heavier version of the electron and can be observed in the cloud chamber with a little luck (as

²²This is the often quoted "wave-particle duality" of Quantum Mechanics: Depending on which aspect we are interested in, we speak of a particle (the electron) or a wave (beta-radiation).

²³Alpha particles consist of two neutrons and two protons bound together. As such they can also be termed Helium nuclei or (fully) ionized Helium.

this radiation occurs less frequently than alpha or beta radiation). Cosmic radiation is not fully understood to date. It is believed to stem from *supernovae*, stars at the end of their lifetime.

What do we learn from the cloud chamber experiment? Generally speaking it confirms there is a lot going on in the world at a lower scale undetectable by our senses. Through patient observation and thorough evaluation we can infer on characteristics of the interaction between electrons and air molecules and hypothesize models on the nature of the interacting particles. Historically, the cloud chamber enabled the discovery of the positron: a particle identical to the electron save for the electric charge, which is opposite to that of the electron²⁴. How was that possible? Charged particles like the electron and the positron are deviated when they pass through a magnetic field: The tracks become curved if one establishes a magnetic field surrounding the cloud chamber. For oppositely charged particles, the curvature is opposite. In 1932, Anderson²⁵ installed a magnetic field and additionally put a lead plate into the cloud chamber to slow down the particles. Slowing down a particle will reduce the radius of its track. These modifications enabled him to determine the flight direction of the particle. Using this setup, he was able to distinguish tracks of oppositely charged particles and to discern the electron from the positron.

It is worth pointing out the randomness of the events in the cloud chamber in the sense that one has no influence on what will take place next. Consequently, the challenge consisted in creating experiments under controlled testing conditions allowing for specific observations. Let us consider how the experimental setup could be modified for observing elementary particles such as the quark. We can interpret the outcome of the cloud chamber experiment in different ways. Assuming that we are well-informed about the nature of alpha and beta radiation, but ignorant in respect to the structure of an air molecule, we hypothesize: *“The radiation permeating the chamber serves to probe the substructure of air molecules.”* The droplet tracks then confirm the air molecules contain charged particles that can be knocked off by radiation. So we have learned something about the structure of the air molecule. On the other hand, if we are versed in the structure of molecules and atoms, but uninformed concerning radiation, we formulate another hypothesis: *“The droplet tracks testify the presence of radiation in the chamber”*, as we are quite sure that they stem from electrons knocked out of the atomic shell and

²⁴Each particle has a so-called anti-particle. Particle and anti-particle differ solely in their electric charge, which is of equal magnitude and opposite sign. While matter consists of particles, anti-matter consists of anti-particles. The universe contains much more matter than anti-matter. No one knows why this is the case.

²⁵Carl D. Anderson (1905-1991) was a US-American physicist of Swedish origin.

that this can only be achieved by means of radiation²⁶. We can then use the features of the tracks to infer on the nature of the radiation.

The first version of the experiment that aims at probing the substructure of the *target* (the air molecule) can be improved by controlling the incident radiation. A beam of electrons can be directed on the target and the beam energy and intensity, i.e. the number of beam particles incident per time unit, can be varied systematically. The target can be put to some fixed location, so that striking it or not with the electron beam is not left to chance. In fact, the *electron microscope* is based on such a setup. It is used to analyse the structure of cells, large molecules, metals and crystals. The electron beam is tuned to do no or little damage to the sample. Parts of the sample will be transparent to the electrons and they will simply pass through, while other parts will deflect the electrons. The result is an image of the sample. To probe the *substructure* of a target however, high energies are needed, so that the electrons can interact with the sample. As a result of this observation the target will be - at least temporarily - damaged or destroyed.

The second version of the experiment aiming at detecting unknown radiation can be optimized by choosing targets that are more sensitive to radiation and by installing an electric field. Digital cameras can be seen as a further stage of the idea behind the cloud chamber. A single target, here called a *pixel*, consists of a layer of silicon²⁷. Incoming light knocks electrons out of the silicon layer. The more incident light, the more electrons knocked out. These electrons are moved to a place where they can be read out by means of an electric field and electronic devices. Each pixel is then assigned a number corresponding to the amount of electrons knocked out, i.e. the brightness. A large number of such pixels are arranged in a rectangular array; all pixels together generate the image.

To probe the substructure of a proton we must go along with the first version of the experiment. Let's replace the target and put a proton there instead of an air molecule. We can now direct a beam of electrons at the proton target. This experiment was performed in the late sixties. As an outcome of the experiment, one measured the scattered electron and a large number of further particles, amongst them some mesons already known from former experiments. This process is called *deep inelastic scattering*. The term *inelastic* refers to the fact that the electron was scattered from the proton,

²⁶This is the sequence in which knowledge was gained historically: Molecules and atoms were discovered previous to radioactivity.

²⁷Silicon is a metalloid, the most common element on earth after oxygen. It is present e.g. in dust and sand. As a *semiconductor*, it is widely in use in electronic devices.

causing the latter to shatter²⁸. The result of deep inelastic scattering could be explained using the *parton model* of the proton. This model says that the proton is made up of *partons*, the three quarks²⁹.

In order to gain more energy for the collision two beams of protons can be aimed against one another instead of directing one beam of particles on a target. This is exactly the experiment currently performed at the research institution *CERN* in Geneva, Switzerland. The experimental setup is called the *Large Hadron*³⁰ *Collider (LHC)* and besides probing the substructure of nucleons it serves to study the elementary particles and their interactions.

In conclusion, we have seen how one tackles the challenge of observing the elementary building blocks of matter. Whereas the cloud chamber may be used to observe the electrons in the shell of the atom particle colliders enable a look right into the constituents of the atomic nucleus - at an unbelievably small scale³¹. It can be pointed out that the smaller the scale we wish to investigate, the larger the energy needed for the collision or the interaction process. This holds true also for the experimental hardware. The LHC can be viewed as an enormous microscope used to investigate the smallest constituents of matter.

1.3 The Cosmic Dance: How Particles Interact

So far the focus was on elementary particles and methods to observe them. I have used the somewhat undifferentiated term “collision”. In this Section the focus moves to the interactions of the elementary particles. I begin with a quote from Fritjof Capra³²[11]: “The exploration of the subatomic world in the twentieth century has revealed the intrinsically dynamic nature of matter. It has shown that the constituents of atoms, the subatomic particles, are dynamic patterns which do not exist as isolated entities, but as integral parts of an inseparable network of interactions. These interactions involve a ceaseless flow of energy manifesting itself as the exchange of particles; a dynamic interplay in which particles are created and destroyed without end in a continual variation of energy patterns. The particle interactions give rise to the stable structures which

²⁸In elastic scattering, the outgoing objects are the same as the ingoing ones. A popular example for elastic scattering is the collision of billiard balls. In inelastic scattering, at least one of the collision partners is damaged, e.g. in a road accident with two vehicles.

²⁹In fact, the substructure of the proton involves a much more complex interplay of partons, which include quarks, anti-quarks and the gluons postulated by the Standard Model.

³⁰Hadron is the umbrella term for particles made up of quarks, like the proton and the neutron built by three and the mesons built by two quarks.

³¹Historically, after the investigation of the atomic shell, one first acquired insight on the atomic nucleus in even more scattering experiments before advancing towards the nucleons.

³²Fritjof Capra (1939) is a US-American physicist of Austrian origin.

build up the material world, which again do not remain static, but oscillate in rhythmic movements. The whole universe is thus engaged in endless motion and activity; in a continual cosmic dance of energy.”

Four fundamental forces are known and have been studied to date: the gravitational force, the electromagnetic force, the weak force and the strong force. Gravity manifests itself on a large scale by binding together planets, stars and galaxies. At the level of elementary particles, however, due to their tiny masses, gravity’s effect is extremely small compared to that of the other forces and can therefore be neglected. The electromagnetic force combines the effects of electricity and magnetism; it binds electrons to the atomic nucleus. The strong force binds quarks together in protons and neutrons. The weak force is responsible for decay processes. The *Higgs exchange*³³ can be viewed as a fifth force. It will be addressed in the next section.

The four fundamental forces are also called the four fundamental interactions. The term “interaction” emphasizes the fact that interacting partners, mediators and charges are involved. All electrically charged elementary particles take part in the electromagnetic interaction - quarks, electrons and muons, as well as the protons in the atomic nucleus and atomic or molecular ions. The electric charge can either be positive or negative. Charges of the same type repel each other, and charges of different types attract each other. The mediator of the electromagnetic interaction is the *photon*. What is a photon? We have already touched upon the wave-particle duality by speaking of either the electron or of beta radiation, respectively. Similarly light can be seen as a wave, e.g. in a rainbow as the result of the refraction of a light wave by raindrops. However, if we are interested in the interaction of light with matter, it is more convenient to view light as a particle. A photon is simply the particle version of light. An example for the interaction of light with matter is the *photoelectric effect*³⁴: Electrons can be emitted from metallic materials when light shines on it; the electron absorbs a photon to gain energy and thus overcomes the atomic bond. This electromagnetic interaction can be pictured using a *Feynman diagram*³⁵, see Fig. 1.6.

Only quarks take part in strong interactions. Strong and electromagnetic interactions together account for the stability of matter. The charges of the strong interaction are called *color charges*; this has nothing to do with everyday colors. There are three color charges called red, blue and green. The mediator of the strong interaction is the *gluon*. Like the photon, the gluon is massless. Unlike the electrically neutral photon, the gluon is itself color charged.

³³Peter W. Higgs (1929) was a British physicist.

³⁴Einstein studied the interaction of light with materials and was awarded the Nobel prize for explaining the photoelectric effect in 1905. Solar cells and digital cameras, as featured in Section 1.2, are only two examples from the wide range of photoelectric effect applications.

³⁵Richard P. Feynman (1918-1988) was a US-American physicist.

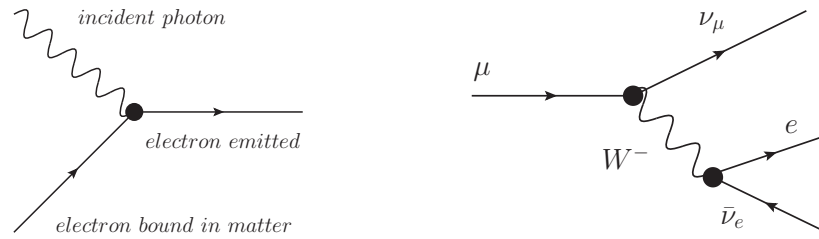


FIGURE 1.6: Left: The photoelectric effect. Light shines on matter, represented by a photon (upper left line). An electron (lower left line) absorbs the photon, becomes energetic and leaves the atomic shell (right line). Right: Muon decay (see text for details).

All particles take part in the weak interaction responsible for decay processes. Mediators of the weak interaction are the W boson and the Z boson. These mediators are massive unlike the photon and the gluon. Both the W boson and the Z boson carry weak charge. In addition, the W boson also has electrical charge; there is the positively charged W^+ and the negatively charged W^- . The Z boson is electrically neutral.

Even though gravity is too weak a force to play a role in the sector of elementary particles and is not included in the Standard Model, I complete this section with a few words on the gravitational interaction. It is commonly known that gravity acts on masses. Special Relativity postulates the equivalence of mass and energy³⁶, therefore the statement is: “The gravitational charges are mass and energy.” All particles are affected by gravity, including the massless ones like the photon³⁷. The mediator of gravity is the hypothesized *graviton* which has not been detected to date.

1.4 Soaring at the Right Altitude: Physics and Scale

All of the four fundamental interactions have characteristic scales. How do these come about? The three fundamental constants of nature that span the cube of physics, the gravitational constant G , the speed of light c and the Planck constant h , can be combined to give “natural” units of time, length and mass. The resulting Planck time and Planck length are thought to represent the shortest distances and times relevant in physics. The Planck length is many orders of magnitude smaller than e.g. the diameter of an atomic nucleus. The Planck time is much shorter than the lifetimes of the particles discovered

³⁶This is stipulated in the probably most famous formula of physics, $E = mc^2$. On the left side of the equation E stands for energy and on the right side of the equation we have the mass m times the speed of light c squared. This formula is applicable for any object, be it an elementary particle or a massive body known from everyday life.

³⁷In Special Relativity, the energy of an object comprises two terms which can be seen as the energy the object has at rest (this energy depends on the mass of the object) and the energy it possesses due to its movement. Although the rest energy of a massless particle, like a photon, is zero, it does have energy (which is related to its frequency).

to date. Since this scale is not experimentally accessible at present, we can only wonder what physical phenomena might be taking place there.

The *Planck mass* that can be found using G , c and h corresponds to around 0.02 milligrams - a tiny quantity compared to the everyday unit of a kilogram. But an enormous quantity compared to the mass of a proton. As discussed mass and energy are the gravitational charges. The Planck mass must therefore be viewed as the characteristic scale of gravity. Surprisingly this scale is way larger than the scales in the realm of the elementary particles. This fact is known as the *hierarchy problem*. Why is this a problem? Owing to the hierarchy of scale, the fundamental interactions cannot be treated in a common framework. A lot of effort has been made to find a theory valid for all of the fundamental interactions. While the electromagnetic and the weak interaction have received a common framework in the *electroweak interaction*, it has not been possible to combine the gravitational interaction with any other fundamental interaction. This reveals the limits of the Standard Model, our best practice in physics today: The Standard model cannot explain the hierarchy problem. Research persists to unify the fundamental interactions. The models proposed so far can either not be verified or falsified (because their effects are not accessible experimentally) or the predicted effects have not been observed to date. These various models are subsumed in the term "physics beyond the Standard Model" - *BSM physics*.

The characteristic scale of the electroweak interaction, established at many orders of magnitude below the Planck mass, is referred to as *vacuum expectation value of the Higgs field* v . With the discovery of the *Higgs boson* at the LHC in Geneva (2012) it has become a matter of common knowledge that "the Higgs boson gives mass to the particles". Now, what might that mean? Let me start with an analogy from everyday life: The coins used in our everyday life would be useless were they not assigned a certain value by the national bank. While the masses of particles can be measured in experiment, it has been hard to incorporate the generation of mass into our physical theories. In 1964, the *Higgs-Mechanism* was proposed to solve this difficulty. The existence of a further mediator, the Higgs boson, was postulated. As indicated above, particles can just as well be pictured as waves. In the present example, the term *field* is more convenient. The earth has a gravitational field, and an electrically charged particle gives rise to an electric field. The effects of a field can be felt in the surroundings of their source, whereby they are stronger near the source and weaker at larger distance to the source. The particles can thus be viewed as excitations of fields acting in spacetime. The Higgs field can be thought of as encompassing our universe. All massive elementary particles and mediators interact with the Higgs field through electroweak interaction. It is by this interaction that they obtain their mass. To come back to the analogy from

everyday life, it is through a formal act of the national bank (the Higgs field) that coins (the particles and mediators) receive a value (mass).

1.5 Measuring the Universe: Precision Physics and New Physics

The Standard Model cannot explain the hierarchy problem as seen in the last section. Furthermore there are additional observational results that seem to contradict its predictions. Astronomical observations have shown that galaxies rotate, like the planets rotate around the sun or a vinyl record rotates around its center. For a rigid body like a vinyl record the rotational velocity measured as the speed of a specific point on the record increases with the distance of that point from the center, see Fig. 1.7. The movements of the planets around the sun follow the Laws of Kepler³⁸: The rotational velocity of the planets decreases with increasing distance from the sun. In accordance with Newtonian Gravity and General Relativity, this should also be the case for stars rotating around their galactic center. Instead, one observes the rotational velocity of stars to be constant in regions further away from the center. How can this be explained? Assuming Newtonian Gravity and General Relativity to be correct, this could be explained with more mass being present in the outer regions of galaxies than can be observed with our contemporary measuring devices. This hypothetical mass is called *dark matter* due to the assumption that, although it does take part in the gravitational interaction, it does not take part in the electromagnetic interaction, therefore emits no light and is not visible in optical observations. The Standard Model does not foresee dark matter and appropriate particles have not been detected to date. Another explanation for the rotational velocities has been found by modifying Newton's Laws. In short, the discrepancy between the expected and the observed rotational curves of galaxies has not been settled yet.

Another discrepancy between theory and experiment has arisen in the context of the so-called *anomalous magnetic moment of the muon*, also known under the shortcut "*muon g-2*". A moving body can be described by its *momentum*. Intuitively, momentum is a measure for the impact of an object due to its velocity and mass. A car weighing half a ton moving at 30 kilometers per hour has a momentum five times larger than a cyclist on a bicycle weighing 100 kilograms moving at the same speed. For a rotating body such as a planet the corresponding quantity is called angular momentum and the distance to the rotation center plays a role. These momenta are well described in classical Newtonian Physics. The movement of an electron in the atomic shell can

³⁸Johannes Kepler (1571-1630) was a German astronomer and mathematician.

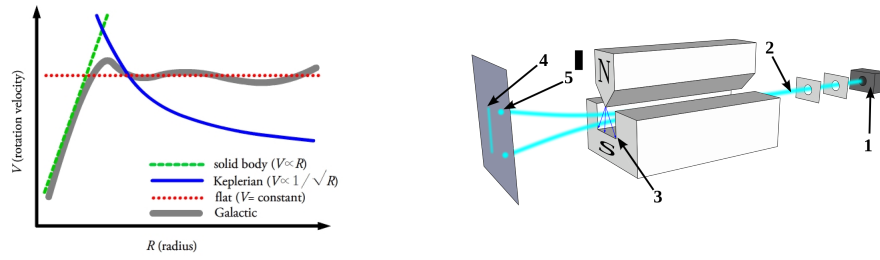


FIGURE 1.7: Left: Rotational curves of a vinyl record (green dashed line), the planets in the Solar system (solid blue line) and the observed rotational curves of galaxies (solid gray line). Illustration by LemonBalmer / CC BY-SA [12]. Right: The Stern–Gerlach experiment. A beam of particles (2) produced at (1) travels through a magnetic field (3). The particles are deflected in two specific directions (5), owing to their Quantum Mechanical spin property. Classical physics predicts the particles to be deflected continuously (4). Illustration by Tatoute / CC BY-SA [13].

be described as a rotation around the atomic nucleus, and the corresponding quantity is called the *orbital angular momentum*. Measurements have shown that the electron possesses an additional characteristic quantity called the *intrinsic angular momentum*, also known as *spin*. This is a genuine Quantum Mechanical effect absent in classical physics³⁹. Based on the angular momentum, a *magnetic moment* can be defined. The Quantum Mechanical correction due to the spin property, also called *anomaly*, can be accounted for by multiplying the classical result with a number, the "muon g-2". In the case of muons, there is a discrepancy between the theoretically calculated and the experimentally measured value of the "muon g-2". This discrepancy is large enough to lead some physicists to assume this might be a hint for BSM physics. Currently, an experiment is ongoing to shed light on this issue⁴⁰.

A third inconsistency between theory and experiment is *neutrino oscillation*. In the Standard Model the neutrino was originally assumed to be massless and the *lepton flavor number*⁴¹ is conserved. Both statements contradict an observation known as neutrino oscillation. Let us begin this discussion with the decay of a muon, see Fig. 1.6. In the first decay process, a muon (μ) decays to a W boson with negative electric charge (W^-) and a *muon neutrino* (ν_μ) in a weak interaction process. The muon neutrino is a neutrino of the second generation - remember that the elementary particles come in three generations. In the second decay process, the W^- decays weakly⁴² into an electron (e)

³⁹The Quantum Mechanical spin property was discovered e.g. in the Stern-Gerlach experiment, see Fig. 1.7.

⁴⁰The experiment is performed at Fermilab in Batavia, Illinois, USA. Data is taken from 2017 until 2020. Check out the public press for results in 2021!

⁴¹The different particle species are distinguished by their flavor. In the case of leptons, the flavors are electron, muon and tau.

⁴²Meaning: in a weak interaction process.

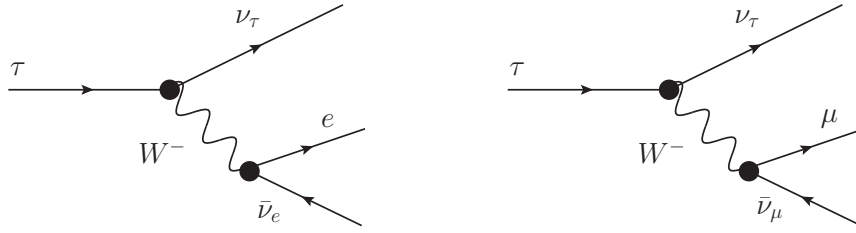


FIGURE 1.8: Left: Electronic decay of the tau. Right: Muonic decay of the tau. Both decays take place at the same rate. This equivalence is known as lepton universality.

and an *anti-electron neutrino* ($\bar{\nu}_e$)⁴³. Let us compare the particles before and after the interactions. Initially, the muon is the only particle. After the decays, we are left with an electron, a muon neutrino and an anti-electron neutrino. First, we check the conservation of electric charge. The muon has a negative electric charge, so does the electron. The neutrinos are electrically neutral. So the net electric charge is conserved. Note that the charge is "carried" from the initial muon to the final electron by the negatively charged mediator, the W^- . Next, we check the conservation of lepton flavor number. The lepton generations are characterized by their *flavors*, thereby distinguishing the electron neutrino, the muon neutrino and the tau-neutrino and their respective anti-particles. The lepton flavor number is +1 for each particle of a specific flavor, -1 for each anti-particle of a specific flavor. The initial muon has zero electronic flavor number and +1 muonic flavor number. In the final state, the muonic flavor number is +1 (stemming from the muon neutrino) and the electric flavor number is zero (as the numbers of the electron and the anti-electron neutrino cancel each other out). So the lepton flavor number is conserved in this decay process, as it should be in accordance with the Standard Model. In experiments, however, it has been observed that neutrinos produced with a certain flavor may later be observed to have changed in flavor. Muon neutrinos produced by cosmic radiation in the atmosphere have been measured before and after passing through part of the earth. The amount of muon neutrinos has been observed to be reduced by up to 50 percent between the first measurement and the second measurement. Most likely, the disappeared fraction was transformed into another neutrino flavor, presumably into tau neutrinos. According to our current theories, a change of flavor is only possible if neutrinos are massive - in contradiction to the Standard Model. This is the phenomenon referred to as neutrino oscillation.

Let me finish this section with some thoughts on *lepton universality*. The weak interaction mediated by the electrically charged bosons W^+ or W^- is equal for all *fermions* (the umbrella term for quarks and leptons). Consequently, the tau is just as likely to decay into an electron as into a muon⁴⁴, see Fig. 1.8. Likewise, an electron in the final state

⁴³The bar-symbol is used to discriminate particles ν_e from anti-particles $\bar{\nu}_e$.

⁴⁴The statement is true up to small effects from the difference in mass of the leptons.

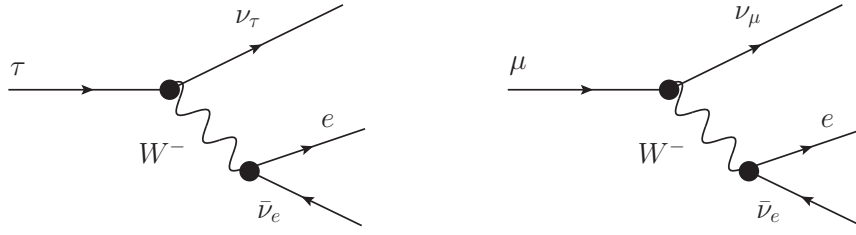


FIGURE 1.9: Left: Electronic decay of the tau. Right: Electronic decay of the muon. Both decays are equally probable due to lepton universality.



FIGURE 1.10: Left: Electronic decay of the B^- meson. Right: Muonic decay of the B^- meson. Lepton universality demands equal rates for both decays⁴⁷.

might just as well stem from a decay process with an initial muon as with an initial tau, as depicted in Fig. 1.9. Theoretical and experimental results are consistent for these decays. As mentioned previously, two quarks can be bound to form a meson - a short-lived particle that will decay soon afterwards. Mesons can decay weakly to fermions. The decay of e.g. B^- mesons made up of a *bottom quark*⁴⁵ and an anti-up quark has been experimentally investigated. According to lepton universality, the electronic decay of the B^- meson should happen just as frequently as the muonic decay. However, recent experimental results have shown an excess of the electronic decay⁴⁶, see Fig. 1.10 [14]. As with the discrepancy for the "muon g-2", this excess is too small to be firm evidence for New Physics beyond the Standard Model and at the same time it is too large to be explained exclusively by the inevitable uncertainties inherent to theory and experiment. Additional more precise experiments and theoretical efforts will hopefully either expand Standard Model or confirm its validity.

In summary, precision physics and searches for New Physics are linked together in constructive tension. In order for New Physics to be validated, physical quantities must be measured ever more precisely. Also, the predictions of the Standard Model must be theoretically calculated ever more accurately, including effects not considered before. Only in case of consistent disagreement between Standard Model based predictions and experimental results can New Physics be established. The current thesis presents a tool to calculate observables⁴⁸ including strong and weak effects in an automated fashion. This tool can be used to study fundamental interactions and decay processes at state of the art accuracy. Its aim is to contribute to the endeavor of providing accurate predictions.

⁴⁵The top and the bottom quark are members of the third generation of quarks.

⁴⁶The statement is true for certain decay channels.

⁴⁸An observable is a physical quantity directly accessible in experiment, e.g. the energy of a particle.

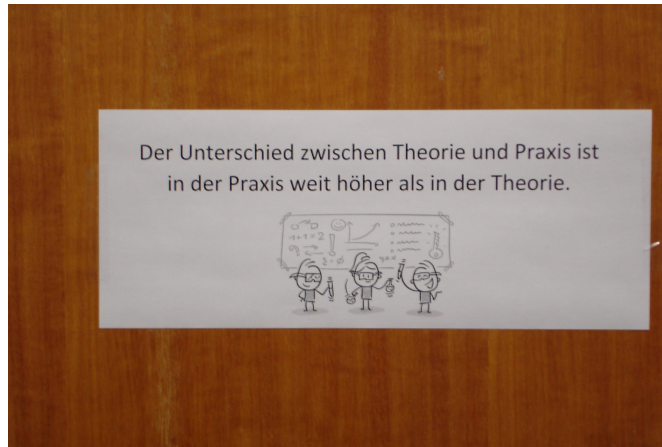


FIGURE 1.11: Cartoon displayed on an office door at the Institute of Exact Sciences of the University of Bern. Photograph by M. Hager.

1.6 Invitation to Cooperate: On the Relation of Theory and Experiment

Elementary particle physics is performed experimentally and theoretically. Roughly speaking, experimental physicists design and perform experiments and analyse the measurement data. Theoretical physicists calculate predictions for the interaction processes based on theoretical foundations, propose new observables and search for new theories attempting to explain discrepancies between theory and experiment. The current thesis contributes to the first task in the domain of theoretical physics. Naturally, theoreticians and experimentalists have different points of view, a fact that is well represented in Fig. 1.11.

As a rule of thumb, experiments always have the last word in case of discrepancies between theory and experiment. I would like to conclude the general introduction with an exception to the rule. From 2006 - 2012, an experiment was conducted to investigate the neutrino oscillations introduced in the previous section⁴⁹. We have seen that neutrinos are produced in decay processes. There are many methods to induce such decay processes. In the aforementioned experiment in Geneva (Switzerland), a beam of protons was directed on a graphite target. This led to the production of mesons, which can decay to muons and muon neutrinos. The particles were sent towards Gran Sasso (Italy), by means of focussing lenses. The muons were absorbed by the rocks en route, while the neutrinos continued their flight and were measured at their destination with a detector specifically constructed for this experiment. Some muon neutrinos were indeed observed to have oscillated to tau neutrinos. In 2011, the collaborators working on the experiment reported that neutrinos had been measured to be travelling faster

⁴⁹The experiment was called "CERN Neutrinos to Gran Sasso".

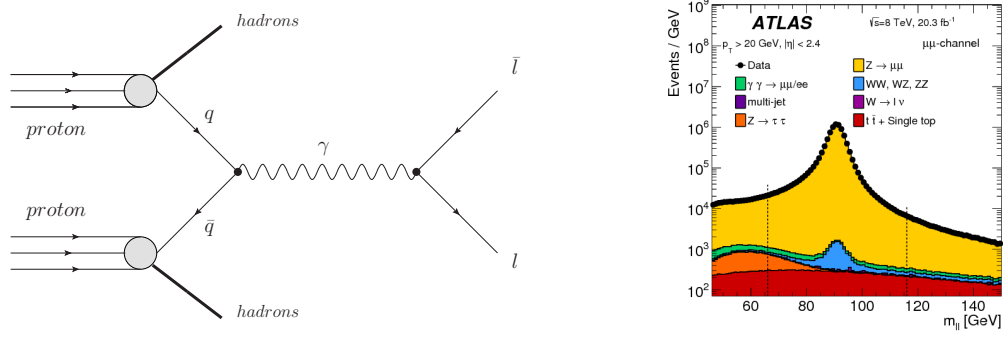


FIGURE 1.12: Left: Photon-mediated Drell-Yan scattering $pp \rightarrow \gamma + X \rightarrow l\bar{l}$. The photon is identified with the greek letter γ . Right: Number of events with respect to the dilepton mass m_{ll} for Drell-Yan scattering [15].

than the speed of light. However, the Special Theory of Relativity states that nothing can travel faster than the speed of light in vacuum, not even a quasi massless neutrino. I was a Bachelor student at the time this news was communicated, and I vividly recall the spell of excitement present at our institute. It was hard to believe that Einstein's theory of Special Relativity, which had persisted - solid as a rock - for over a century, could be challenged by a bunch of superluminal particles travelling through the Alps. It turned out that failures in the experimental setup had lead to false results, and it was later reported that after the equipment had been fixed, the speed of the neutrinos was measured to be in agreement with the speed of light.

1.7 Getting down to Business: An Example Scattering Process

After the general overview everything needed is at hand to immerse ourselves into the details of the research documented in this thesis. I start with the Drell-Yan (DY)⁵⁰ scattering process that was first suggested and measured in 1970. In a *particle accelerator*, two beams of protons are made to travel in opposite directions in separate beam pipes at nearly the speed of light, thereby gaining high energy. The two beams are then brought together, whereby some protons undergo collisions. At high energies this results in a scattering of the constituents. For example, a quark of one proton can interact with an anti-quark of the other proton. In an electromagnetic interaction a photon is produced that subsequently decays to a lepton and an anti-lepton. The remaining constituents of the protons recombine to build hadrons. The example process is schematically depicted in Fig. 1.12 (left).

⁵⁰Sidney D. Drell (1926-2016) was a US-American physicist. Tung-Mow Yan (1937) is a US-American physicist of Taiwanese origin.

A *detector*, an ingenious combination of tracking devices⁵¹, calorimeters⁵² and particle-identification devices⁵³ measures physical observables including energy, mass and charge of the particles left behind after the interaction. If the event shows the characteristics of the process being studied, in our case the two leptons in the *final state* after the interaction, the measurement is recorded. After many such measurements an *event rate*, also called *interaction rate*, can be computed, corresponding to the number of events registered per unit time.

Once the event rate R is known, a quantity called *cross section* can be evaluated. The cross section σ of a specific interaction is a measure of the probability for it to take place. It is defined as

$$\sigma = \frac{\#interactions \cdot \mathcal{A}}{N_A N_B} = \frac{R}{\mathcal{L}}, \quad \text{with} \quad \mathcal{L} = \frac{N_A N_B}{\mathcal{A}}. \quad (1.1)$$

N_i is the number of particles in beam i , and \mathcal{A} is the beam area. The interaction rate R is the number of interactions per time unit, and the luminosity \mathcal{L} is a measure for the performance of the particle accelerator per time unit. The more particles in the beams N_i for a given beam area \mathcal{A} and time unit, the higher the luminosity of the accelerator. The cross section has the dimensions of a surface and is measured in *barns*; $1 \text{ b} = 10^{-28} \text{ m}^2$. The values of N_i and \mathcal{A} can be tuned and the interaction rate R is measured in the experiment, while the cross section σ is a physical quantity independent of the accelerator parameters save for the beam energy, as we shall see further below.

In Fig. 1.12 (right), the outcome of proton-proton scattering to a lepton pair is visualized. The term " $\mu\mu$ -channel" indicates that only events with a muon and an anti-muon in the final state are considered in this plot. The plot shows the *differential* cross section. This is the number of events *with respect to a certain observable*, here the dimuon mass. We see that the number of events changes with the mass. Most events were recorded at a dimuon mass around 90 GeV⁵⁴. We also notice that the yellow area contributes most. It corresponds to the process $pp \rightarrow Z \rightarrow \mu\bar{\mu}$, where the *intermediate state* is a Z boson instead of a photon. It is no coincidence that the peak is at approximately 90 GeV, which is the Z boson mass. Viewing the situation the other way round, the

⁵¹The tracking devices include semiconductors (remember the phototelectric effect), gas-ionisation (remember the cloud chamber) and muon spectrometers. The latter contain magnets to bend the tracks of charged particles like the muon (remember the discovery of the positron), allowing to calculate charges and momenta.

⁵²The calorimeter is designed to absorb most particles coming from a collision, forcing them to deposit their energy within the detector. It consists of dense and highly absorbing material, lead for example.

⁵³Particle-identification devices detect radiation emitted by charged particles. The energy of this radiation or the angle at which the radiation is emitted allow to distinguish different particle types.

⁵⁴The GeV is a unit for mass and energy commonly used in high energy physics. 1 GeV corresponds to 10^9 *electron volt* eV. The mass of an electron is approximately $m_e c^2 \simeq 500\,000 \text{ eV} = 0.5 \text{ MeV}$.

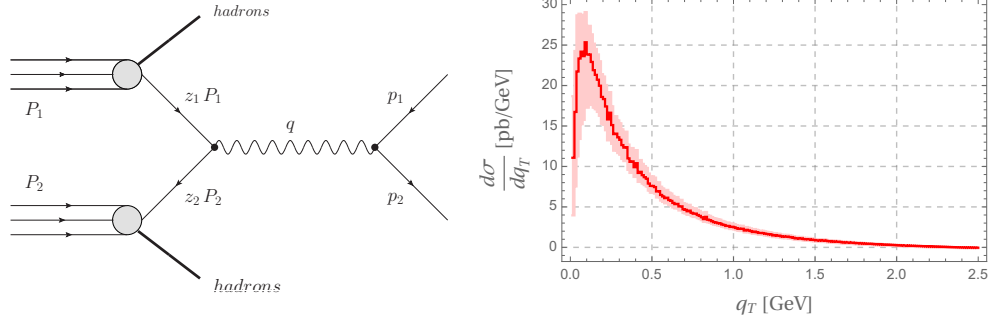


FIGURE 1.13: Left: Kinematic quantities in Drell-Yan scattering. Right: Differential cross section $d\sigma/dq_T$ for Z boson-mediated Drell-Yan scattering.

existence of a peak can be taken as evidence that a particle of a certain mass is in the intermediate state. This phenomenon is known as a *resonance*, and it shows exactly how new particles were and still are discovered.

Another interesting observable is the *transverse momentum*. This is the component of the momentum in the plane transverse to the beams. There is – *per definition* – no transverse momentum in the *initial state* of the two protons before the interaction. Transverse momentum is a conserved quantity, therefore it equals zero also in final state. If only two leptons are produced without additional radiation, they will fly away back to back, with equal momentum in opposite directions.

If the measured total transverse momentum of the final state, including possible radiation, does not add up to zero, then some of it was carried away by particles that were not detected. This is referred to as *missing transverse momentum*, or *missing transverse energy*, respectively. Missing transverse momentum allowed for the discovery of the neutrino, produced in the electroweak decay $W \rightarrow l \nu$. It is also an experimental signature expected in BSM-physics, e.g. in Supersymmetry (SUSY); searches for SUSY particles are based on measuring missing transverse energy.

We shall see very soon that the cross section for DY scattering does indeed depend on transverse momentum, whereby the transverse momentum of the final state is compensated by radiation of the interacting quarks. The understanding of the transverse momentum spectrum in scattering processes, the calculation of the cross section and finally the implementation of this calculation into a framework allowing for an automated evaluation over a wide range of processes and observables, neither limited to the DY process nor to the transverse momentum – that’s what this thesis is all about.

In order to compute the theoretical cross section for our $pp \rightarrow \gamma \rightarrow l \bar{l}$ example process – note that the photon is identified with the greek letter γ – we use methods from

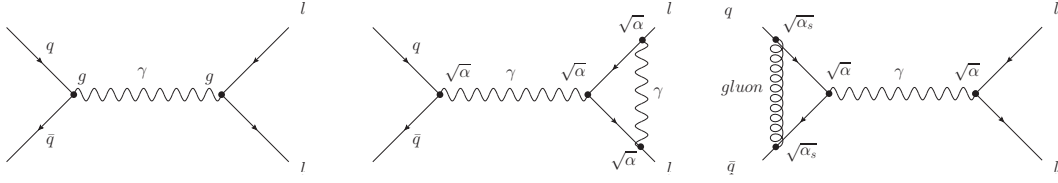


FIGURE 1.14: Left: DY scattering at tree level. Middle: A one-loop diagram for the electromagnetic interaction in DY scattering. Right: A one-loop diagram for the strong interaction in DY scattering. The black blobs are called interaction vertices. The mediators are the photons for the electromagnetic and the gluon for the strong interaction. The coupling constants are α for the electromagnetic and α_s for the strong interaction.

Quantum field theory (QFT). In QFT, physical quantities O are often computed as a series in a *coupling constant* g ,

$$O(\alpha) = \sum c_n g^n = c_0 + c_1 g^2 + c_2 g^4 + \dots, \quad (1.2)$$

where the c_i are coefficients. As long as $g \ll 1$, the subleading terms of order g^4 and higher powers of g are corrections (perturbations) to the leading term $c_0 + c_1 g^2$, hence the series expansion method is also called *perturbation theory*. The process at *tree level* relevant in our example comprises the leading term only. Each *interaction vertex* in the Feynman diagrams in Fig. 1.14 corresponds to a factor g . Based on the diagram, an *amplitude* can be calculated. The *probability* for a process to take place is the square of the amplitude, so that the leading-order (LO) result will be proportional to g^4 . In our example process, which is an electromagnetic interaction, the coupling constant is denoted α , with $\alpha := g^2/4\pi$.

Let's have a look at the kinematic quantities of the DY process, see Fig. 1.13. The colliding protons have four-momenta $P_1 = (E_b, 0, 0, E_b)$ and $P_2 = (E_b, 0, 0, -E_b)$, where E_b is the beam energy of the particle accelerator. The interacting partons carry fractions z_i of the proton momenta, such that $E_i = z_i E_b$ are the energies of the partons in absence of radiation. The intermediate state has momentum $q = (z_1 P_1 + z_2 P_2)$, and we find $q^2 = z_1 z_2 s = M^2$, where M is the mass of the leptonic final state and $s = (P_1 + P_2)^2$. The *rapidity* of the intermediate state is defined as

$$y = \frac{1}{2} \ln \left(\frac{E + q_z}{E - q_z} \right) = \frac{1}{2} \ln \left(\frac{z_1}{z_2} \right), \text{ where } z_1 = \frac{M}{\sqrt{s}} e^y \text{ and } z_2 = \frac{M}{\sqrt{s}} e^{-y}. \quad (1.3)$$

Intuitively, the rapidity is related to the velocity of the intermediate state in one of the beam directions. The larger the parton momentum ratio (z_1/z_2) , the larger the rapidity. The cross section σ for proton-proton scattering to some measured final state Y, as derived e.g. in [16], is

$$\begin{aligned} \sigma(p(P_1) + p(P_2) \rightarrow Y) \\ = \int_0^1 dz_1 \int_0^1 dz_2 \sum_f \phi_f(z_1) \phi_f(z_2) \cdot \sigma(q_f(z_1 P_1) + \bar{q}_f(z_2 P_2) \rightarrow Y), \end{aligned} \quad (1.4)$$

where the sums runs over all quark and anti-quark flavors⁵⁵ up, anti-up, down, etc. The $\phi(z_i)$ are *parton distribution functions* (PDFs) that encode the momentum fraction z_i carried away from the proton by the parton.

At this stage some questions are overdue. The proton being a composite particle made of two up quarks and one down quark, how do we know which quark, the up or the down, takes part in the interaction? Where does the anti-quark come from? How can we know which fraction of the proton momentum the parton carries off? The first two questions can be answered as follows. As already suggested, the substructure of the proton is not limited to the up and down quarks, which are also called *valence quarks*. Rather, it can be pictured as containing all quark and anti-quark flavors as well as gluons, the mediators of the strong interaction. These constituents are called *sea quarks*. The sea quarks also participate in interactions, though with a smaller probability than the valence quarks. The mentioned scattering experiments of the late sixties have shown that though we cannot predict the momentum of a specific parton, we can extract the *probability* for it to keep a certain fraction of the proton momentum.

In Fig. 1.15 the left diagram shows the cross section of a scattering experiment with respect to the momentum fraction x of the interacting quark⁵⁶. The experiment was performed at various initial energies and scattering angles of the projectile. The plot shows a characteristic distribution of measurement values that was shown to be independent of the energies and angles. Phenomenologically speaking, this means that the substructure of a proton looks roughly the same for a projectile no matter how hard it strikes the proton. Based on this finding, many scattering processes with different interaction partners were performed, so that the probability distributions of the momentum fractions for the different partons could be tabulated.

The right diagram shows these distributions for the proton. We notice that for any momentum fraction x it is more probable to find an up quark than a down quark. It is also more probable to find a quark than an anti-quark of a certain flavor, and it is more probable to find quarks of the first generation than of the second. We also see that for small fractions of x the gluons dominate by far. These findings are purely empirical and no method is known for finding the PDFs analytically.

⁵⁵As with the leptons, the different species of the quark are referred to as “flavors”.

⁵⁶For the sake of comprehensibility, we are slightly simplifying things. The plot shows $d\sigma/dxdQ^2$ divided by a factor (depending on Q^2 , x and s) against x , where Q is the momentum transferred to the target by the projectile. The identification of x with the momentum fraction is only valid at LO.



FIGURE 1.15: Left: The cross section of deep inelastic scattering with respect to the momentum fraction x of the interacting quark and the momentum transfer Q^2 of the electron for various initial electron energies and scattering angles. Right: Parton distribution functions for the proton at $Q^2 = 4 \text{ GeV}^2$. Illustrations from [16].

The formula for the interaction of a quark with an anti-quark of flavor f to produce a lepton pair is

$$\sigma(q_f \bar{q}_f \rightarrow l^+ l^-) = \frac{1}{3} Q_f^2 \cdot \frac{4\pi\alpha^2}{3M^2}, \quad (1.5)$$

where Q_f^2 is the square of the quark electric charge of the quark and M^2 is the dilepton mass squared. The coupling constant α of the electromagnetic interaction is also called the *fine-structure constant*. The cross section σ for photon-mediated DY scattering at leading order is

$$\sigma(pp \rightarrow l^+ l^-) = \int_0^1 dz_1 \int_0^1 dz_2 \sum_f \phi_f(z_1) \phi_f(z_2) \cdot \frac{1}{3} Q_f^2 \cdot \frac{4\pi\alpha^2}{3M^2}. \quad (1.6)$$

Let's also compute the *differential cross section* $d\sigma/dM^2 dy$ which is the cross section with respect to the physical observables M^2 and y . Computing the Jacobian for the change of variables using relation (1.3), we find $dz_1 dz_2 s = dM^2 dy$ and

$$\frac{d\sigma}{dM^2 dy}(pp \rightarrow l^+ l^- + X) = \sum_f z_1 \phi_f(z_1) z_2 \phi_f(z_2) \cdot \frac{1}{3} Q_f^2 \cdot \frac{4\pi\alpha^2}{3M^4}. \quad (1.7)$$

In the next chapter, I present a formula for the cross section that is more realistic than the one presented here for the process at tree level. I first discuss the formula qualitatively, then outline its derivation using an *effective theory*. In the remaining chapters I describe how the different factors of the formula are worked out and implemented into a computational framework. Finally results generated using this framework are discussed.

Chapter 2

Preparation of Tools

If you want to go far, go slow.

anonymous

2.1 Going Beyond Tree Level: The Factorization Formula for Small Transverse Momentum

Now that we have dwelled on the DY-process at tree level, let's analyze the following two modifications: We want to consider radiation of the interacting partons, and we want to include next-to-leading order effects in the strong interaction of the quarks. We do not go beyond the leading order in the electromagnetic interaction because the NLO-terms are smaller than the pursued accuracy of a few percent. In the strong interaction however we include the next-to-leading (NLO) order because it differs from the tree-level result by 20 to 30 percent¹. To encode the radiation, we construct a *beam function* \bar{B} . Both improvements are illustrated in Fig. 2.1. The beam function combines the PDFs known from the tree-level process with a function \bar{I} that encodes the radiation of quarks and gluons by the interacting partons. The following factorization formula for photon-mediated Drell-Yan scattering given in [1] meets these requirements:

$$\begin{aligned} \frac{d\sigma}{dM^2 dq_T^2 dy} &= \frac{4\pi\alpha^2}{9M^2 s} |C_V(-M^2, \mu)|^2 \frac{1}{4\pi} \int d^2x_\perp e^{-iq_\perp \cdot x_\perp} e^{g_F(\eta_F, L_\perp, \alpha_s)} \\ &\times \sum_q e_q^2 [\bar{B}_i(\xi_1, x_\perp, \mu) \bar{B}_j(\xi_1, x_\perp, \mu) + (q \leftrightarrow \bar{q})] . \end{aligned} \quad (2.1)$$

¹One can assess the relative strenghts of the strong and the electromagnetic interaction by comparing the decay times of short-lived hadrons through the respective interaction. The decay time is inversely proportional to the strength of the coupling. One finds that the strong interaction is around 100 times stronger than the electromagnetic interaction.

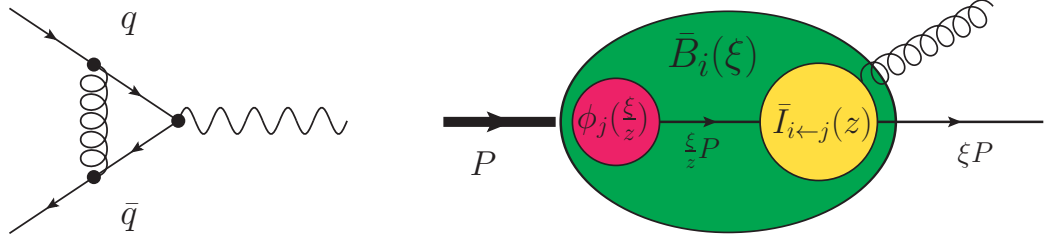


FIGURE 2.1: Left: Feynman diagram of the strong interaction at order $\mathcal{O}(\alpha_s)$ (NLO). Right: Beam function \bar{B} and kinematical details of the radiation.

On the left-hand side of the equation, we have the differential cross section with respect to the dilepton mass squared M , the rapidity y and the transverse momentum squared q_T^2 . In the first factor on the right-hand side, together with the sum over quark charges $\sum_q e_q^2$, we recognize the tree-level result (1.5) for the electromagnetic interaction of a quark with an anti-quark to produce a lepton pair. The factor $|C_V(-M^2, \mu)|^2$ includes terms up to order NLO of the series in the coupling α_s of the strong interaction. The quantity C_V is called a *Wilson coefficient*², and the subscript V raises awareness for the fact that the coefficient is related to a vector, the gluon in our case. As usual, M is the mass of the leptonic final state. For the origin of the minus sign, see Fig. 2.3. The variable μ appearing here for the first time is the *factorization scale* – the scale at which we choose to evaluate the different factors. It has no physical meaning, a fact that we will make use of in our calculations. The term in brackets on the second line encodes the radiation. It is part of a Fourier integral, where the integration d^2x_\perp runs over the transverse plane. While this term will be analysed in detail in Chapter 3, let me illustrate the basic mechanism by means of the beam function

$$\bar{B}_i(\xi, x_\perp, \mu) = \sum_j \int_\xi^1 \frac{dz}{z} \bar{I}_{i \leftarrow j}(z, x_\perp, \mu) \phi_j(\xi/z, \mu). \quad (2.2)$$

As seen in the tree-level interaction, a certain fraction of the proton momentum is carried away by a parton. The parton can then undergo radiation processes, so that finally a momentum fraction ξ is left to interact. The beam function depends on the momentum fraction ξ left after radiation, while the function \bar{I} depends on a variable called z . For $z = 1$, no emission takes place and the beam function \bar{B} reduces to the PDF ϕ . For $z = \xi$ the parton takes all of the proton momentum, $\xi/z = 1$. The integral runs over all values $z \in (\xi, 1)$, so that the beam function encodes all possible radiation, given a ξ , up to a certain accuracy called NNLL that will be explained later on.

To access the transverse momentum spectrum of the electroweak final state, we integrate over M^2 and y . The cross section $d\sigma/dq_T$ can be found by using the relation

²Kenneth G. Wilson (1936) is a US-American physicist.

$$\frac{d\sigma}{dq_T} = 2q_T \frac{d\sigma}{dq_T^2}. \quad (2.3)$$

Fig. 1.13 shows the transverse momentum spectrum $d\sigma/dq_T$ for the Drell-Yan process $pp \rightarrow Z + X \rightarrow l\bar{l}$ computed using formula (2.1). The X denotes hadronic states including the radiation we are interested in. Most interactions take place at small transverse momentum q_T around 5 GeV of the lepton pair and hardly any events occur with $q_T > 80$ GeV. This finding agrees well with experimental results.

2.2 Knowing our Limits: Effective Field Theories

The factorization formula (2.1) has been derived using an *effective theory*. An effective (field) theory aims at explaining some aspects of a problem, as opposed to explaining everything. In this sense, every physical theory is an effective theory, as we have not found “The Theory of Everything” yet. As I have exposed in the introduction, the Standard Model is an effective theory in the sense that it can explain many, albeit not all physical phenomena below the Planck scale. In an effective theory, one is allowed to simplify things as long as the effects of the simplification are negligible compared to the relevant quantities of the problem at hand. It has been pointed out in the introduction that Quantum Mechanics as a non-relativistic theory is very successful at describing the hydrogen and the helium atom as well as many more atomic phenomena. For understanding atoms it is not necessary to take into account the substructure of the nucleus, let alone of the nucleons. The atomic nucleus can be considered point-like, charged and – because it is many orders of magnitudes heavier than the electron – to a good approximation as fixed in space. This illustrates in what way Quantum Mechanics is an effective theory.

Let’s work out some useful simplifications for our scattering process. In view of the fact that the masses of the interacting partons are many orders of magnitude smaller than the mass of the leptonic final state M , the partons can be considered massless. The observable q_T of interest is also much smaller than M , so the ratio q_T/M might be a useful parameter for a series expansion. The momenta of the incoming partons are oriented along the beam directions, and we are also interested in the momenta in the transverse plane stemming from radiation. Therefore we should adapt the coordinate system to this situation. These properties, amongst others, are incorporated into the effective theory called Soft-Collinear Effective Theory (SCET). SCET will prove to be well suited for deriving the factorization formula and will be introduced in the next section.

2.3 Deriving the Factorization Formula: An Adventurous Journey

2.3.1 The 2 to 2 Scattering Process

We are interested in the scattering of two protons with momenta P_1 and P_2 to a measured final state with two leptons carrying momenta p_+ and p_- and hadronic states X with momentum p_X ,

$$p(P_1) + p(P_2) \rightarrow p_+ + p_- + p_X. \quad (2.4)$$

The general cross section formula for this process is

$$d\sigma = \frac{d\Pi_{LIPS}}{2s} |\langle p_+, p_-, p_X | P_1, P_2 \rangle|^2 (2\pi)^4 \delta^{(4)}(p_+ + p_- + p_X - P_1 - P_2), \quad (2.5)$$

We denote the integration over the phase space of the states X as \sum_X and the momentum of the leptons as $q = p_+ + p_-$. The second property is implemented in the cross section by a factor $d^4q \delta^{(4)}(q - p_+ - p_-) = 1$. Also, we replace the delta-distribution in Eq. (2.5) by its Fourier representation,

$$(2\pi)^4 \delta^{(4)}(q + p_X - P_1 - P_2) = \int d^4x e^{i(P_1 + P_2 - q - p_X)x}, \quad (2.6)$$

to get

$$\frac{d\sigma}{d^4q} = \frac{d\Pi_{LIPS}}{2s} \delta^{(4)}(q - p_+ - p_-) \int d^4x \sum_X |\langle p_+, p_-, p_X | P_1, P_2 \rangle|^2 e^{i(P_1 + P_2 - q - p_X)x}, \quad (2.7)$$

where $d\Pi_{LIPS}$ is the Lorentz-invariant phase space,

$$d\Pi_{LIPS} = \frac{d^3\vec{p}_+}{(2\pi)^3} \frac{1}{2E_+} \frac{d^3\vec{p}_-}{(2\pi)^3} \frac{1}{2E_-}. \quad (2.8)$$

In the following it will be useful to work with *currents*. The fermion vector current J^μ is of the form $\bar{\psi}\gamma^\mu\psi$. In our case, the currents are related to the symmetry transformation

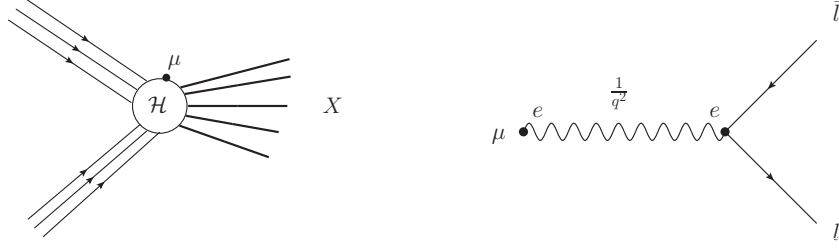


FIGURE 2.2: Left: The hadronic part of the interaction. Right: The leptonic part of the interaction.

$\psi \rightarrow e^{-i\kappa}\psi$ of the Lagrangian \mathcal{L} that will be introduced in the next section. Using *Noether's Theorem*³, we find

$$J^\mu = \frac{\partial \mathcal{L}}{\partial(\partial\psi)} \frac{\delta\psi}{\delta\kappa} = \bar{\psi}\gamma^\mu\psi. \quad (2.9)$$

This is the current for the electromagnetic interaction of fermions. We will write the current for the electromagnetic interaction of quarks as $J^\mu = \sum_q e_q \bar{\psi}_q \gamma^\mu \psi_q$, where the sum \sum_q is taken over quark flavors and the e_q are the quark charges. As we are working to leading order in the electromagnetic interaction, and because leptons do not interact strongly, the leptonic part of the scattering amplitude $\langle p_+, p_-, p_X | P_1, P_2 \rangle$ factorizes from the hadronic part. This situation is sketched in Fig. 2.2, and the two contributions are given by

$$\frac{e^2}{q^2} \bar{u}(p_-) \gamma^\mu v(p_+), \quad \langle p_X | J^\mu(0) | P_1, P_2 \rangle. \quad (2.10)$$

In the leptonic part $\frac{1}{q^2}$ stems from the photon propagator and we have used $\alpha = e^2/4\pi$. In the hadronic part we use the current operator introduced above. The cross section can now be written as the product of a lepton tensor $L_{\mu\nu}$ and a hadron tensor $W_{\mu\nu}$,

$$\frac{d\sigma}{d^4q} = \frac{1}{2s} \frac{e^4}{(q^2)^2} L_{\mu\nu} W^{\mu\nu}, \quad (2.11)$$

with the two tensors

$$L_{\mu\nu} = \int \frac{d^3\vec{p}_+}{(2\pi)^3 2E_+} \frac{d^3\vec{p}_-}{(2\pi)^3 2E_-} \delta^{(4)}(q - p_+ - p_-) \sum_s \bar{u}(p_-) \gamma_\nu v(p_+) \bar{u}(p_-) \bar{v}(p_+) \gamma_\mu u(p_-) \quad (2.12)$$

³Emmi Noether (1882-1935) was a German mathematician.

and

$$W_{\mu\nu} = \int d^4x \sum_X \langle P_1, P_2 | J_\mu^\dagger(0) | X \rangle \langle X | J_\nu(0) | P_1, P_2 \rangle e^{i(P_1 + P_2 - q - p_X)x}. \quad (2.13)$$

The lepton tensor is evaluated using $g^{\mu\nu} L_{\mu\nu}$ and the sum \sum_s is taken over final spins. We use the translation operator to replace $J_\mu^\dagger(0) = e^{-iP_x} J_\mu^\dagger(x) e^{iP_x}$ in the hadron tensor. Applying the relation $\sum_X |X\rangle \langle X| = \mathbb{1}$ we find the result

$$d\sigma = \frac{4\pi\alpha^2}{3q^2s} \frac{d^4q}{(2\pi)^4} \int d^4x e^{-iq \cdot x} (-g_{\mu\nu}) \langle P_1, P_2 | J_\mu^\dagger(x) J_\nu(0) | P_1, P_2 \rangle. \quad (2.14)$$

The formula above is the starting point for the factorization that will be elaborated using the effective theory SCET. In the next section, I introduce the formalism needed herefore.

2.3.2 SCET Kinematics and Lagrangian

Since we consider large momentum in the beam directions and small transverse momentum q_T , we prefer to work with momenta along the beam directions called collinear and anti-collinear and soft momenta meaning small energies in all directions. These properties are encoded using two light cone vectors

$$n_\mu \equiv (1, 0, 0, 1), \quad \bar{n}_\mu \equiv (1, 0, 0, -1). \quad (2.15)$$

Due to

$$n^2 = \bar{n}^2 = 0, \quad n \cdot \bar{n} = 2, \quad (2.16)$$

these reference vectors are suited to describe massless particles propagating at the speed of light. Any vector $k^\mu = (k_0, k_x, k_y, k_z)$ can be decomposed into three components called $(+, -, \perp)$, where

$$\begin{aligned} k^\mu &= k_+^\mu + k_-^\mu + k_\perp^\mu = (n \cdot k) \frac{\bar{n}^\mu}{2} + (\bar{n} \cdot k) \frac{n^\mu}{2} + k_\perp^\mu \\ &= (k_0 + k_z) \frac{\bar{n}^\mu}{2} + (k_0 - k_z) \frac{n^\mu}{2} + k_\perp^\mu \equiv \underbrace{(n \cdot k)}_+ \underbrace{(\bar{n} \cdot k)}_- + k_\perp^\mu. \end{aligned} \quad (2.17)$$

The four-vector $k_\perp^\mu = (0, k_x, k_y, 0)$ is related to the two-dimensional vector $\vec{k}_T = (k_x, k_y)$ by $k_\perp^2 = -|\vec{k}_T|^2 = -k_T^2 = -k_x^2 - k_y^2 \neq 0$. The scalar product of two vectors p^μ and x^μ is

$$p \cdot x = p_+ \cdot x_- + p_- \cdot x_+ + p_\perp \cdot x_\perp. \quad (2.18)$$

The two relevant scales for the processes of interest are the transverse momentum q_T and the invariant mass M of the leptonic final state, so $\lambda = q_T/M$ is a small expansion parameter. With these considerations in mind, the relevant momenta called collinear (c), anti-collinear (\bar{c}) and soft (s) scale as

$$p_c = M(\lambda^2, 1, \lambda), \quad p_{\bar{c}} = M(1, \lambda^2, \lambda), \quad p_s = M(\lambda^2, \lambda^2, \lambda^2). \quad (2.19)$$

Fields are introduced for each sector, the quark fields ψ and the gluon fields A^μ as

$$\psi(x) \rightarrow \psi_c(x) + \psi_{\bar{c}}(x) + \psi_s(x), \quad A^\mu(x) \rightarrow A_c^\mu(x) + A_{\bar{c}}^\mu(x) + A_s^\mu(x). \quad (2.20)$$

Using *projection operators*

$$P_+ = \frac{\not{n} \not{\bar{n}}}{4} \quad \text{and} \quad P_- = \frac{\not{\bar{n}} \not{n}}{4} \quad (2.21)$$

satisfying $P_\pm^2 = P_\pm$ and $P_+ + P_- = \mathbb{1}$, the collinear field ψ_c can be further decomposed into

$$\psi_c(x) = P_+ \psi_c(x) + P_- \psi_c(x) = \xi(x) + \eta(x). \quad (2.22)$$

Checking the scaling of the different components of the field ψ (see A.1), we find

$$\xi \sim \lambda, \quad \eta \sim \lambda^2, \quad \psi_s \sim \lambda^3. \quad (2.23)$$

Each component of the gluon field A^μ scales as its momentum. For the collinear gluon field A_c^μ we have

$$n \cdot A_c \sim \lambda^2, \quad \bar{n} \cdot A_c \sim 1, \quad A_{c\perp} \sim \lambda, \quad (2.24)$$

and all components of the soft field A_s^μ scale as λ^2 . The Lagrangian of SCET for our problem can be written as

$$\mathcal{L}_{SCET} = \mathcal{L}_c + \mathcal{L}_{\bar{c}} + \mathcal{L}_s, \quad (2.25)$$

where \mathcal{L}_c and $\mathcal{L}_{\bar{c}}$ describe the contributions (anti-) collinear to the beams and \mathcal{L}_s the soft contributions. While at first sight this seems to make everything more complicated, it will turn out that after the due transformations we are left with few terms only. The collinear Lagrangian for massless fermions and the covariant derivative read

$$\begin{aligned} \mathcal{L}_c &= \bar{\psi}_c i \not{D} \psi_c, \\ iD_\mu &= i\partial_\mu + gA_\mu = i\partial_\mu + g(A_{c\mu}^a + A_{s\mu}^a) t^a, \end{aligned} \quad (2.26)$$

where g is the coupling constant and t^a are the generators of SU(3). After some transformations (see A.2) we are left with

$$\mathcal{L}_c = \bar{\xi} \left[in \cdot D + i \not{D}_{c\perp} \frac{1}{in \cdot D_c} i \not{D}_{c\perp} \right] \frac{\not{n}}{2} \xi, \quad (2.27)$$

where

$$\begin{aligned} iD_c &= i\partial + gA_c, \\ in \cdot D &= in \cdot \partial + gn \cdot A_c + gn \cdot A_s. \end{aligned} \quad (2.28)$$

The component η of the collinear fermion field which is power suppressed compared to ξ is not present any more in the Lagrangian. The collinear gluon Lagrangian and the soft Lagrangian read

$$\begin{aligned} \mathcal{L}_c &= -\frac{1}{4} (F_c^a)_{\mu\nu} (F_c^a)^{\mu\nu} \\ \mathcal{L}_s &= \bar{\psi}_s i \not{D}_s \psi_s - \frac{1}{4} (F_s^a)_{\mu\nu} (F_s^a)^{\mu\nu}, \end{aligned} \quad (2.29)$$

with the soft covariant derivative $iD_s = i\partial + gA_s$. Let's direct our attention to soft-collinear interactions. Soft-collinear interactions involving soft quarks do not appear at leading order in the effective Lagrangian, since $\psi_s \sim \lambda^3$ is power suppressed with respect to all other fermion and gluon components. The soft contributions can therefore stem only from gluons. Comparing the collinear gluon field A_c with the soft gluon field A_s , we find that all components of the soft field are suppressed with respect to the collinear field, except for $n \cdot A_s \sim \lambda^2 \sim n \cdot A_c$ (2.24). For this reason, only the component $n \cdot A_s$ enters the soft-collinear interactions. The term $n \cdot A_s$ is part of the derivative $n \cdot D$ (2.28),

and this gives rise to interactions between soft gluons and collinear fermions. The same procedure also works for soft-collinear gluon-gluon interactions by defining

$$igF_{\mu\nu}^c := [iD_\mu^c, iD_\nu^c] \rightarrow [iD_\mu, iD_\nu], \quad (2.30)$$

where $iD_\mu = iD_\mu^c + gn \cdot A_s \frac{\bar{n}_\mu}{2}$. Basing on the above considerations, in the collinear Lagrangian the gluon field reduces to

$$A^\mu(x) \rightarrow (n \cdot A_c(x) + n \cdot A_s(x)) \frac{\bar{n}^\mu}{2} + \bar{n} \cdot A_c(x) \frac{n^\mu}{2} + A_{c\perp}^\mu. \quad (2.31)$$

The final result for the Lagrangian reads

$$\mathcal{L}_{SCET} = \bar{\psi}_s i \not{D}_s \psi_s + \bar{\xi} \left[in \cdot D + i \not{D}_{c\perp} \frac{1}{i\bar{n} \cdot D_c} i \not{D}_{c\perp} \right] \frac{\not{n}}{2} \xi - \frac{1}{4} (F_{\mu\nu}^{s,a})^2 - \frac{1}{4} (F_{\mu\nu}^{c,a})^2. \quad (2.32)$$

The anti-collinear sector \bar{c} in the Lagrangian can be obtained by replacing $n^\mu \leftrightarrow \bar{n}^\mu$ in the collinear sector. We now perform the *multipole (or derivative) expansion* that serves to keep the unsuppressed contributions only. In soft-collinear interactions, the momentum dominated by the collinear contribution scales as $(\lambda^2, 1, \lambda)$. The spacetime point x is conjugate to the momentum and therefore has scaling $(1, \lambda^{-2}, \lambda^{-1})$. Only the term $x_- \cdot \partial_+ A_s \sim \lambda^{-2} \cdot \lambda^2 \sim 1$ gives a contribution. Here we have used the fact that all derivatives⁴ of the soft field scale as λ^2 . The Taylor expansion is therefore performed in the component x_- ,

$$\begin{aligned} A_s(x) &= A_s(x_-) + (x - x_-) \cdot \partial A_s(x_-) + \frac{1}{2} (x - x_-)^2 \cdot \partial^2 A_s(x_-) + \dots \\ &= A_s(x_-) + \underbrace{x_+ \cdot \partial_- A_s(x_-)}_{\mathcal{O}(\lambda^2)} + \underbrace{x_\perp \cdot \partial_\perp A_s(x_-)}_{\mathcal{O}(\lambda)} + \mathcal{O}(\lambda^2). \end{aligned} \quad (2.33)$$

The expansion shows that the field $A_s(x)$ can be rewritten as $A_s(x_-)$ up to first order in λ for soft-collinear interactions.

2.3.3 Matching of the Current

After these considerations we return to the current operator that first appeared in Section 2.3.1 which we write as

⁴The quantum mechanical momentum operator is $p = -i\hbar\partial_x$. Hence all derivatives scale as the corresponding momenta.

$$J^\mu(x) = \bar{\psi}(x) \gamma^\mu \psi(x). \quad (2.34)$$

The effective theory (SCET) is constructed through a matching procedure with the full theory (QCD). It can be shown that the terms of the SCET-Lagrangian do not receive any matching corrections, while the current operator does:

$$J_{QCD}^\mu = C_V J_{SCET}^\mu. \quad (2.35)$$

The Wilson factor C_V is called a *matching coefficient*. When constructing a current in an effective theory one writes down all possible terms including the fields and their derivatives allowed by symmetry and *gauge invariance*. Gauge invariance is discussed in the Appendix (see A.3). Higher order terms in the parameter λ can be dropped. Derivatives of collinear fields, scaling as the field itself, and are not suppressed in the (anti-) collinear sectors. This amounts to *non-localities* in the (anti-) collinear directions. The non-local current operator⁵ can therefore be written as

$$J^\mu(x) = \int ds \int dt C_V(s, t) \bar{\psi}_c(x + s\bar{n}) \gamma^\mu \psi_{\bar{c}}(x + tn), \quad (2.36)$$

where tn and $s\bar{n}$ are displacements in the (anti-) collinear directions. Non-local operators are not gauge invariant. Fortunately a product of fields at different spacetime points can be rendered gauge invariant if the fields are connected by *Wilson lines* $W(x)$ (see A.4). Using Wilson lines we can define gauge invariant fermion fields

$$\chi(x) = W^\dagger(x) \psi(x), \quad \bar{\chi}(x) = \bar{\psi}(x) W(x). \quad (2.37)$$

Now we construct the gauge invariant current operator

$$J^\mu(x) = \int ds \int dt C_V(s, t) \bar{\chi}_c(x + s\bar{n}) \gamma_\perp^\mu \chi_{\bar{c}}(x + tn). \quad (2.38)$$

Only γ_\perp contributes to the expression above.⁶ Now we return to the soft-collinear interaction term in the Lagrangian (2.32),

$$\bar{\xi} \frac{\not{n}}{2} i n \cdot D \xi. \quad (2.39)$$

⁵A non-local operator contains fields evaluated at different points in spacetime.

⁶ γ^μ can be decomposed as $\gamma^\mu = \gamma_\perp^\mu + \not{n} \frac{\bar{n}^\mu}{2} + \not{\bar{n}} \frac{n^\mu}{2}$. We have seen (see Appendix A.1) that $\not{n} \not{n} = 0 = \not{\bar{n}} \not{\bar{n}}$. So $\bar{\chi}_c(\not{n} + \not{\bar{n}}) \chi_{\bar{c}} = 0$ also.

The soft field $A_s(x)$ has been multipole-expanded (2.33), so the covariant derivative D is

$$in \cdot D = in \cdot \partial + gn \cdot A_c(x) + gn \cdot A_s(x_-). \quad (2.40)$$

We now redefine the collinear fields using soft Wilson lines $S(x)$,

$$\begin{aligned} \xi(x) &\rightarrow S_n(x_-)\xi(x)^{(0)} \\ A_c^\mu(x) &\rightarrow S_n(x_-)A_c^{(0)\mu}S_n^\dagger(x_-), \end{aligned} \quad (2.41)$$

where the superscript “(0)” denotes a *decoupled* field. One can check that after this redefinition the derivative D no longer depends on the soft sector,

$$in \cdot D\xi \rightarrow S_n(x_-)in \cdot D_c^{(0)}\xi^{(0)}, \quad D_c^{(0)} := \partial - igA_c^{(0)}(x). \quad (2.42)$$

The term (2.39) now reads

$$\bar{\xi} \frac{\not{n}}{2} in \cdot D\xi \rightarrow \bar{\xi}^{(0)} \frac{\not{n}}{2} in \cdot D_c^{(0)}\xi^{(0)}, \quad (2.43)$$

and the soft gluon field is no longer present. It has been decoupled from the collinear Lagrangian, hence the transformation (2.41) is termed a *decoupling transformation*. The current now is

$$J^\mu(x) = \int ds \int dt C_V(s, t) \bar{\chi}_c^{(0)}(x + s\bar{n}) S_n^\dagger(x_-) S_n(x_+) \gamma_\perp^\mu \chi_c^{(0)}(x + tn). \quad (2.44)$$

This current describes an energetic quark in the direction of P_1 and an anti-quark in the direction of P_2 . We keep in mind that there is a second contribution in which the directions of the quark and the anti-quark are interchanged. Again we perform the multipole-expansion. The momentum of a collinear-anti-collinear interaction scales as $(1, 1, \lambda)$, and the conjugate spacetime point x as $(1, 1, \lambda^{-1})$. Keeping in mind that the derivatives scale as the fields, we find that for the collinear field $\chi_c^{(0)}$ the terms $x_+ \cdot \partial_- \chi_c^{(0)}$ and $x_\perp \cdot \partial_\perp \chi_c^{(0)}$ give contributions of order 1. We therefore expand $\chi_c^{(0)}$ in $x_+ + x_\perp$ (and $\chi_c^{(0)}$ in $x_- + x_\perp$ accordingly). Since the derivatives of the soft fields scale as λ^2 , there is no contribution of order 1, and the soft Wilson lines are evaluated at $x = 0$. The result after expansion reads

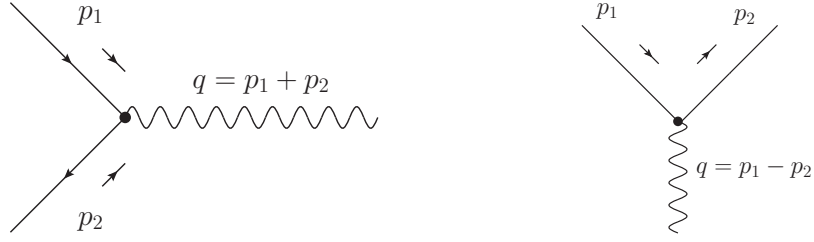


FIGURE 2.3: Left: Timelike momentum q with $q^2 = M^2 > 0$. Right: Spacelike momentum q with $q^2 = -M^2 < 0$. The mass squared M^2 is a physical observable and therefore always positive.

$$J^\mu(x) = \int ds \int dt C_V(s, t) \bar{\chi}_c^{(0)}(x_+ + x_\perp + s\bar{n}) S_n^\dagger(0) S_{\bar{n}}(0) \gamma_\perp^\mu \chi_{\bar{c}}^{(0)}(x_- + x_\perp + tn). \quad (2.45)$$

This result can now be inserted back into expression (2.13). As the different fields have been decoupled, the hadronic tensor $W_{\mu\nu}$ factorizes into a soft and collinear matrix elements,

$$W_{\mu\nu} \sim \langle \text{soft} \rangle \times \langle \text{collinear} \rangle. \quad (2.46)$$

It turns out that the soft contribution evaluates to 1 in the final result. The matrix elements of the collinear fields correspond to the PDFs. Details of these transformations can be found in [4] from page 55 onwards. We write the matrix element $(-g_{\mu\nu}) \langle P_1, P_2 | J_\mu^\dagger(x) J_\nu(0) | P_1, P_2 \rangle$ in (2.14) as

$$\frac{1}{N_c} |C_V(-M^2, \mu)|^2 \sum_q e_q^2 \times \langle P_1 | \bar{\chi}_c^{(0)}(x_+ + x_\perp) \frac{\not{n}}{2} \chi_c^{(0)}(0) | P_1 \rangle \langle P_2 | \bar{\chi}_{\bar{c}}^{(0)}(0) \frac{\not{\bar{n}}}{2} \chi_{\bar{c}}^{(0)}(x_- + x_\perp) | P_2 \rangle,$$

where N_C is the number of colors. The Wilson coefficient depends on the *factorization scale* μ and on $-M^2$. Note the first appearance of a factorization scale in this section. This indicates that the corresponding quantity has been *renormalized*. The step from the bare to the renormalized Wilson coefficient is shown in more detail in Section 3.1. While the physical mass squared M^2 is always a positive quantity, the momentum transfer can be spacelike with $q^2 < 0$, as shown in Fig. 2.3. This is the origin of the minus sign in the arguments of the Wilson coefficient: it was originally calculated for a process with spacelike momentum transfer. The cross section now reads

$$\begin{aligned}
d\sigma &= \frac{4\pi\alpha^2}{3N_c q^2 s} \frac{d^4 q}{(2\pi)^4} \int d^4 x e^{-iq \cdot x} |C_V(-M^2, \mu)|^2 \sum_q e_q^2 \\
&\times \langle P_1 | \bar{\chi}_c(x_+ + x_\perp) \frac{\not{q}}{2} \chi_c(0) | P_1 \rangle \langle P_2 | \bar{\chi}_{\bar{c}}(0) \frac{\not{q}}{2} \chi_{\bar{c}}(x_- + x_\perp) | P_2 \rangle.
\end{aligned} \tag{2.47}$$

Here the superscripts “(0)” of the collinear fields have been dropped for convenience.

2.3.4 From PDFs to Beam Functions

We now turn our attention to the collinear matrix elements. Using SCET operators, the PDFs read

$$\phi_{q/P}(z, \mu) = \frac{1}{2\pi} \int dt e^{-izt\bar{n} \cdot P} \langle P | \bar{\chi}_c(t\bar{n}) \frac{\not{t}}{2} \chi_c(0) | P \rangle. \tag{2.48}$$

We see that the standard PDFs are not suitable for our analysis that contains the *transverse displacement* vector x_\perp . One therefore defines *transverse PDFs* related to x_T with $x_T^2 = -x_\perp^2 > 0$,

$$\mathcal{B}_{q/P}(z, x_T^2, \mu) = \frac{1}{2\pi} \int dt e^{-izt\bar{n} \cdot P} \langle P | \bar{\chi}_c(t\bar{n} + x_\perp) \frac{\not{t}}{2} \chi_c(0) | P \rangle. \tag{2.49}$$

Using the transverse PDF \mathcal{B} , we can express the cross section as

$$\begin{aligned}
\frac{d\sigma}{dM^2 dq_T^2 dy} &= \frac{4\pi\alpha^2}{3N_c M^2 s} |C_V(-M^2, \mu)|^2 \frac{1}{4\pi} \int d^2 x_\perp e^{-iq_\perp \cdot x_\perp} \\
&\times \sum_q e_q^2 [\mathcal{B}_{q/P_1}(\xi_1, x_T^2, \mu) \mathcal{B}_{\bar{q}/P_2}(\xi_2, x_T^2, \mu) + (q \leftrightarrow \bar{q})] + \mathcal{O}\left(\frac{q_T^2}{M^2}\right),
\end{aligned} \tag{2.50}$$

where we define

$$\xi_1 = \sqrt{\tau} e^y, \quad \xi_2 = \sqrt{\tau} e^{-y}, \quad \text{with} \quad \tau = \frac{M^2}{s}, \tag{2.51}$$

and the $d^4 x$ integration has been rewritten in terms of light cone coordinates:

$$\int d^4 x = \frac{1}{2} \int_{-\infty}^{\infty} dx_+ \int_{-\infty}^{\infty} dx_- \int d^2 x_\perp. \tag{2.52}$$

The integration over x_+ and x_- fixes the momentum fractions ξ_1, ξ_2 . We have also used the identities $d^4q \theta(q^0) \delta(q^2 - M^2) = \frac{1}{2} d^2q_\perp dy = \frac{\pi}{2} d^2q_T dy$. The formula above seems to achieve the desired factorization of the scales M^2 and $q_T^2 \sim x_T^{-2}$.

2.3.5 The Collinear Anomaly

The factorization is not fully accomplished yet. Looking at Formula (2.50), we see that the Wilson coefficient C_V depends on the scale $M^2 \sim q^2$. The *renormalisation group* (RG) equation for C_V that will be solved in Section 3.1 includes a term $\mathcal{C} \ln(q^2/\mu^2)$, where \mathcal{C} is a factor,

$$\frac{d}{d \ln \mu} C_V \sim \left[\mathcal{C} \ln \left(\frac{q^2}{\mu^2} \right) + \dots \right] C_V. \quad (2.53)$$

But we demand that the physical cross section is independent of the scale μ . This implies that the product of beam functions depends on the same term with opposite sign,

$$\frac{d}{d \ln \mu} \sigma = 0 \quad \rightarrow \quad \frac{d}{d \ln \mu} [\mathcal{B}\mathcal{B}] \sim - \left(\mathcal{C} \ln \left(\frac{q^2}{\mu^2} \right) + \dots \right) [\mathcal{B}\mathcal{B}]. \quad (2.54)$$

In other words, the beam functions contain a hidden dependence on the large scale $q^2 \sim M^2$. This effect is called an *anomaly* because it is a quantum effect not present at the classical level. In [1] it was shown that the product can be refactorized as follows:

$$[\mathcal{B}_{q/P_1}(\xi_1, x_T^2, \mu) \mathcal{B}_{\bar{q}/P_2}(\xi_2, x_T^2, \mu)] = \left(\frac{x_T^2 q^2}{b_0^2} \right)^{-F_{q\bar{q}}(x_T^2, \mu)} B_{q/P_1}(\xi_1, x_T^2, \mu) B_{\bar{q}/P_2}(\xi_2, x_T^2, \mu), \quad (2.55)$$

with $b_0 = 2^{-\gamma_E}$. The functions B_{i/P_j} are independent of the hard momentum transfer q^2 , which is now a power with exponent $F_{q\bar{q}}$. The corresponding calculations are traced in Section 3.2. Using this refactorization we are finally left with the formula (2.1) given at the beginning of this chapter, in which the disparate scales M^2 and q_T^2 are completely separated,

$$\begin{aligned} \frac{d\sigma}{dM^2 dq_T^2 dy} &= \frac{4\pi\alpha^2}{3N_c M^2 s} |C_V(-M^2, \mu)|^2 \frac{1}{4\pi} \int d^2x_\perp e^{-iq_\perp \cdot x_\perp} \left(\frac{x_T^2 M^2}{b_0^2} \right)^{-F_{q\bar{q}}(x_T^2, \mu)} \\ &\quad \times \sum_q e_q^2 [B_{q/P_1}(\xi_1, x_T^2, \mu) B_{\bar{q}/P_2}(\xi_2, x_T^2, \mu) + (q \leftrightarrow \bar{q})] + \mathcal{O} \left(\frac{q_T^2}{M^2} \right). \end{aligned} \quad (2.56)$$

The beam functions B have been shown in [4] to obey an operator-product expansion of the form

$$B_{i/P}(\xi, x_T^2, \mu) = \sum_j \int_\xi^1 \frac{dz}{z} I_{i \leftarrow j}(z, x_T^2, \mu) \phi_{j/P}(\xi/z, \mu), \quad (2.57)$$

where the $I_{i \leftarrow j}$ are called *kernel functions*. Both B and I are specified in Section 3.2.

Chapter 3

Calculation of the Cross Section

Nothing in life is to be feared, it is only to be understood. Now is the time to understand more, so that we may fear less.

Marie Sklodowska Curie, 1867-1934

Now that the factorization formula (2.56) has been derived, we explicitly calculate the Wilson coefficient C_V to include the NLO-correction for the strong interaction and the beam functions B encoding radiation. The numerical implementation of all components of the formula will be explained in Chapter 5. At this point we slightly adjust the wording: Instead of the large scale M used in the previous chapter, we speak of the *hard scale* Q . Both quantities $Q^2 = M^2$ correspond to the mass squared of the dilepton final state. When we speak of the *hard function*, we mean the Wilson coefficient C_V that encodes virtual corrections from the strong interaction of a quark and an anti-quark.

3.1 The Hard Function to One Loop and Resummation of Large Logarithms

We write the hard function as a series in the strong coupling constant α_s ,

$$\mathcal{H}_{ij}(\hat{p}_1, \hat{p}_2, q, \mu) = 1 + \frac{\alpha_s(\mu)}{4\pi} \mathcal{H}_{ij}^{(1)}(\hat{p}_1, \hat{p}_2, q, \mu) + \mathcal{O}(\alpha_s^2), \quad (3.1)$$

where $\hat{p}_i = P_i \xi_i$ is the momentum fraction going into the hard interaction after possible emissions. The square of the Wilson coefficient $|C_V(-M^2, \mu)|^2$ in the factorization

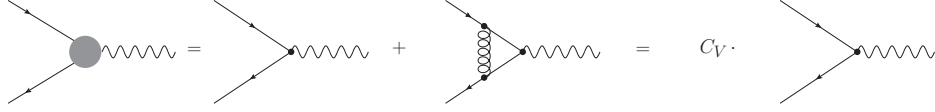


FIGURE 3.1: The hard function at NLO is obtained by summing the tree-level and the virtual 1-loop contributions. This is identical to multiplying the matching coefficient C_V with the tree-level result.

formula (2.56) corresponds to the first two terms of the series, where the second term denotes the one-loop virtual correction. The matching procedure is illustrated in Fig. 3.1. The Wilson coefficient calculated in dimensional regularization for the photon production process reads

$$C_V^{\text{bare}}(\epsilon, Q^2) = 1 + \frac{\alpha_s^0}{4\pi} C_F \left(-\frac{2}{\epsilon^2} - \frac{3}{\epsilon} - 8 + \frac{\pi^2}{6} + \mathcal{O}(\epsilon) \right) \left(\frac{e^{\gamma_E} Q^2}{4\pi} \right)^{-\epsilon} + \mathcal{O}(\alpha_s^2), \quad (3.2)$$

where $\alpha_s^0 = g_s^2/4\pi$ is the bare coupling constant and γ_E the Euler-Mascheroni constant. We now renormalize the coefficient in the $\overline{\text{MS}}$ ¹ scheme, introducing a scale μ and expressing the bare coupling α_s^0 in terms of $\alpha_s(\mu)$. Using the relation $Z_\alpha \alpha_s(\mu) \mu^{2\epsilon} = e^{-\epsilon\gamma_E} (4\pi)^\epsilon \alpha_s^0$ with $Z_\alpha = 1 + \mathcal{O}(\alpha_s)$, we obtain

$$C_V^{\text{bare}}(\epsilon, Q^2) = 1 + \frac{\alpha_s(\mu)}{4\pi} C_F \left(-\frac{2}{\epsilon^2} - \frac{3}{\epsilon} - 8 + \frac{\pi^2}{6} + \mathcal{O}(\epsilon) \right) \left(\frac{Q^2}{\mu^2} \right)^{-\epsilon} + \mathcal{O}(\alpha_s^2). \quad (3.3)$$

The divergences are absorbed into a multiplicative factor Z ,

$$Z(\epsilon, Q^2, \mu) = 1 + \frac{\alpha_s(\mu)}{4\pi} C_F \left(-\frac{2}{\epsilon^2} - \frac{3}{\epsilon} + \frac{2}{\epsilon} \ln \frac{Q^2}{\mu^2} \right) + \mathcal{O}(\alpha_s^2). \quad (3.4)$$

One can check that the equation

$$C_V(Q^2, \mu) = \lim_{\epsilon \rightarrow 0} Z^{-1}(\epsilon, Q^2, \mu) C_V^{\text{bare}}(\epsilon, Q^2) \quad (3.5)$$

holds, with the renormalized Wilson coefficient C_V at order α_s given by

$$C_V(Q^2, \mu) = 1 + \frac{\alpha_s(\mu)}{4\pi} C_F \left(-\ln^2 \frac{Q^2}{\mu^2} + 3 \ln \frac{Q^2}{\mu^2} + \frac{\pi^2}{6} - 8 \right) + \mathcal{O}(\alpha_s^2). \quad (3.6)$$

¹Modified minimal subtraction ($\overline{\text{MS}}$) is a scheme for choosing the finite parts of the counterterms in the process of renormalization.

We compute the square of C_V to find

$$\mathcal{H}_{q\bar{q}}^{(1)} = \underbrace{-2C_F \ln^2 \frac{Q^2}{\mu^2}}_{L^2} + \underbrace{6C_F \ln \frac{Q^2}{\mu^2}}_{L^1} + \underbrace{C_F \left(\frac{2\pi^2}{6} - 16 \right)}_{L^0}. \quad (3.7)$$

Note that, had we evaluated $C_V(-Q^2, \mu)$, as it appears in the factorization formula, instead of $C_V(Q^2, \mu)$, we would have obtained $7\pi^2/3$ instead of $2\pi^2/6$, because $\ln(-a) = \ln(a) + i\pi$ for $a > 0$. With $L \equiv \ln(Q^2/\mu^2)$ scaling as α_s^{-1} , $\mathcal{H}^{(1)}$ contains leading logarithmic (LL) terms with $\alpha_s L^2 \sim \mathcal{O}(1/\alpha_s)$, next-to leading logarithmic (NLL) terms with $\alpha_s L \sim \mathcal{O}(1)$ and next-to-next-to leading logarithmic (NNLL) terms with $\alpha_s L^0 \sim \mathcal{O}(\alpha_s)$. We observe that (3.7) involves large logarithms for $\mu^2 \ll Q^2$, while the beam functions involve large logarithms for $\mu^2 \gg q_T^2$, as we shall see in the next section. This dilemma can be remedied by solving the *renormalization group equation* for C_V . The following equation holds to all orders in α_s ,

$$\frac{d}{d \ln \mu} C_V(Q^2, \mu) = \left[C_F \gamma_{\text{cusp}}(\alpha_s) \ln \frac{Q^2}{\mu^2} + \gamma_V(\alpha_s) \right] C_V(Q^2, \mu), \quad (3.8)$$

where the functions

$$\gamma_{\text{cusp}}(\alpha_s) = 4 \frac{\alpha_s(\mu)}{4\pi} + \mathcal{O}(\alpha_s^2), \quad \gamma_V(\alpha_s) = -6C_F \frac{\alpha_s(\mu)}{4\pi} + \mathcal{O}(\alpha_s^2) \quad (3.9)$$

are anomalous dimensions. One obtains the solution

$$C_V(Q^2, \mu) = \exp \left\{ \int_{\mu_h}^{\mu} \left[C_F \gamma_{\text{cusp}}(\alpha_s) \ln \frac{Q^2}{\mu'^2} + \gamma_V(\alpha_s) \right] d \ln \mu' \right\} C_V(Q^2, \mu_h). \quad (3.10)$$

It is convenient to write the solution in terms of an evolution factor U ,

$$C_V(Q^2, \mu) = U(\mu_h, \mu) C_V(Q^2, \mu_h). \quad (3.11)$$

This relation allows us to evaluate the hard function at a high scale $\mu_h \sim Q$ and then to evolve the result down to a low scale $\mu \sim q_T$ where the beam functions are evaluated. The large logarithms are thus absorbed into an exponent while the Wilson coefficients are well-behaved. This procedure is referred to as *resummation of large logarithms to all orders in α_s* . The explicit formula for U is given in the Appendix, see B.1.

3.2 The Fourier Integral with Beam Functions to $\mathcal{O}(\epsilon)$

3.2.1 Factoring Out Dependencies on the Hard Scale and Double Logarithms

In perturbation theory, the beam functions B in (2.56) are polynomials in a logarithmic quantity L_\perp ,

$$L_\perp \equiv \ln \left(\frac{x_T^2 \mu^2}{b_0^2} \right), \quad (3.12)$$

that depends on the transverse displacement x_T and a scale μ , while $b_0 = 2e^{-\gamma_E}$ is a constant. The transverse PDFs \mathcal{B} that first appeared in (2.50) contain a dependence on the square of the hard momentum transfer q^2 . As has been shown in (2.55) this dependence can be factored out, leaving us with the beam functions B . We will see in the following that for a valid expansion we will need to factor out yet another quantity, namely the double logarithmic dependence of the beam functions B on L_\perp . The beam functions after both refactorizations will be denoted as \bar{B} . The corresponding notation for the kernel functions is \mathcal{I} , I and \bar{I} .

We start with the following relation from [4],

$$\begin{aligned} [\mathcal{B}_{q/q}(z_1, x_T^2) \mathcal{B}_{\bar{q}/\bar{q}}(z_2, x_T^2)]_{q^2} &= \delta(1-z_1)\delta(1-z_2) \\ &\quad - \frac{C_F \alpha_s}{4\pi} \left\{ \delta(1-z_1)\delta(1-z_2) \left(4L_\perp \ln \left(\frac{q^2}{\mu^2} \right) + 2L_\perp^2 + \frac{\pi^2}{3} \right) \right. \\ &\quad \left. + \left[2\delta(1-z_2) \left(L_\perp \frac{1+z_2^2}{[1-z_2]_+} - (1-z_2) \right) + (z_1 \leftrightarrow z_2) \right] \right\}. \end{aligned} \quad (3.13)$$

Note that compared to (2.55) the hadronic state P_1 in \mathcal{B}_{q/P_1} has been replaced by a quark q in $\mathcal{B}_{q/q}$. The same holds for \mathcal{B}_{q/P_2} and $\mathcal{B}_{\bar{q}/\bar{q}}$. The subscript q^2 indicates the hidden dependence on q^2 that can be seen explicitly in the second line. In the last line, $[1-z_2]_+$ indicates a *plus distribution*. Plus distributions are discussed in A.5. The q^2 dependent term can be expressed as

$$\ln \left(\frac{q^2}{\mu^2} \right) = \ln \left(\frac{M^2 x_T^2}{b_0^2} \right) - L_\perp, \quad (3.14)$$

and a comparison of the relevant terms of (2.55) and (3.13) yields

$$\left(\frac{x_T^2 q^2}{b_0^2}\right)^{-F_{q\bar{q}}(x_T^2, \mu)} = e^{-F_{q\bar{q}} \ln\left(\frac{x_T^2 q^2}{b_0^2}\right)} \sim 1 - 4 \frac{C_F \alpha_s}{4\pi} L_\perp \ln\left(\frac{M^2 x_T^2}{b_0^2}\right). \quad (3.15)$$

Expanding the left-hand side in α_s , we read off

$$F_{q\bar{q}}(x_T^2, \mu) = C_F \gamma_{\text{cusp}} L_\perp + \mathcal{O}(\alpha_s^2). \quad (3.16)$$

The relationship between the partonic beam functions $\mathcal{B}_{i/j}$ and the kernel functions $\mathcal{I}_{i \leftarrow j}$ can be seen as follows,

$$\begin{aligned} B_{i/j}(\xi, x_T^2, \mu) &= \sum_k \int_\xi^1 \frac{dz}{z} I_{i \leftarrow k}(z, x_T^2, \mu) \phi_{k/j}(\xi/z, \mu) \\ &= \sum_k \int_\xi^1 \frac{dz}{z} I_{i \leftarrow j}(z, x_T^2, \mu) \delta(1 - \xi/z) \delta_{kj} \\ &= I_{i \leftarrow j}(\xi, x_T^2, \mu), \end{aligned} \quad (3.17)$$

where we have used that the partonic PDFs are $\phi_{k/j}(x) = \delta(1 - x) \delta_{kj}$. Using this relationship we can restate equation (2.55) as

$$[\mathcal{I}_{q \leftarrow i}(z_1, x_T^2, \mu) \mathcal{I}_{\bar{q} \leftarrow j}(z_2, x_T^2, \mu)] = \left(\frac{x_T^2 q^2}{b_0^2}\right)^{-F_{q\bar{q}}(x_T^2, \mu)} I_{q \leftarrow i}(z_1, x_T^2, \mu) I_{\bar{q} \leftarrow j}(z_2, x_T^2, \mu). \quad (3.18)$$

Comparing (3.18) with (3.13), one can find the explicit expression for the kernel functions I at order α_s [1],

$$I_{q \leftarrow q}(z, L_\perp, \alpha_s) = \delta(1 - z) \left[1 + \frac{C_F \alpha_s}{4\pi} \left(L_\perp^2 - \frac{\pi^2}{6} \right) \right] - \frac{C_F \alpha_s}{2\pi} \left[L_\perp \frac{1 + z^2}{[1 - z]_+} - (1 - z) \right]. \quad (3.19)$$

Here we observe the double logarithmic dependence of the kernel functions I on L_\perp . For not too small q_T , $\frac{x_T^2 \mu^2}{b_0^2} \sim 1$ and L_\perp is a small logarithm. So the kernel functions can be readily evaluated. We factor out this dependence by rewriting [2]

$$I_{q \leftarrow i}(z, L_\perp, \alpha_s) \equiv e^{h_i(L_\perp, \alpha_s)} \bar{I}_{q \leftarrow i}(z, L_\perp, \alpha_s). \quad (3.20)$$

The double-logarithmic exponent $h_i(L_\perp, \alpha_s)$ is defined as the solution of the RG equation

$$\frac{d}{d \ln \mu} h_i(L_\perp, \alpha_s) = C_i \gamma_{\text{cusp}} L_\perp - 2\gamma^i(\alpha_s) \quad (3.21)$$

with boundary condition $h_i(0, \alpha_s) = 0$. For quark-induced processes $C_i = C_F$, while we have $C_i = C_A$ in the gluon case. We arrange the prefactors into a single exponent,

$$e^{g_i(\eta_i, L_\perp, \alpha_s)} = \left(\frac{x_T^2 Q^2}{b_0^2} \right)^{-F_{ij}(L_\perp, \alpha_s)} e^{h_i(L_\perp, \alpha_s)} e^{h_j(L_\perp, \alpha_s)}. \quad (3.22)$$

The exponent $g_F(\eta_F, L_\perp, \alpha_s)$ for the quark case is listed in the Appendix (see B.2). We have introduced the variable η_i that will be elucidated in the next section,

$$\eta_i \equiv \eta_i(Q^2, \mu) = \frac{C_i \alpha_s(\mu)}{\pi} \ln \frac{Q^2}{\mu^2} \sim 1. \quad (3.23)$$

We adjust the factorization formula to the modifications found so far:

$$\begin{aligned} \frac{d\sigma}{dM^2 dq_T^2 dy} &= \frac{4\pi\alpha^2}{3N_c M^2 s} |C_V(-M^2, \mu)|^2 \frac{1}{4\pi} \int d^2 x_\perp e^{-iq_\perp \cdot x_\perp} e^{g_F(\eta_F, L_\perp, \alpha_s)} \\ &\times \sum_q e_q^2 [\bar{B}_i(\xi_1, x_\perp, \mu) \bar{B}_j(\xi_1, x_\perp, \mu) + (q \leftrightarrow \bar{q})]. \end{aligned} \quad (3.24)$$

Since the integrand only depends on $x_T^2 = -x_\perp^2$, we rewrite $q_\perp \cdot x_\perp = -x_T q_T \cos \phi$ and integrate over the azimuthal angle ϕ , which yields

$$\int_{-\infty}^{\infty} d^2 x_\perp e^{-iq_\perp \cdot x_\perp} = 2\pi \int_0^{+\infty} dx_T x_T J_0(x_T q_T). \quad (3.25)$$

Due to the oscillatory nature of the Bessel function $J_0(x_T q_T)$, the numerical convergence is rather slow. It can be improved by using the identity $J_0(x_T q_T) = \frac{2}{\pi} \text{Im} K_0(-ix_T q_T)$ and then performing a Wick rotation $x_T \rightarrow ix_T$. Omitting the prefactors and listing only the Fourier part \mathcal{F} of the cross section, we have

$$\begin{aligned} \mathcal{F}_{ij}(Q, \mu, q_T, \xi_i, \xi_j) &= \frac{1}{4\pi} \int d^2 x_\perp e^{-iq_\perp \cdot x_\perp} e^{g_F(\eta, L_\perp, \alpha_s)} \bar{B}_i(\xi_1, x_\perp, \mu) \bar{B}_j(\xi_1, x_\perp, \mu) \\ &= -\frac{1}{\pi} \text{Im} \int_0^{+\infty} dx_T x_T K_0(x_T q_T) e^{g_F(\eta, L_\perp, \alpha_s)} \bar{B}_i(\xi_1, x_\perp, \mu) \bar{B}_j(\xi_1, x_\perp, \mu). \end{aligned} \quad (3.26)$$

3.2.2 Scale Setting and Modified Power Counting

At this point, let us pause briefly, recapitulate our endeavour, review what we have already achieved and look ahead what remains to be done. Using an effective theory and a small expansion parameter $\lambda = q_T/M$, we have derived a factorization theorem (2.56) for Drell-Yan production at small transverse momentum $q_T \ll M$. What is the lower bound for the validity of the factorization formula regarding q_T ? One would expect that we would need to impose $\mu \gg \Lambda_{\text{QCD}}$, the location of the *Landau pole*², in order for perturbation theory to remain valid. However, we shall shortly introduce a scale q_* and show that the cross section can be calculated for arbitrarily small values of q_T , up to corrections controlled by Λ_{QCD}/q_* . We distinguish three regions of transverse momentum which require different treatment. For large $q_T \gtrsim 40\text{GeV}$, fixed order perturbative calculation is adequate, and there is no need for resummation as no large logarithms are present. In an intermediate region, large logarithms appear that we resum. In the region of very small $q_T \lesssim q_*$, the power counting must be modified.

We now need to set the factorization scale μ . For a reliable evaluation of the factorization formula, the quantity L_\perp (3.12) entering the Fourier integral via the beam functions \bar{B} and the exponent g_F should be a small quantity. Assuming that q_T and x_T are conjugate variables with $q_T \cdot x_T \sim 1$, the choice $\mu \sim q_T$ seems reasonable. A detailed study of the region of very small q_T in [2] leads to an associated scale q^* , given by the value of μ at which η (3.23) becomes equal to one,

$$q_* = Q \exp\left(-\frac{\pi}{2C_i \alpha_s(q_*)}\right). \quad (3.27)$$

In our numerical work, we therefore use $\mu = q_T + q_*$ as the default choice for the factorization scale. For Z production $q^* \approx 1.88\text{GeV}$. Note that since we set the scale independently of the integration variable, we do not hit the Landau pole. A consequence of the appearance of the dynamical scale q^* is that the logarithm L_\perp , which counts as an $\mathcal{O}(1)$ quantity for $\mu \sim q_T$, now scales as $L_\perp \sim \frac{1}{\sqrt{\alpha_s}}$ for $q_T \rightarrow 0$. To keep track of the powers we introduce a parameter ϵ with $\alpha_s \sim \epsilon$ and $L_\perp \sim \epsilon^{-1/2}$. Consequently, for our order α_s calculation we consider terms of order $\epsilon^{-1/2}$, ϵ^0 , $\epsilon^{1/2}$ and ϵ . This modified power counting has been considered for the exponent g_F (see B.2).

²L. D. Landau (1908-1968) was a Soviet physicist. The Landau pole is the scale where perturbation theory breaks down, because the loop corrections become as large as the leading order. For $\mu \sim \Lambda_{\text{QCD}}$, $\alpha_s(\mu) \rightarrow \infty$.

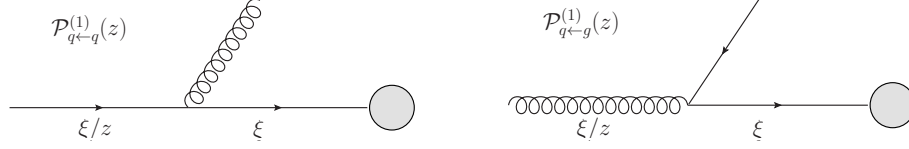


FIGURE 3.2: Left: Gluon emission. Right: Quark emission.

3.2.3 The Beam Functions as an Expansion in L_\perp

As depicted in Figure 2.1, the transverse-position dependent beam function \bar{B}_i factorizes into a perturbative kernel $\bar{I}_{i\leftarrow j}$ describing the soft and collinear emissions at low transverse momentum and a PDF ϕ_j ,

$$\bar{B}_i(\xi, x_\perp, \mu) = \sum_j \int_\xi^1 \frac{dz}{z} \bar{I}_{i\leftarrow j}(z, x_\perp, \mu) \phi_j(\xi/z, \mu). \quad (3.28)$$

For NNLL resummation³, we need the one-loop result for $\bar{I}_{i\leftarrow j}$ which takes the form

$$\bar{I}_{i\leftarrow j}(z) = \delta(1-z) \delta_{ij} - a_s \left[\mathcal{P}_{i\leftarrow j}^{(1)}(z) \frac{L_\perp}{2} - \mathcal{R}_{i\leftarrow j}(z) \right] + \mathcal{O}(a_s^2). \quad (3.29)$$

Here we have introduced the abbreviation $a_s = \alpha_s(\mu)/4\pi$. The first term of the expansion takes care of the case where no emission takes place, $z = 1$, and the beam function corresponds to the PDF. The logarithmic piece is proportional to the Dokshitzer-Gribov-Lipatov-Altarelli-Parisi (DGLAP) splitting functions $\mathcal{P}_{i\leftarrow j}^{(1)}$ at one loop. The two relevant terms for $\mathcal{P}_{i\leftarrow j}^{(1)}$ are $\mathcal{P}_{q\leftarrow q}^{(1)}$ and $\mathcal{P}_{q\leftarrow g}^{(1)}$, see Fig. 3.2. To achieve uniform accuracy over the entire low q_T region, we take into account the modified power counting and also include the leading logarithmic piece of the two-loop beam functions

$$\Delta \bar{I}_{i\leftarrow j}(z) = a_s^2 \left(\mathcal{D}_{i\leftarrow j}(z) - 2\beta_0 \mathcal{P}_{i\leftarrow j}^{(1)}(z) \right) \frac{L_\perp^2}{8}, \quad (3.30)$$

where

$$\mathcal{D}_{i\leftarrow j}(z) = \sum_k \mathcal{D}_{i\leftarrow k\leftarrow j}(z) = \sum_{k=q,\bar{q},g} \int_z^1 \frac{du}{u} \mathcal{P}_{i\leftarrow k}^{(1)}(u) \mathcal{P}_{k\leftarrow j}^{(1)}(z/u). \quad (3.31)$$

Two of the contributions to $\mathcal{D}_{i\leftarrow k\leftarrow j}$ for quark-induced hard scattering are depicted in Figure 3.3. The diagram to the right shows that the quark flavor before and after radiation can differ in the two-loop terms. The DGLAP splitting functions $\mathcal{P}_{i\leftarrow j}^{(1)}$, the

³The terms LL, NLL and NNLL are explained in the text below Formula (3.7).

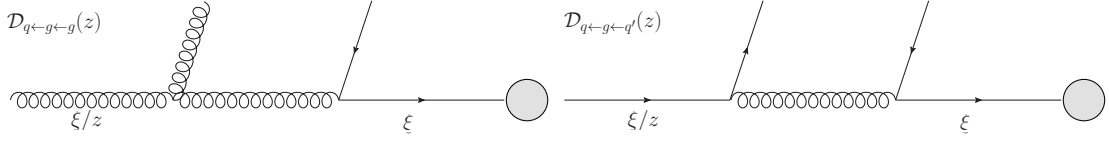


FIGURE 3.3: Left: Quark and gluon emission. Right: Double quark emission.

remainder functions $\mathcal{R}_{i\leftarrow j}$ and the two-loop functions $\mathcal{D}_{i\leftarrow j}$ are listed in Appendix B.3, and sample computations for $\mathcal{D}_{i\leftarrow j}$ is performed in A.5.

The complete beam function at NNLL accuracy is thus a second order polynomial in the logarithm L_\perp ,

$$\begin{aligned}
 \bar{B}_i(\xi, x_\perp, \mu) &= \sum_j \int_\xi^1 \frac{dz}{z} \left[\delta(1-z) \delta_{ij} - a_s \mathcal{P}_{i\leftarrow j}^{(1)}(z) \frac{L_\perp}{2} + a_s \mathcal{R}_{i\leftarrow j}(z) \right. \\
 &\quad \left. + a_s^2 \left(\mathcal{D}_{i\leftarrow j}(z) - 2\beta_0 \mathcal{P}_{i\leftarrow j}^{(1)}(z) \right) \frac{L_\perp^2}{8} \right] \phi_j(\xi/z, \mu) \\
 &\equiv B_i^{(0)}(\xi, \mu) + a_s B_i^{(1)}(\xi, \mu) - a_s \frac{L_\perp}{2} B_i^{(2)}(\xi, \mu) \\
 &\quad + a_s^2 L_\perp^2 \left(-\frac{\beta_0}{4} B_i^{(2)}(\xi, \mu) + \frac{1}{8} B_i^{(3)}(\xi, \mu) \right), \tag{3.32}
 \end{aligned}$$

and the coefficients $B_i^{(m)}(\xi, \mu)$ are functions of the momentum fraction ξ and the factorization scale μ . With the coefficients $B_i^{(m)}(\xi, \mu)$ at hand, the Fourier integral reduces to a set of integrals involving the n -th power of a logarithm

$$\mathcal{M}_n(Q, \mu, q_T) = -\frac{1}{\pi} \text{Im} \int_0^{+\infty} dx_T x_T K_0(x_T q_T) e^{g_F(\eta_F, L_\perp, a_s)} L_\perp^n. \tag{3.33}$$

Expressed in terms of the integrals \mathcal{M}_n and coefficients $B_i^{(m)}$, the final form of the Fourier-integral, as implemented in our code, is

$$\begin{aligned}
 \mathcal{F}_{ij}(Q, \mu, q_T, \xi_i, \xi_j) &= \frac{1}{4\pi} \int d^2 x_\perp e^{-iq_\perp \cdot x_\perp} e^{g_F(\eta_F, L_\perp, a_s)} \bar{B}_i(\xi_1, x_\perp, \mu) \bar{B}_j(\xi_2, x_\perp, \mu) \\
 &= \mathcal{M}_0(Q, \mu, q_T) \left[B_i^{(0)}(\xi_1, \mu) B_j^{(0)}(\xi_2, \mu) + a_s B_i^{(0)}(\xi_1, \mu) B_j^{(1)}(\xi_2, \mu) + a_s B_i^{(1)}(\xi_1, \mu) B_j^{(0)}(\xi_2, \mu) \right] \\
 &\quad - \frac{a_s}{2} \mathcal{M}_1(Q, \mu, q_T) \left[B_i^{(0)}(\xi_1, \mu) B_j^{(2)}(\xi_2, \mu) + B_i^{(2)}(\xi_1, \mu) B_j^{(0)}(\xi_2, \mu) \right] \\
 &\quad + \frac{a_s^2}{4} \mathcal{M}_2(Q, \mu, q_T) \left[-\beta_0 B_i^{(0)}(\xi_1, \mu) B_j^{(2)}(\xi_2, \mu) - \beta_0 B_i^{(2)}(\xi_1, \mu) B_j^{(0)}(\xi_2, \mu) \right. \\
 &\quad \left. + \frac{B_i^{(0)}(\xi_1, \mu) B_j^{(3)}(\xi_2, \mu)}{2} + \frac{B_i^{(3)}(\xi_1, \mu) B_j^{(0)}(\xi_2, \mu)}{2} + B_i^{(2)}(\xi_1, \mu) B_j^{(2)}(\xi_2, \mu) \right]. \tag{3.34}
 \end{aligned}$$

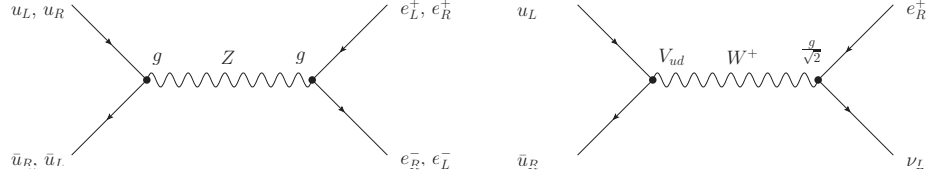


FIGURE 3.4: Left: Electroweak interaction mediated by the Z . Right: Electroweak interaction mediated by the W^+ .

3.3 The Transition from Electromagnetic to Electroweak Interactions

Our considerations so far are related to an electromagnetic process mediated by a photon, our efforts however are aimed at treating electroweak processes including Z and W boson production by quark-antiquark annihilation. Here we must take into account the chirality of the fermions: W bosons couple to left fermions and right antifermions. Z bosons and photons couple to both components. In experiment, coupling could only be verified for left neutrinos and right antineutrinos. The quarks coupling to W bosons are of different flavor, so quark mixing must be kept in mind.

A detailed discussion of electroweak interactions is beyond the scope of this work. Instead, we will briefly discuss the sample interactions depicted in Fig. 3.4. The interaction $u\bar{u} \rightarrow Z \rightarrow e^+e^-$ is realized in four variants respecting conservation of weak hypercharge, one of them being $u_L\bar{u}_R \rightarrow Z \rightarrow e_L^+e_R^-$. Each fermion couples to the Z with a specific factor times the coupling constant g . To obtain the amplitude for this process, all possibilities must be summed. The process $u\bar{d} \rightarrow W^+ \rightarrow e^+\nu$ has been observed in the version $u_L\bar{d}_R \rightarrow W^+ \rightarrow e_R^+\nu_L$ as shown in Fig. 3.4. The coupling of fermions to the W is $g/\sqrt{2}$, and the factor V_{ud} takes care of the quark mixing involved with this interaction. The coupling constant g is related to the electromagnetic coupling α by $g^2 \sin^2 \theta_W = 4\pi\alpha$, where θ_W is the electroweak mixing angle named after S. Weinberg⁴. The angle θ_W is the only free parameter of the electroweak interaction, assuming the electromagnetic coupling α is already known, and it needs to be determined by experiment.

The result (2.56) can hence be generalized to W and Z production (without subsequent decay) as follows. To obtain the double differential cross section $d^2\sigma/dq_T^2 dy$ we change the prefactor according to

$$\frac{4\pi\alpha^2}{3N_c M^2 s} \rightarrow \frac{4\pi^2\alpha}{N_c s} \quad (3.35)$$

⁴Steven Weinberg (1933) is a US-American physicist of Austrian origin.

and insert the proper charge factors. For the Z boson we replace

$$\sum_q e_q^2 \rightarrow \sum_q \frac{|g_L^q|^2 + |g_R^q|^2}{2} = \sum_q \frac{(1 - 2|e_q| \sin^2 \theta_W)^2 + 4e_q^2 \sin^4 \theta_W}{8 \sin^2 \theta_W \cos^2 \theta_W}. \quad (3.36)$$

For the W we replace the sum over flavors q by a double sum over individual quark and anti-quark flavors q, q' . The relevant coupling for a W^+ boson produced in the annihilation of an anti-down and an up quark is

$$\sum_q e_q^2 \rightarrow \sum_{q,q'} \frac{|g_L^{q,q'}|^2}{2} = \sum_{q,q'} \frac{|V_{q,q'}|^2}{4 \sin^2 \theta_W}, \quad (3.37)$$

where $V_{q,q'}$ are elements of the Cabibbo–Kobaiashi–Maskawa (CKM) quark mixing matrix.

Chapter 4

Highlights of the Calculations

The more I study, the more insatiable
do I feel my genius for it to be.

Ada Lovelace, 1815-1852

4.1 Improving the Measurement: The Observable ϕ^*

The observable ϕ^* has been developed based on the fact that collider detectors generally have far better angular resolution than calorimeter (energy) or track (momentum) resolution. In the following, I sketch the history of the ϕ^* -observable.

In [17], the authors discuss the ingredients of the q_T -measurement in experiment. In a Drell-Yan process, the q_T -measurement depends on the resolution of the transverse momentum p_T of the leptons as well as on the overall event selection efficiency. They propose an observable that is sensitive to q_T , but less sensitive to these experimental systematics. They decompose the $\vec{q}_T = \vec{p}_T^{(1)} + \vec{p}_T^{(2)}$ into two orthogonal components: a_T transverse and a_L parallel to the di-lepton thrust-axis \hat{t} , see Fig. 4.1, where

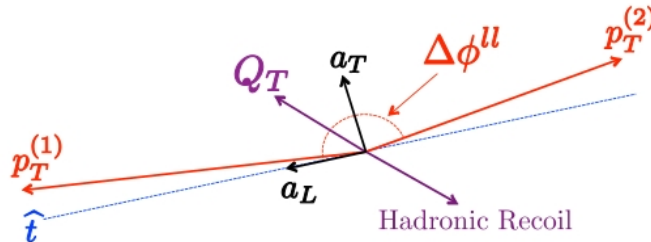


FIGURE 4.1: Construction of the observable a_T . Figure from [17].

$$\hat{t} = \frac{\vec{p}_T^{(1)} - \vec{p}_T^{(2)}}{|\vec{p}_T^{(1)} - \vec{p}_T^{(2)}|}, \quad a_T = |\vec{q}_T \times \hat{t}|, \quad a_L = \vec{q}_T \cdot \hat{t}. \quad (4.1)$$

For events with opening angle of the leptons in the transverse plane $\Delta\phi^l < \pi/2$, corresponding to only approximately 1% of the cross section, this decomposition is not useful, and a_T is set equal to q_T . The sensitivity to lepton p_T mis-measurement and the dependence on event selection efficiency of the observables q_T , a_T and a_L are studied. The authors conclude that for low to moderate values of q_T , $q_T < 50$ GeV, a_T is significantly less prone to these experimental systematics than q_T .

A theoretical study of the novel variable a_T is carried out in [18]. The authors perform a resummation at NLL for the variable a_T and compare this result to the one stemming from the q_T distribution. They show that the calculations are nearly identical, and that the resulting leading order cross sections for a_T and $q_T/2$ coincide up to a constant term. The resummed results are then expanded to order α_s^2 and tested against fixed-order results at NLO-level using the program MCFM¹. The authors conclude that in the low a_T domain, the variable is useful for modelling partonic radiation and studying small- x broadening of transverse momentum distributions.

In [19], the variable $\phi^* \approx a_T/Q$ is introduced, where Q represents the dilepton invariant mass. It is defined as

$$\phi^* = \tan\left(\frac{\pi - \Delta\phi}{2}\right) \sin(\theta^*), \quad \text{with} \quad \cos(\theta^*) := \tanh\left(\frac{\Delta\eta}{2}\right), \quad (4.2)$$

where $\Delta\eta = \eta^- - \eta^+$ is the difference in pseudorapidity η ,

$$\eta = -\ln\left[\tan\left(\frac{\theta}{2}\right)\right], \quad (4.3)$$

of the decaying leptons and $\Delta\phi$ the opening angle of the leptons in the azimuthal plane. The angle between the momentum vector of the particle and the beam axis is denoted θ . In Fig. 4.2 the two factors forming ϕ^* are visualized. A variation of $\Delta\phi$ around its leading-order (also called *Born-level*²) value at $\Delta\phi = \pi$ shows that the first factor is zero at Born level and obtains its maximum for $\Delta\phi \rightarrow 0$. The second factor takes values in $[0, 1]$ and is maximal for $\Delta\eta = 0$. Intuitively, the observable ϕ^* is a measure of the deviation of the lepton opening angle $\Delta\phi$ from its value at Born level.

¹<http://mcfm.fnal.gov/>

²Max Born (1882-1970) was a german physicist.

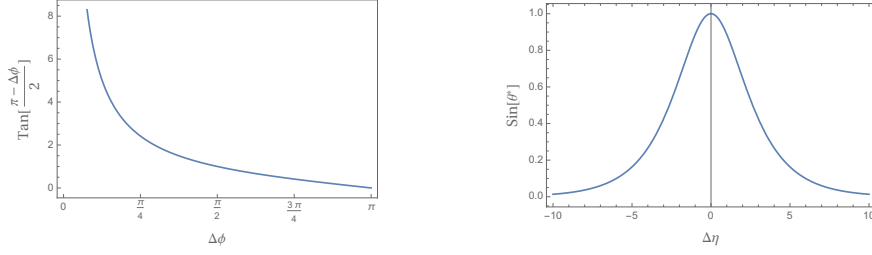


FIGURE 4.2: Left: If the leptons are back to back, $\Delta\phi = \pi$ and $\phi^* = 0$. Right: The maximum of ϕ^* is obtained for $\Delta\eta = 0$.

The observable ϕ^* is determined exclusively from the measured lepton directions. The authors perform detailed studies of different variables, for example a_T and Q_T/Q , regarding physics sensitivity (dependence of the variable on Q), experimental resolution and immunity to experimental systematic uncertainties. They show that in the region of low q_T , the variable ϕ^* is superior to other variables.

An analytical prediction for the ϕ^* variable is presented in [20]. In this paper, the resummation is performed at next-to-next-to-leading order, and the result is matched to NLO fixed-order results. Cuts on the final state leptons, as they are used in experiment, are incorporated into the calculation. A comparison to experimental data is carried out in [21]. The computations are performed at the appropriate renormalisation, factorisation and resummation scales, which are then varied in order to assess the uncertainty of the results. The authors report excellent agreement with experimental data stemming from the $D\bar{0}$ collaboration over a large range of ϕ^* in all rapidity bins. Finally, in [22], an equivalent study is carried out using LHC data. The resummed predictions are obtained using a reweighting procedure similar to ours.

Fig. 4.3 shows a density plot of the cross section in q_T and $\log_{10} \phi^*$ to illustrate the correlation among the two observables. For a given q_T , there is a maximum possible value for ϕ^* obtained when the two leptons are produced at $\Delta\eta = 0$. One finds that $\phi_{\max}^* = q_T/Q$ (for a derivation see A.7). The corresponding relation for $Q = M_Z$ is shown as a dashed red line, and the red area above the line is kinematically excluded. The largest cross section is found near the maximum possible value of ϕ^* which demonstrates the close correlation among the two observables.

4.2 A Step Towards More Realism: Considering Recoil Effects

The derivation of the factorization formula for the cross section in Chapter 2 was based on the small expansion parameter $\lambda = q_T/M$. Contributions of higher order in λ were

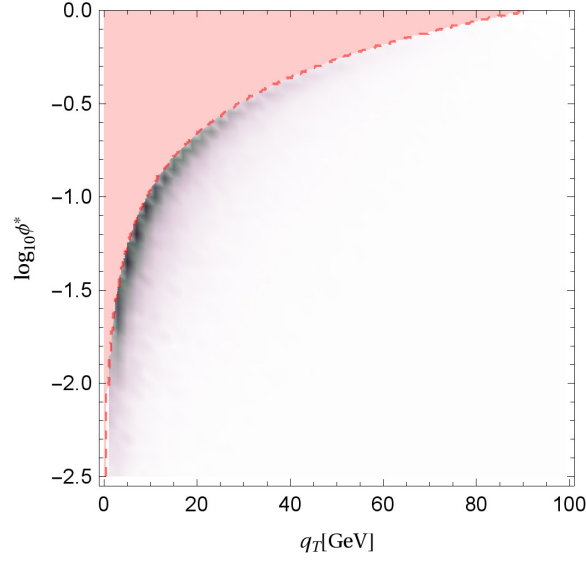


FIGURE 4.3: The double differential cross section in q_T and $\log_{10} \phi^*$. The dashed red line corresponds to $\phi^* = q_T/M_Z$, the maximum achievable value of ϕ^* for a given q_T . In the red region above the dashed line, the cross section vanishes. Dark areas in the density plot correspond to a large cross section. Most of the cross section arises from values of ϕ^* close to the kinematic boundary.

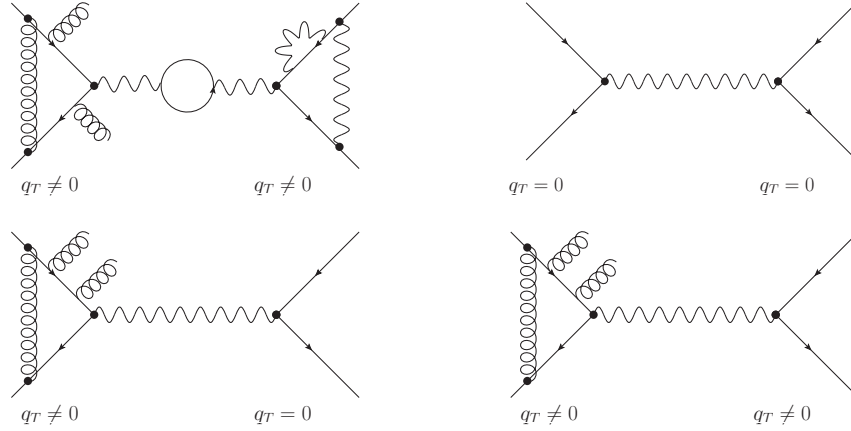


FIGURE 4.4: Upper left: In a physical process countless radiation processes take place, leading to equal and opposite transverse momenta in the initial hadronic and the final leptonic part. Upper right: In the process at tree level, no transverse momentum is present. Lower left: Neglecting recoil effects leads to a mismatch in the kinematics of the initial and the final state. Lower right: Boosting the tree-level event restores conservation of transverse momentum.

systematically expanded away. In particular, the small transverse momentum of the partons entering the hard scattering process was not taken into account. As a consequence, the partons obey tree-level kinematics in the factorization formula (2.56),

$$\xi_1 p_1 + \xi_2 p_2 = q. \quad (4.4)$$

This situation is depicted in the upper right of Fig. 4.4. Expanding away the small transverse momenta is appropriate for the computation of the QCD corrections associated with the large scale Q^2 as $q_T \ll Q$. It is useful because the hard part of the process is then given by the tree-level amplitude times correction factors, allowing us to generate this part using a tree-level generator.

Due to the expansion we are left with a mismatch between the electroweak part, which has zero transverse momentum, and the hadronic part in which the beam functions generate emissions at a low transverse momentum q_T . Momentum is no longer conserved exactly, as illustrated in the lower left of Fig. 4.4. Given a hadronic momentum p_X^\perp due to the radiation, we define the quantity $q_\perp = -p_X^\perp$, that we parametrize as

$$q_\perp^\mu = (0, q_T \cos \phi, q_T \sin \phi, 0). \quad (4.5)$$

We now boost the entire tree-level event such that its total transverse momentum becomes q_\perp^μ (for details see B.4). While the total cross section is invariant under this transformation, the tree-level process now has two incoming partons with small transverse momenta. In our reweighting, we use the parton kinematics before the boost to determine the momentum fractions ξ_1 and ξ_2 for the beam functions. Doing so, we again neglect small momentum components. The electroweak final state however now has the correct transverse momentum, as represented in the lower right of Fig. 4.4. This procedure allows us to access to the transverse-momentum distribution of the individual final state particles.

Another procedure to consider the recoil effects was proposed by S. Catani et. al. in [23]. The authors suggest a Lorentz transformation of the colliding parton momenta from the hadronic collision frame to a specified vector boson rest frame. For dilepton production involving parton momenta k_{iT} , the constraint $q_T = k_{1T} + k_{2T}$ provides a class of consistent q_T -recoil prescriptions, the choice $k_{1T} = k_{2T} = q_T/2$ corresponding to the Collins-Soper rest frame for the vector boson. The different schemes for implementing recoil effects differ by terms suppressed by the small quantity q_T^2/Q^2 in which we expand. These power suppressed terms are not captured by our resummation formula, but we will match to fixed-order results to account for their effects up to $\mathcal{O}(\alpha_s)$.

In summary, we modify the tree-level events such that recoil effects are no longer neglected. The events are boosted to a frame in which they have momentum q_T in the transverse plane. In this way we take into consideration the transverse momentum due to the emissions. Due to momentum conservation, also the decay products are provided with transverse momentum, and their q_T -spectra become accessible.

4.3 The Art of Physics: Matching to Fixed Order

Once more we recall that our result is based on the small expansion parameter $\lambda = q_T/M$ and therefore holds for small values of q_T . Logarithms which arise at small transverse momentum are resummed, while contributions which are suppressed by powers of q_T^2/Q^2 are expanded away. At larger transverse momentum these contributions become more and more relevant and should be included.

For large q_T -values we therefore want to recover the fixed-order result. The fixed-order cross section relies on a series expansion in the strong coupling α_s . For large momentum transfer Q , the interaction is feeble and the coupling α_s small – a property referred to as *asymptotic freedom*. The result at fixed order is therefore well suited for large values of q_T . The resummed and fixed-order calculations can be matched at intermediate values of q_T to achieve uniform accuracy for the entire range of transverse momenta. One could be tempted to combine our resummed result with the fixed-order result by simply adding the two results,

$$\left. \frac{d\sigma^{\text{NNLL}}}{dq_T} \right|_{\text{combined}} \simeq \frac{d\sigma^{\text{NNLL}}}{dq_T} + \frac{d\sigma^{\text{NLO}}}{dq_T}. \quad (4.6)$$

The first term on the right-hand side is the resummed result and the second term the fixed-order NLO-result obtained from the event generator MG5_aMC@NLO. The labelling of fixed-order results is not uniform in the literature. We use the term NLO to denote the $\mathcal{O}(\alpha_s)$ result, such that the LO prediction is a δ -function term at $q_T = 0$. But this amounts to double counting some of the contributions. To correct for this, we therefore need to subtract the NLO-contribution of the resummed result. The NLO-expansion of the resummed cross section is computed in A.6. After this step, the matched cross section reads

$$\left. \frac{d\sigma^{\text{NNLL}}}{dq_T} \right|_{\text{matched to NLO}} = \frac{d\sigma^{\text{NNLL}}}{dq_T} + \underbrace{\frac{d\sigma^{\text{NLO}}}{dq_T} - \left. \frac{d\sigma^{\text{NNLL}}}{dq_T} \right|_{\text{exp. to NLO}}}_{\text{matching correction } \Delta\sigma}. \quad (4.7)$$

The third term on the right-hand side of (4.7) is the resummed result expanded to NLO. The combination of the second and third term is called the matching correction $\Delta\sigma$. The result of this matching procedure, which we will call naive matching, is shown in Fig. 4.5. While formally correct, the matched result (4.7) suffers from two problems. First of all, we do not recover the pure fixed-order result, even at very large q_T , because the resummed result includes higher-order terms in α_s . Formally they are beyond the accuracy of the computation and can be kept, but since they are based on the $q_T \rightarrow 0$

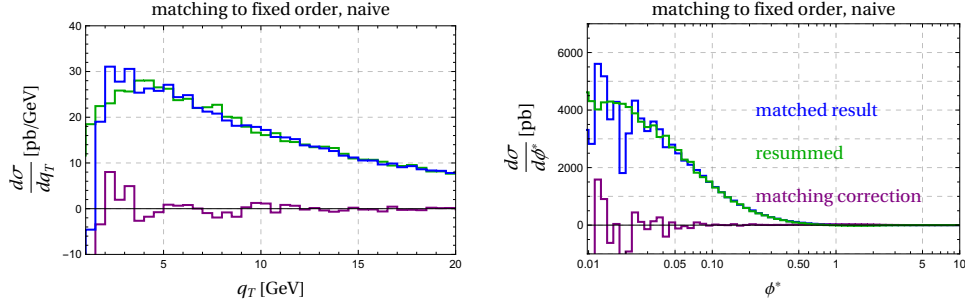


FIGURE 4.5: Matching correction, resummed, and matched result for q_T and ϕ^* , for the Z -production process featured in Section 6.2.

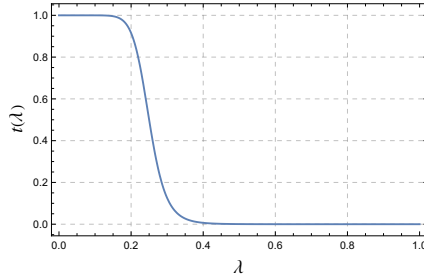


FIGURE 4.6: Transition function $t(\lambda)$ used to switch off the resummation.

limit, they can induce unphysical behavior at large q_T . Indeed, naively keeping those terms one ends up with a negative cross section at $q_T \gtrsim Q$.

The second problem concerns the other end of the spectrum. Both the fixed-order result and the NLO expansion diverge for $q_T \rightarrow 0$. The difference goes to zero, but numerically the cancellation is imperfect which leads to large numerical noise, well visible in Fig. 4.5, which renders the matched result useless for very small q_T . The numerical problems are especially visible because the resummed leading-power cross section is suppressed for very small q_T . The matching correction is not needed in this region. Because it contains unresummed large logarithms, it can even be problematic to include it. In the following, we will improve our matching scheme to solve both of the above problems.

To eliminate the numerical noise at small q_T , we switch off the matching correction for very low $q_T < q_0$, where q_0 is a cutoff of the order of a few GeV. The cutoff q_0 is chosen large enough to avoid the numerical noise from the incomplete cancellation and small enough that the neglected matching correction, which parametrically scales as q_0^2/Q^2 , lies within the scale uncertainty of the resummed result. Both conditions are fulfilled for the choice $q_0 = 5 \text{ GeV}$, which we adopt as our default value.

To avoid unphysical behavior stemming from higher-order terms in α_s of the resummed result, we switch off the resummation at large q_T . To achieve this we introduce a transition function

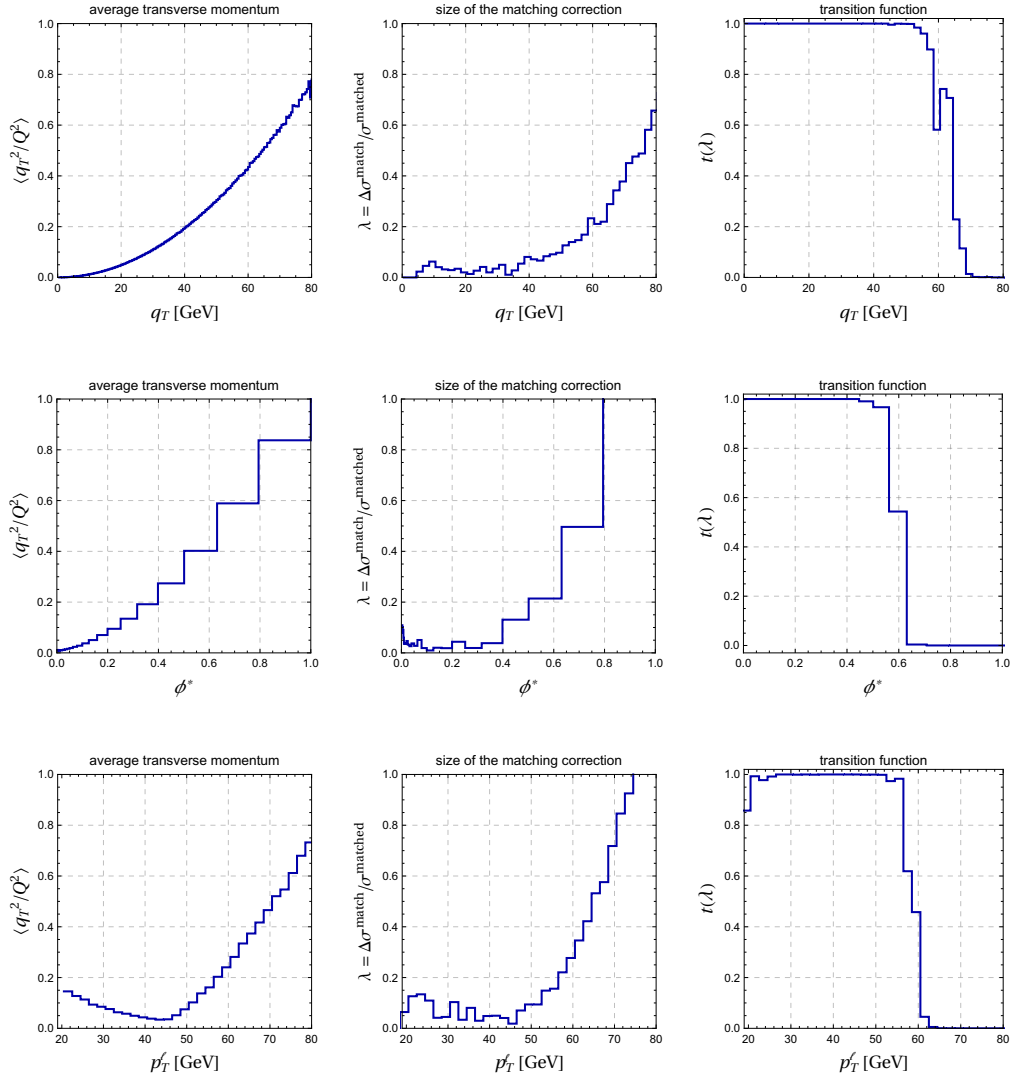


FIGURE 4.7: Average transverse momentum, size of the matching correction and transition function for the observables q_T , ϕ^* and p_T^ℓ for the Z -production process featured in Section 6.2.

$$t(\lambda) := \frac{1}{1 + a \lambda^{C_i b}}, \quad (4.8)$$

with $\lambda = \Delta\sigma/\sigma^{\text{matched}}$, where $\Delta\sigma$ is the matching correction and σ^{matched} the naively matched cross section (4.7). We use $a = 4$, $b = 8$ and $C_i = C_F = 4/3$ for the quark induced processes discussed here. The resulting functional form is plotted in Figure 4.6. The plot shows that we start switching off the resummation when the matching correction amounts to around 20% of the result and switch it off completely once it is larger than 40% of the matched cross section.

The improved matching scheme now reads

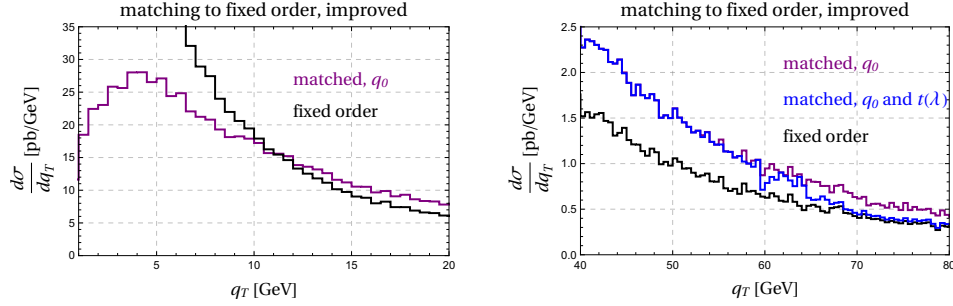


FIGURE 4.8: Improved matching for q_T , according to (4.9) for the Z -production process featured in Section 6.2. The purple curve shows the matching with a cutoff $q_T > q_0$ and the blue curve also includes the transition function $t(\lambda)$ which becomes active for $q_T \gtrsim 50$ GeV.

$$\left. \frac{d\sigma^{\text{NNLL}}}{dq_T} \right|_{\text{matched to NLO}} = t(\lambda) \left(\frac{d\sigma^{\text{NNLL}}}{dq_T} + \Delta\sigma \Big|_{q_T > q_0} \right) + (1 - t(\lambda)) \frac{d\sigma^{\text{NLO}}}{dq_T}. \quad (4.9)$$

For low values of q_T , the function $t(\lambda)$ equals 1 up to power corrections. Expression (4.7) is hence reproduced up to the fact that the matching is switched off at very small $q_T < q_0$. For large values of q_T , we have $t(\lambda) \rightarrow 0$ so that the first term vanishes and we go back to the fixed-order result.

There are various other prescriptions to switch off resummation. An advantage of working with a transition function is that this approach is simple and transparent. In [23] the transition to fixed order was based on the value of q_T . Using instead the size of the power corrections as a measure is useful because it immediately generalizes to other observables such as ϕ^* or the lepton energy distribution.

In Figure 4.7 we plot the expectation value $\langle q_T^2/Q^2 \rangle$, evaluated with the resummed cross section before matching, the size of the matching correction and the value of the transition function for q_T , ϕ^* and p_T^ℓ , the lepton energy distribution. One observes that there is a good correlation between the quantity λ , which tracks the size of the power corrections, and the expectation value $\langle q_T^2/Q^2 \rangle$ in the region of low transverse momentum. Some care is required when computing expectation values using the resummed events since the resummed cross section becomes negative at large $q_T \gtrsim Q$, where the formalism is not valid. This unphysical behavior would lead to a negative value for the expectation value $\langle q_T^2/Q^2 \rangle$ at large values of ϕ^* . To avoid this, we exclude the events with negative cross section when computing the expectation values shown in Figure 4.7. While the expectation value $\langle q_T^2/Q^2 \rangle$ and λ lead to similar behavior, we prefer to use λ since it does not require any additional computations beyond the ingredients of (4.9).

In Figure 4.8, we show the matched result based on the improved formula (4.9). One observes that the numerical noise at small q_T is gone. The right plot in the same figure shows the transition from the resummed result to the fixed-order case which takes place between q_T values of 50 – 70 GeV.

4.4 Sampling of q_T -values

For the resummation procedure we need to generate a sample of events with different transverse momenta. The most natural way of doing this would be to distribute the events according to the cross section, i.e. to compute

$$z = \Sigma(q_T) = \int_0^{q_T} dq'_T \frac{1}{\sigma} \frac{d\sigma}{dq'_T}. \quad (4.10)$$

Inverting this relation one obtains $q_T(z)$ and one then uses a random number $z = 0 \dots 1$ to generate q_T values. Proceeding in this way would yield events with equal weight, but one would obtain only few events at larger q_T where the cross section is small. In order to have a sample which also covers the region of larger q_T values, we instead generate weighted events by sampling the q_T values uniformly, i.e. we generate a random number z and set

$$q_T = z q_{\max} \quad (4.11)$$

Imposing a maximum q_T value is necessary because the resummed result for the cross section becomes unphysical at large values $q_T \gtrsim Q$. Writing $\Delta q = dq_T/dz = q_{\max}$, the cross section integral takes the form

$$\sigma_{\text{fid}} = \int_0^{q_{\max}} dq_T \frac{d\sigma}{dq_T} = \int_0^1 dz \Delta q \frac{d\sigma}{dq_T}. \quad (4.12)$$

In a MC evaluation of the last integral with N events, each event thus contributes a weight

$$w = \frac{1}{N} \frac{\Delta q}{\sigma_{\text{fid}}} \frac{d\sigma}{dq_T} \quad (4.13)$$

or equivalently, we can assign a cross section

$$\Delta\sigma = \frac{\Delta q}{N} \frac{d\sigma}{dq_T} \quad (4.14)$$

to each event. In the practical implementation, we start with MG5_aMC@NLO tree-level events, generate q_T and a random angle $\phi \in (0, 2\pi)$ to obtain the transverse momentum vector. Then we boost the event as discussed in 4.2 and compute the event weight.

Chapter 5

Implementation of the Method

Now that the factorization formula (2.56) has been derived, its components have been mathematically worked out (Chapter 3) and methodical refinements have been illustrated (Chapter 4), this chapter is dedicated to the automatisisation of the calculations. Our method is implemented using a *universal* reweighting code in combination with the event generator MG5_aMC@NLO [24] and a *process-specific* analysis code. Section 5.1 is focussed on the reweighting code, which is universal in the sense that it can be applied to arbitrary quark-induced electroweak boson production processes with or without subsequent leptonic decay, for example

$$\begin{aligned} pp \rightarrow Z & \quad \text{and} \quad pp \rightarrow Z \rightarrow l_+ l_- \\ pp \rightarrow W^+ \rightarrow l_+ \nu & \quad \text{and} \quad pp \rightarrow W^- \rightarrow l_- \nu, \\ pp \rightarrow W^+ Z & \quad \text{and} \quad pp \rightarrow W^+ Z \rightarrow l_+ l_+ l_- \nu \\ pp \rightarrow W \rightarrow HW & \quad \text{and} \quad pp \rightarrow Z \rightarrow HZ. \end{aligned} \tag{5.1}$$

With the analysis code illustrated in Section 5.2, one can choose the observables to be analysed, e.g. q_T or ϕ^* , impose the relevant experimental cuts, such as the transverse momentum and rapidity cuts ATLAS imposes on the leptons, and fill a set of histograms for the observable under consideration, containing the resummed result as well as its NLO expansion for different scale choices. These histograms may then be combined with experimental data. The use of the codes is explained step by step in Section 5.3, and methods to match the results to fixed order and compare them to experimental data are outlined in Section 5.4.

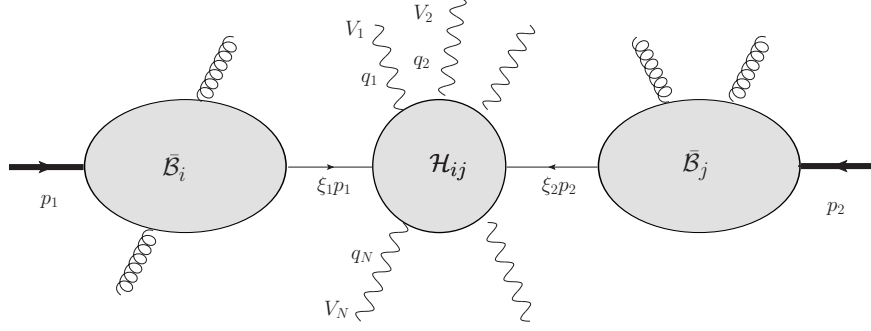


FIGURE 5.1: Structure and kinematics of the factorization theorem for boson production. The wavy lines denote the electroweak bosons in the final state.

5.1 Dressing LO Events with NLO and NNLL Contributions

5.1.1 Generating Tree-Level Events with an Event Generator

Our considerations so far were related to the production of single bosons and their leptonic decay. The underlying factorization formula includes process-specific parts, such as the hard function to one loop, and universal parts, such as the radiation of the interacting quarks. In order to generate arbitrary electroweak states like the ones listed in (5.1), we make use of MG5_aMC@NLO to compute the process-specific parts of the resummed cross section and supply it with the universal ingredients needed to achieve the resummation.

We choose a process and generate tree-level events with MG5_aMC@NLO. This results in a Les Houches Event File (LHEF) [25] containing kinematics and the leading-order cross section

$$d\sigma^{\text{LO}} = \int_0^1 d\xi_1 \int_0^1 d\xi_2 \sum_{ij \in \{\bar{q}, q\}} d\sigma_{ij}^0 \phi_i(\xi_1, \mu) \phi_j(\xi_2, \mu) \quad (5.2)$$

for each event. Here, $d\sigma_{ij}^0(\hat{p}_1, \hat{p}_2, q_1, \dots, q_N)$ is called the *partonic* cross section. For the scattering process studied in Section 1.7, the Born-level cross section was given in (1.6). Because we are no longer limited to the production of single bosons, the momentum q in our formulas gets replaced by $q_1 + q_2 + \dots + q_N$ for N bosons in the intermediate or the final state. This situation is illustrated in Fig. 5.1.

5.1.2 Computing the One-Loop Corrections for the Hard Function

The one-loop correction to the hard function takes the form

$$\mathcal{H}_{q\bar{q}}^{(1)} = -2C_F \ln^2 \left(\frac{M^2}{\mu^2} \right) + 6C_F \ln \left(\frac{M^2}{\mu^2} \right) + h_0(\hat{p}_1, \hat{p}_2, q_1, \dots, q_N). \quad (5.3)$$

For the photon-mediated process and for Z -production we have $h_0 = C_F(-16 + 7\pi^2/3)$. This quantity was computed in Section 3.1. The process-specific one-loop corrections h_0 are computed with the routine Madloop of MG5_aMC@NLO. The hard function is related to the finite part C_0 of the virtual contribution obtained from Madloop as follows,

$$h_0(\hat{p}_1, \hat{p}_2, q_1, \dots, q_N) = 2C_0(\hat{p}_1, \hat{p}_2, q_1, \dots, q_N, \mu_{\text{Mad}}) + C_F \left[\frac{\pi^2}{3} + 2 \ln^2 \frac{Q^2}{\mu_{\text{Mad}}^2} - 6 \ln \frac{Q^2}{\mu_{\text{Mad}}^2} \right], \quad (5.4)$$

where μ_{Mad} is a reference scale used by the event generator. We use a script written during earlier work on jet veto resummation [26] to compute the loop correction for each tree-level event and store this information in the eventfile.

5.1.3 Computing the Reweighting Factor

Next we run the reweighting code. The user needs to set two paths and define the range of q_T values to be considered. The maximal q_T can be chosen arbitrarily. For comparison to experimental data, the user will want to adjust the q_T range to the data provided. Our default choice for $q_{T,\text{max}}$ is around the average mass of the intermediate state, where the cross section vanishes. In a first step, the code computes an interpolation for the Q -dependent quantity q^* (3.27). The default value for the high scale $\mu_h = Q$ will be chosen dynamically for each event in the main routine based on the kinematics of the event.

In the main routine, the code executes the following steps event by event. A transverse momentum q_T and an angle ϕ are randomly generated. The entire tree-level event with four-momentum $\hat{q}^\mu = (q^0, 0, 0, q_z)$ of the intermediate state is boosted (see B.4) to transmit the recoil, see Section 4.2, such that the new coordinates are

$$q^{\mu'} = (q'_0, q_T \cos \phi, q_T \sin \phi, q'_z). \quad (5.5)$$

The flavors i and j of the incoming partons, their momentum fractions ξ_1 and ξ_2 as well as Q^2 are read from the eventfile. The quantity $q^*(\mu_h = Q)$ is obtained by numerically solving (3.27) for the given Q -value of the event using interpolation, and the factorization scale is set to $\mu = q_T + q_*$. The RG-evolved hard function \mathcal{H}_{ij} is constructed using the loop correction provided with each event and the general form of the evolution factor U . For the given value of q_T , the integrals \mathcal{M}_i are computed. We have tabulated the beam function coefficients $B_f^{(k)}$ and use a PDF code for their interpolation. The reweighting code computes the resummed cross section by assembling the mentioned quantities with the Born-level cross section and the factor for obtaining the differential cross section $d\sigma/dq_T$ from $d\sigma/dq_T^2$ emerging from the factorization formula (2.3). The cross section at q_T is obtained as a weight factor

$$w = \left(\frac{\alpha_s(\mu)}{\alpha_s(\mu_{\text{Mad}})} \right)^k \frac{\mathcal{H}_{ij}(\hat{p}_1, \hat{p}_2, q_1, \dots, q_N, \mu) \mathcal{F}_{ij}(\xi_1, \xi_2, q_T, \mu)}{\phi_i(\xi_1, \mu_{\text{Mad}}) \phi_j(\xi_2, \mu_{\text{Mad}})} w^0, \quad (5.6)$$

where w^0 is the Born weight of the tree-level event that was generated with the factorization and renormalization scales set equal to a reference value μ_{Mad} . The denominator is needed to remove the PDFs that come in via the LO cross section (5.2). Instead, we need the beam functions, given by \mathcal{F}_{ij} . The exponent k is the power of α_s of the Born level process. For the quark-induced electroweak vector-boson processes we consider here $k = 0$.

The fixed-order expansion at the scale $\mu_{\text{match}} = Q$ is also computed. All these steps are repeated under scale variation: The factorization scale μ , the high scale μ_h and the matching scale μ_{match} are varied by factors 2 and 1/2. The code then writes the boosted vectors and the weight factors back into the eventfile. The result of the reweighting is that we have a statistical ensemble of events with transverse momentum containing different weights for different scale choices.

5.2 Extracting Observables From the Reweighted Events

Our analysis code is process-specific and relies on an eventfile with reweighted events obtained by the approach presented in the previous section. At the beginning of the code, two paths need to be set. The q_T region of interest must correspond to, or lie in the range of the one chosen for the reweighting. Additionally, a cutoff value q_0 has to be defined for the matching procedure, see Section 4.3. Our default value is $q_0 = 5 \text{ GeV}$. Inside the main routine kinematical cuts and fiducial regions can be set.

Subsequently arrays are defined for the scale-varied and NLO-expanded cross sections as well as for the observables of interest. For the process $pp \rightarrow Z \rightarrow e^+ e^-$ featured in

the results Chapter 6, we choose to analyze the dilepton transverse momentum q_T , the dilepton angular observable ϕ^* and the electron transverse momentum p_T^ℓ . Arrays for histograms and event statistics are set up. The binning of the histograms can be chosen to suit the experimental data for comparison.

In the main routine we loop through the reweighted and boosted events. The event kinematics are read in for computing the observables. For those events that satisfy the imposed cuts, the cross sections are stored. An additional loop over the events that have passed the cuts serves to collect their contributions to the fiducial cross sections that are assigned to the respective bins. Further data can be collected for statistical quantities, e.g. the average value of q_T in bins of ϕ^* shown in Fig. 4.7.

The binned results are written to a textfile, and a series of plots are created that provide a first impression. After this analysis we have the resummed result, as well as its NLO expansion, for different scale choices in histogram format and ready for matching and comparing to experimental data. Note that our code produces cross sections, not spectra. If needed, we normalize our curves after the matching as a last step before comparison to experiment.

5.3 Instructions for the Use of the Reweighting and Analysis Codes

In order to use the reweighting and analysis codes, you must meet some prerequisites.

- Install MadGraph5_aMC@NLO¹.
- Install a PDF set, e.g. MMHT2014nloclas118 with LHAPDF ID 25200².
- Link the PDFs in MadGraph5_aMC@NLO.

5.3.1 Generation of Events at Tree Level

First generate the process of interest. Locate your MG5_aMC@NLO directory, open a terminal and start Madgraph by typing

```
>> ./bin/mg5_aMC
```

¹<http://www.madgraph.org/>

²<https://lhapdf.hepforge.org/pdfsets.html>

By default 4 quark flavors are activated. We work with 5 flavors, including also the b-quark. To import the 5 flavor scheme type

```
>> import model loop_sm-no_b_mass
```

Generate the process, e.g.

```
>> generate p p > Z [QCD]
```

Save the results in a new directory, e.g.

```
>> output OUT_ppZ
```

Before generating events, we need some preparations. Adjust the runcard, to be found in the process directory, `/Cards/run_card.dat`. Choose the number of events to be generated, the required accuracy as well as the collider type and energy and specify the PDF set to be used, for example:

```
lhapdf = pdlabel ! PDF set
25200 = lhaid ! If pdlabel=lhapdf, this is the lhapdf number.
```

As has been expanded on in Section 5.1, our method is based on handling single events. For each event, we want MG5_aMC@NLO to use the invariant mass Q of the final-state particles as the scale for renormalization and factorization. We therefore opt for a dynamical scale choice:

```
10 = dynamical_scale_choice ! Choose one (or more) of the predefined ...
```

In order to render the quarks massless, the ickkw parameter must be set to -1:

```
-1 = ickkw
```

Save the runcard after having made the settings. The dynamical scale choice needs to be implemented into the script `setscales.f`, to be found in the folder `/SubProcesses`. In the function `scale_global_reference(pp)` at the end of the script, the user can define the scale to be used by MG5_aMC@NLO. Define the variable `ppv` needed for summing up the contributions to the invariant mass at the beginning of the the function:

```
double precision ppv(0:3)
```

The scale must be set dynamically regardless of the value of the ickkw parameter, so replace `if(ickkw.eq.-1)then` by `if(.false.)then` at the beginning of the routine:

```
tmp=0
if (.false.) then
  tmp=ptj
...
```

At the end of the routine, define the scale by adding the following lines:

```
#####
## USER-DEFINED SCALE: ENTER YOUR CODE HERE
```

```

## to use this code you must set
## dynamical_scale_choice = 10
## in the run_card (run_card.dat)
#####
temp_scale_id='User-defined dynamical scale: mu = Q' ! use ...
tmp = 0d0
do i = 0,3
  do j = 3, nexternal-1
    ppv(i) = ppv(i) + pp(i,j)
  enddo
enddo
tmp = dsqrt(dot(ppv,ppv))
#####
##      USER-DEFINED SCALE: END OF USER CODE
#####

```

The numbering of the external particles can be checked in the Feynman diagrams in /HTML/info.html. You are now ready to generate tree-level events. Type

```
>> launch OUT_ppZ
```

Alternatively, you can locate the process directory in a terminal and type

```
>> ./bin/generate_events
```

Make sure you choose the following options in the first dialogue:

```

order = L0
fixed_order = OFF
shower = OFF
madspin = OFF
reweight = OFF

```

In the next step you have the possibility to edit the parameter card and the runcard. Unless you want to make further modifications, you can bypass this dialogue and directly press **Enter** again. The events are now generated and stored in the folder /events.lhe.gz in the directory /Events/run_01_L0. Extract the file events.lhe from this folder.

5.3.2 Virtual Corrections to the Hard Function

The leading-order cross section (5.2) is available in the eventfile. The one-loop correction factor h_0 (5.4) that includes the virtual QCD-corrections at order α_s has been

automated in MG5_aMC@NLO [26]. The relevant script is the `virt_reweighter.py` in `/Utilities/VetoPrefactors`. Move this script to the folder `/bin/internal` of the process directory.

In case the process generated has an intermediate state, the `virt_reweighter.py` must be adapted. For the example process $p p \rightarrow Z$ [QCD], this is not needed. For e.g. $p p \rightarrow Z \rightarrow e^+ e^-$, add the supplementary line `''.join('z')+ '_' + \` to the helper function `channelToShellName` at the beginning of the script:

```
# Process identified by list of PDGs to shell name mapping
def channelToShellName(in_pdgs,out_pdgs):
    return ''.join([PDGToShellName(in_pdg) for in_pdg in in_pdgs])+ '_' + \
           ''.join('z')+ '_' + \
           ''.join([PDGToShellName(out_pdg) for out_pdg in out_pdgs])
```

For the process $p p \rightarrow W^+ Z \rightarrow \mu^+ \nu e^+ e^-$ the corresponding line would read `''.join('wpz')+ '_' + \`.

Now locate the process directory and enter

```
>> cd bin/internal
>> ./virt_reweighter.py ../../Events/run_01_L0/events.lhe
```

The events are reweighted with the virtual corrections and saved as `events_rwgt.lhe`.

5.3.3 Reweighting of Events

Move the following objects to the folder `/Events/run_01_L0`:

- The python scripts `qT_reweighter.py` and `rew_functions.py`,
- the Fortran scripts `alphaS.f`, `BeamNew.f` and `mstwpdf.f`,
- the Makefile
- and the folder `Grids`.

Compile the Fortran scripts using the Makefile. The command

```
>> make
```

should return

```
>> gfortran BeamNew.f alphaS.f mstwpdf.f -o BeamNew
```

At the beginning of the script `qT_reweighter.py`, in the box `USER DEFINED SETTINGS`, insert the following information:

- The path to your MG5_aMC@NLO directory,
- the path to the process directory and
- the range of transverse momentum q_T to be considered.

The reweighting can now be accomplished by entering

```
>> python qT_reweighter.py
```

This can take considerable time, around 3 minutes for 1000, half an hour for 10'000 and one day for 500'000 events. The results are written to `events_rwgt_boost.lhe`.

5.3.4 Analysis of Events

The reweighted events can be analysed with the script `analyzer.py`. The output of the `analyzer.py` is a file named `data_hist.txt`. This file contains the resummed result, as well as its NLO expansion, for different scale choices in histogram format. To use `analyzer.py`, specify paths, the range of transverse momentum and the matching cutoff q_0 in the box `USER DEFINED SETTINGS`. Define the observables desired for analysis in the section `VARIABLES AND ARRAYS`. Set up the histograms in `ORGANIZE HISTOGRAMS`. In the part `IMPOSE CUTS` of the main routine, specify kinematical cuts and fiducial regions. For a coherent outcome, make sure the binning of the histograms and the cuts imposed correspond to the settings for the generation of fixed-order results and to the experimental data.

5.3.5 Fixed-Order Events at NLO

The resummed results can be matched to fixed-order results. The fixed-order calculation is automated in MG5_aMC@NLO as well. Use a template from the folder `/FixedOrderAnalysis` and modify it according to the process of interest: define the desired histograms as well as the binning, impose cuts on kinematic quantities and observables. For the example process `p p > Z [QCD]`, use the script `analysis_HwU_pp_V.f`. Update the fixed-order analysis card, to be found in `/Cards/FO_analyse_card.dat`, with the following lines:

```
FO_ANALYSIS_FORMAT = HwU
```

```
FO_ANALYSE = analysis_HwU_pp_V.o
```

In the runcard, to be found in `/Cards/run_card.dat`, set the `ickkw` parameter to zero:

```
0 = ickkw
```

You are now ready to generate fixed-order events. In the MG5_aMC@NLO terminal, type

```
>> launch OUT_ppZ
```

Alternatively, you can locate the process directory and type

```
>> ./bin/generate_events
```

Make sure to choose the following options in the first dialogue:

```
order = NLO
fixed_order = ON
shower = OFF
madspin = OFF
reweight = OFF
```

Then press `Enter`. You have the possibility to edit the runcard and the fixed-order analysis card. If you have already updated these cards, you can bypass this dialogue and press `Enter`. The fixed-order events are stored in the file `MADatNLO.HwU` in a new run directory `/Events/run_02`. In the files `data_hist.txt` and `MADatNLO.HwU`, data for the resummed and the fixed-order cross sections for the selected observables are now available and ready for matching. Their combination with experimental data allows for comparison of the theoretical predictions to experimental results.

5.4 Matching and Comparison to Experimental Data

We perform the matching in a separate *Mathematica*³ notebook. The different cross sections are combined step by step according to the prescription given in Section 4.3. The matching correction $\Delta\sigma$ is obtained from the NLO fixed-order result for the cross section, computed with MG5_aMC@NLO, at $q_T > q_0$. We then subtract from this the NLO-expanded resummed result imposing the same cutoff.

For the comparison to experimental data, we work with *Mathematica* as well. The ATLAS experiment uses bins of unequal size, and this can require a rebinning. For the processes featured in the results Chapter 6, we use equidistant bins for the fixed-order and the resummed data and have rebinned the experimental data. As a final step, a normalization prescription must be chosen to obtain the spectrum from the cross section. We first compute the fiducial cross section in the region $q_T \lesssim M$, the average mass of the final state, from our matched result using default scale choices and then divide by this number to get the spectrum. We also normalize the experimental result to the measured cross section in this momentum region. The upper range was chosen because

³<https://www.wolfram.com/mathematica/>

the unmatched resummed cross section turns negative at higher values of q_T which would lead to unphysical behavior in the unmatched spectra shown in Figure 6.3.

Chapter 6

Results and Discussion

I now present some computations made with our code and compare to results obtained with previous frameworks and experimental predictions. Our computations are based on version 2.6.4 of the MG5_aMC@NLO framework and unless stated otherwise, we adopt the default parameter values of this code. These include $M_Z = 91.188 \text{ GeV}$, $\alpha_s(M_Z) = 0.118$, $\alpha_{\text{EM}} = 1/132.507$, $G_F = 1.16639 \times 10^{-5} \text{ GeV}^{-2}$, and the derived quantities $M_W = 80.419 \text{ GeV}$ and $\theta_W = 0.490912$. We work with the MMHT 2014 NLO PDF set with $n_f = 5$ flavors [27]. For the hard scale, we choose the value $\mu_h = Q$, where the value of Q is set dynamically, on an event-by-event basis. For the low scale, we choose $\mu = q_T + q^*$, where q^* was defined in (3.27). In our fixed-order computations and for the matching we use $\mu_f = \mu_r = \mu_h$. To estimate the uncertainties of our computation, we individually vary the scales μ and μ_h by a factor two around their default values and take the envelope of the variations as our scale uncertainty. We found that in order to have sufficient statistics, we need to generate around 100'000 events for a q_T range of 100 GeV.

6.1 Z Boson Production

We first compare our results for the process $pp \rightarrow Z$ to those obtained with the resummation code CuTe [3] for the purpose of validation. CuTe¹ is a C++ program to calculate the differential cross-section for electroweak gauge boson and Higgs boson production at small transverse momentum q_T . The code implements NNNLL resummation as well as matching to NNLO fixed-order results and uses the LHAPDF interface to provide different PDF sets. The resummation code CuTe relies on the same theoretical foundations as the current work.

¹<https://cute.hepforge.org/>

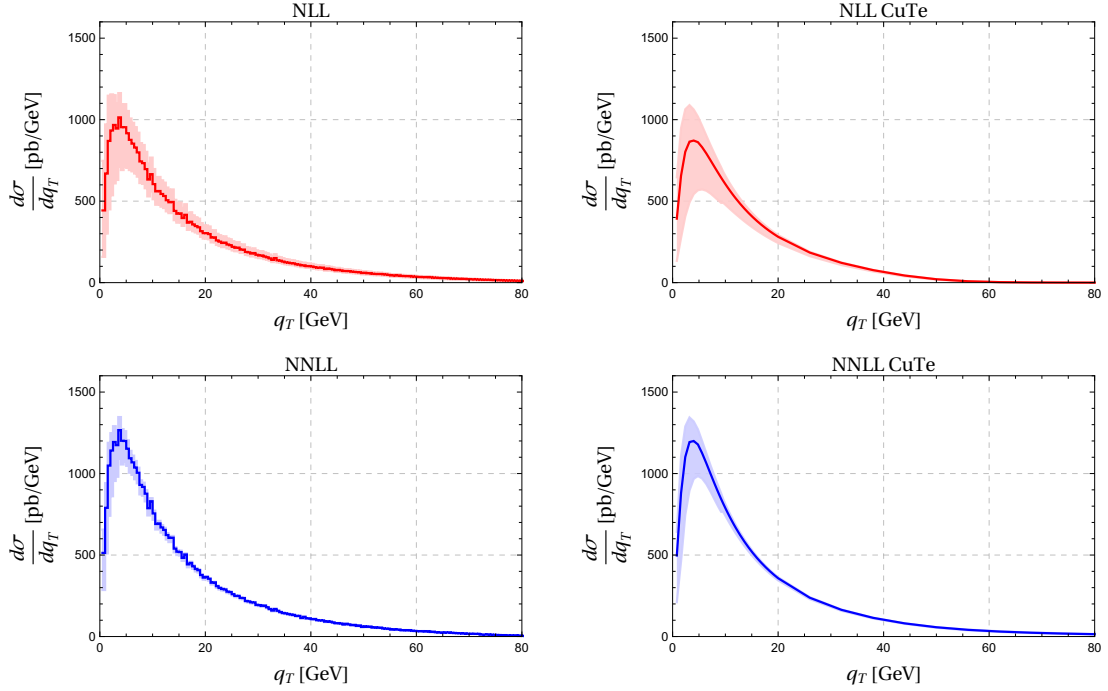


FIGURE 6.1: Comparison of the Z boson transverse momentum cross section to the result obtained with the CuTe code, with rapidity cut $|y_Z| < 2.4$.

The only selection criterion applied is to restrict the rapidity of the Z boson to $|y_Z| < 2.4$. The results for the resummed cross section are shown in Fig. 6.1. The difference in the peak region stems from the fact that in CuTe $\mu = q_T + q^* e^{-q_T/q^*}$ while in our code $\mu = q_T + q^*$. The rapidity is defined using $\tau = (M^2 + q_T^2)/s$ in CuTe, while we have $\tau = M^2/s$ (2.51). This leads to a difference for large q_T . When one adjusts these values, the results coincide exactly.

6.2 Z Boson Production and Leptonic Decay

Measurements of ϕ^* and q_T for DY events with dilepton pairs e^+e^- and $\mu^+\mu^-$ in the final state are presented in [15]. The data were collected in 2012 with the ATLAS detector in pp collisions at $\sqrt{s} = 8$ TeV, corresponding to an integrated luminosity² of 20.3 fb⁻¹. The selection criteria are listed in Table 6.1: Events were considered with transverse momentum $p_T^\ell > 20$ GeV and pseudorapidity (4.3) $|\eta| < 2.4$ for each lepton in the final state. The lepton pairs were required to have a rapidity (1.3) $|y_{\ell\ell}| < 2.4$. Our study is related to the Z -resonance region $66 \text{ GeV} < m_{\ell\ell} < 116 \text{ GeV}$.

The raw measurements are subjected to many steps of analysis before being published³. From the observed events, two cross sections are extracted. The *fiducial* cross section

²The integrated luminosity is the integral of the luminosity with respect to time.

³We use the results from the repository <https://www.hepdata.net>.

Leptons	$p_T^\ell > 20 \text{ GeV}$	$ \eta < 2.4$
Lepton pairs		$ y_{\ell\ell} < 2.4$
Mass region	$66 \text{ GeV} < m_{\ell\ell} < 116 \text{ GeV}$	

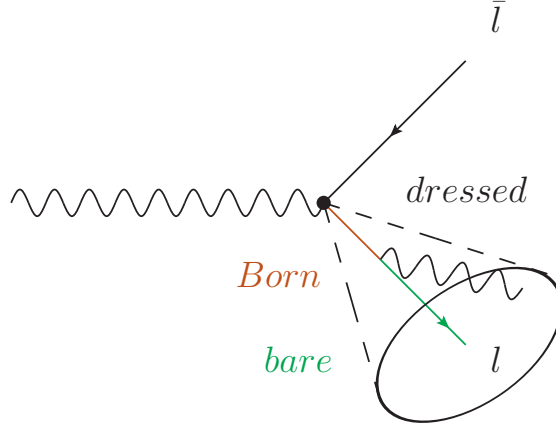
TABLE 6.1: Kinematic cuts applied for the process $pp \rightarrow Z \rightarrow e^+ e^-$.

FIGURE 6.2: Three particle-level definitions are applied to the measurements regarding lepton kinematics and final-state photon radiation: Born (red), bare (green) and dressed (black).

corresponds to the result in a region of phase-space defined by the event selection criteria. For the *total* cross section, the measured event yield must be extrapolated to the experimentally inaccessible part of the phase space. To this extent, theoretical predictions are used. The *final-state photon radiation (FSR)* is treated in three different ways named bare, dressed and Born. The lepton kinematics before FSR are called Born, those after FSR bare. The particle level called dressed is defined by combining the bare four-momentum of each lepton with that of photons radiated within a cone defined by $\Delta R = 0.1$ around the lepton, see Fig. 6.2. We perform our studies using the Born data. Monte Carlo simulation is used to estimate backgrounds and to correct the data for detector resolution and inefficiencies, as well as for the effects of FSR. The details of this analysis can be found in the reference [15].

Before confronting experiment, it is interesting to compare the resummation at NLL and NNLL order. The corresponding spectra are shown in Fig. 6.3. We observe that the scale uncertainties are reduced by about a factor two going from NLL to NNLL. The NNLL results lie within the NLL uncertainties.

In Fig. 6.4, we plot our matched results for the q_T and ϕ^* spectra, as measured by ATLAS. The scale bands are driven by the μ variation at low q_T . The μ_h variation becomes dominant at larger values when we start to switch off the resummation. The experimental data and the prediction generally agree quite well. At intermediate values we overshoot a little bit and our cross section is too small in the fixed order region at

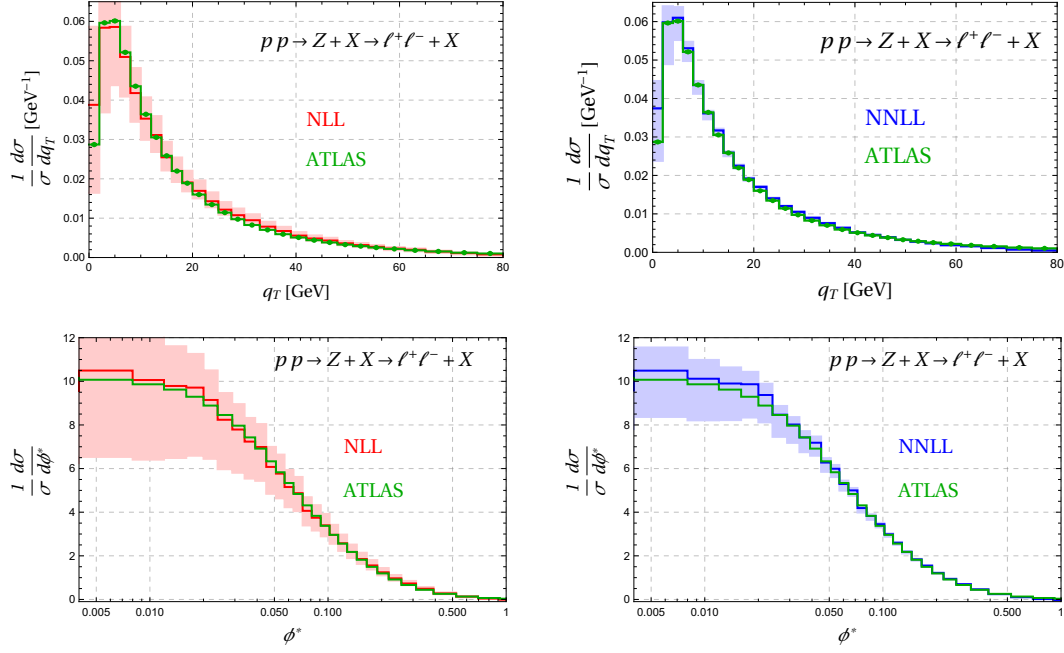


FIGURE 6.3: Comparison of the NLL (blue) and NNLL (red) results for the q_T and ϕ^* spectra. The plots show the result before matching. For visual reference, we also include ATLAS measurements (green points).

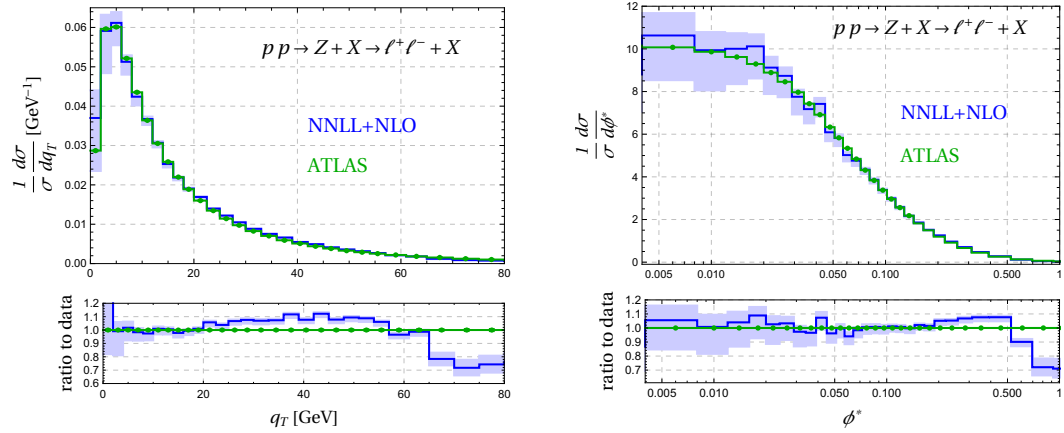


FIGURE 6.4: Comparison of the matched NNLL result to ATLAS data. The experimental uncertainties (green dots) are below 1% and thus invisibly small, the theoretical ones (blue bands) are obtained from scale variation, see text.

large q_T . Our fixed-order matching at $\mathcal{O}(\alpha_s)$ only includes the leading term for $q_T \neq 0$ and thus has limited accuracy. In the context of the fixed-order computation, let us mention that in the matching scheme (4.9) with a cutoff q_0 on the matching corrections, we could extend the matching with limited effort to $\mathcal{O}(\alpha_s^2)$. To do so, one would use MG5_aMC@NLO to perform a NLO computation of $Z + j$ with $p_T^j > q_0$, where j is a jet. The resummed results would then be expanded one order higher in α_s to extract $\Delta\sigma$.

Fig. 6.5 shows the matched result for the lepton energy distribution. Due to the lepton

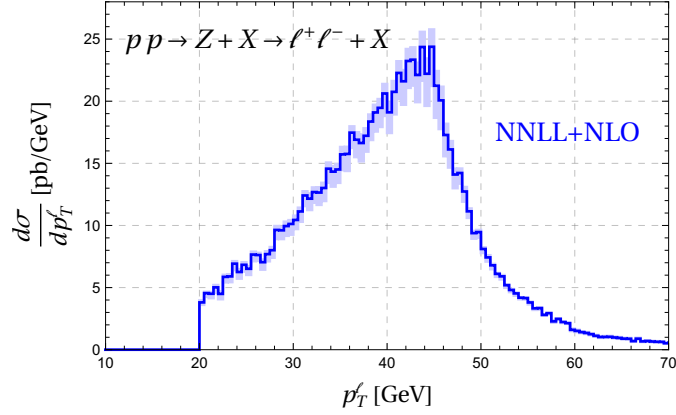


FIGURE 6.5: Matched NNLL result for the electron momentum. ATLAS imposes $p_T^e > 20$ GeV, so the distribution vanishes below this value. The bands show the scale uncertainties.

energy cut, this distribution starts at $p_T^\ell = 20$ GeV. Resummation effects are especially important near the end-point of the tree-level result at half of the mass M_V of the produced boson. Indeed for $p_T^\ell < M_V/2$, the distribution is dominated by low- q_T events, while the matching becomes important at higher values of p_T^ℓ , see Fig. 4.7. The lepton energy spectrum is much easier to measure than the transverse momentum of the weak boson, especially for the W where one has to reconstruct the missing energy to obtain the boson momentum, but to our knowledge no LHC measurements were presented for p_T^ℓ in Z production, so we cannot directly compare.

6.3 W Boson Production and Leptonic Decay

Measurements of inclusive W^+ , W^- and Z/γ^* production cross sections are presented in [28]. The data were collected in 2011 with the ATLAS detector in pp collisions at $\sqrt{s} = 7$ TeV with an integrated luminosity of 4.6 fb^{-1} . Differential W^+ and W^- cross sections were measured in a lepton pseudorapidity range $|\eta_\ell| < 2.5$ and differential Z/γ^* cross sections as a function of the absolute dilepton rapidity for $|y_{\ell\ell}| < 3.6$. In an inclusive $W \rightarrow \ell\nu$ analysis, signal events can be considered to consist of three contributions: the isolated charged lepton, the undetected neutrino, and any further particles produced in the hadronization of quarks and gluons produced in association with the W boson. The measurements provide a sensitive test of electron-muon universality in the weak interaction sector. The ratios R_W and R_Z for electronic and muonic decay were found to confirm lepton universality in the weak vector-boson decays in [28].

Our qualitative study is related to W production. We calculate the transverse momentum cross sections of the muon in $W \rightarrow \mu\nu$. Besides the figures shown in 6.6, no data

$$W \text{ decay} \quad p_T^\mu > 20 \text{ GeV} \quad |\eta_\mu| < 2.4$$

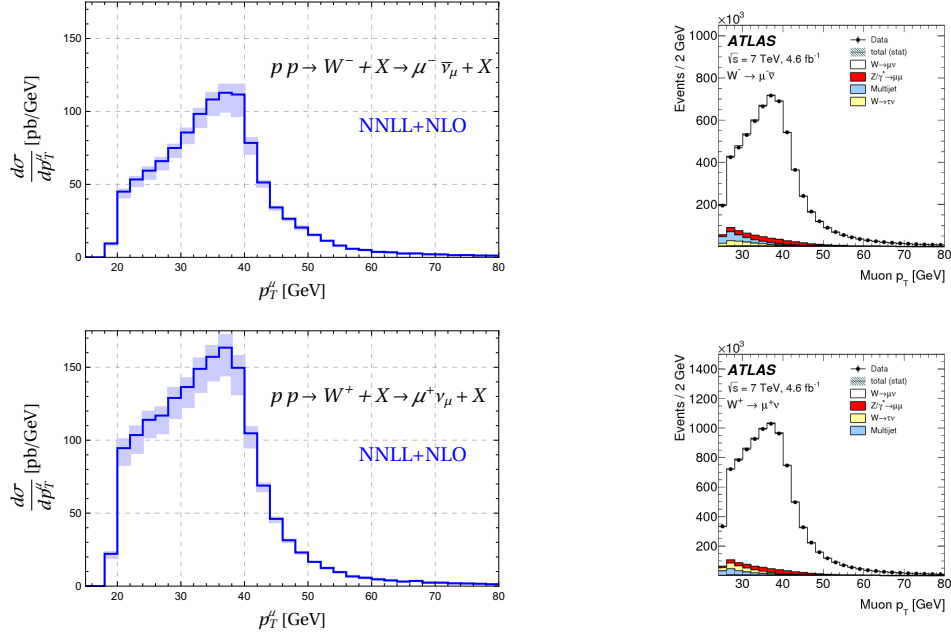
TABLE 6.2: Kinematic cuts applied for the process $pp \rightarrow W^\pm \rightarrow \mu^\pm \nu$.

FIGURE 6.6: Number of events in bins of 2 GeV for the muon p_T in $W^- \rightarrow \mu^- \bar{\nu}$ (top) and $W^+ \rightarrow \mu^+ \nu$ (bottom). Left: The muon differential cross section for the energy we obtain with our method. The bands show the scale uncertainties. Right: As measured by ATLAS [28].

on the muon spectra were published. The selection criteria applied for our qualitative study are listed in Table 6.2.

6.4 WZ Production and Triple Gauge Boson Coupling

The Standard Model predicts triple gauge boson couplings (TGCs), see Fig. 6.7. The TGC vertex is determined by the electroweak gauge structure, and it can be measured through the analysis of diboson production. A precise measurement of this vertex probes for possible new phenomena involving gauge bosons. The $W^\pm Z$ production cross section may be enhanced by anomalous TGCs deviating from gauge constraints. New particles decaying into $W^\pm Z$ pairs, such as those predicted in supersymmetric models, can also increase the cross section. An measurement sensitive to such effects has been performed at the Large Hadron Collider in 2011 [29].

The $W^\pm Z$ production cross section was measured with the ATLAS detector in pp collisions at $\sqrt{s} = 7$ TeV. Four decay channels including large missing transverse momentum were considered, namely $W^\pm Z \rightarrow e^\pm e^+ e^- \nu$, $W^\pm Z \rightarrow \mu^\pm e^+ e^- \nu$, $W^\pm Z \rightarrow e^\pm \mu^+ \mu^- \nu$ and

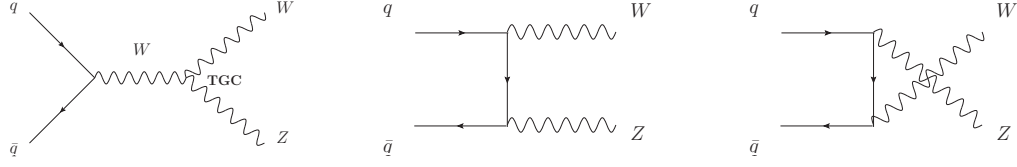


FIGURE 6.7: The SM tree-level Feynman diagrams for $W^\pm Z$ production through the s-, t- and u-channels.

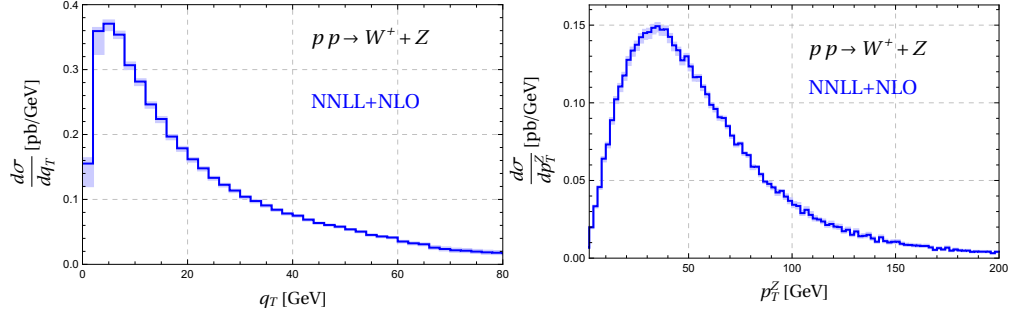


FIGURE 6.8: Matched cross sections for $W^\pm Z$ production at $\sqrt{s} = 7$ TeV. The left plot shows the total transverse momentum q_T , the right one p_T^Z , the transverse momentum of the Z boson. The bands show the scale uncertainties. The only cut we apply is to restrict the rapidity of the di-boson system to $|y| < 2.4$.

$W^\pm Z \rightarrow \mu^\pm \mu^+ \mu^- \nu$. The following selection criteria were applied: The transverse momentum of the muon must exceed 15 (18 for trigger) GeV, its pseudorapidity $|\eta| < 2.5$. For electrons, the transverse energy must be greater than 15 (22 for electron p_T trigger) GeV, while the pseudorapidity must satisfy $|\eta| < 1.37$ or $1.52 < |\eta| < 2.47$. At least one of the electrons (muons) is required to have $p_T > 20$. The dilepton invariant mass must lie within 10 GeV of the Z boson mass. Background processes for the $W^\pm Z$ signal are jets produced in association with W^\pm or Z bosons, W^+W^- and ZZ pairs as well as top-quark production events. In total, 317 candidates were observed with a background expectation of 68 ± 10 events. There were 206 W^+Z and 111 W^-Z candidates, consistent with the expectation of 186 ± 11 and 110 ± 6 , respectively. From the observed events, the fiducial and the total cross section are extracted.

We have mimicked the process by generating $pp \rightarrow W^\pm Z$ with diboson rapidity $|y| < 2.4$. The results are shown in Fig. 6.8. Plots of the Z boson transverse momentum from [29] are shown in Fig. 6.9.

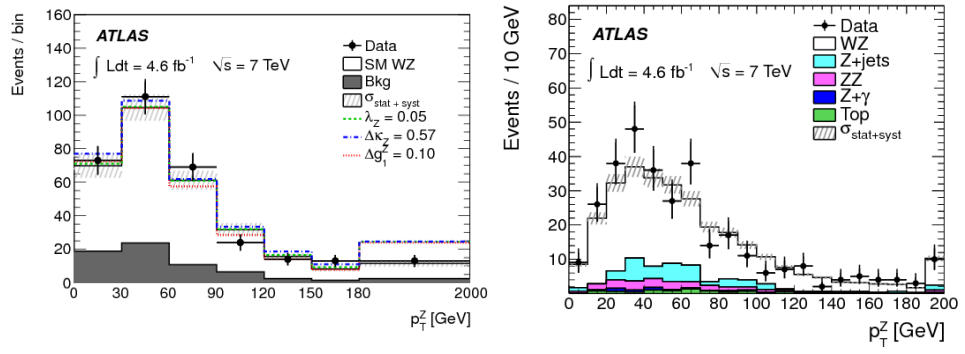


FIGURE 6.9: Visualization of Z boson transverse momentum as measured by ATLAS [29].

Chapter 7

Conclusion and Outlook

Life need not be easy, provided only
that it is not empty.

Lise Meitner, 1878-1968

I have presented and implemented a framework for transverse momentum resummation for arbitrary electroweak final states. The main points of this thesis were to explain the theoretical foundations, namely the factorization formula derived in an effective theory and the resummation technique. The implementation of the method, allowing for the automated computation of cross sections, was fleshed out in detail. Results for several observables including the variable ϕ^* were generated and discussed.

The framework is set up for arbitrary electroweak final states and has been validated carefully for Z and W boson production and leptonic decay by comparing to results obtained from existing resummation codes. It can be applied to arbitrary bosonic production processes, as was demonstrated for WZ production. Unfortunately no experimental data could be found for lepton transverse momenta. Hopefully, such results will soon be available. An interesting application is the determination of the W boson mass. The experimental analysis relies on predictions for ratios of transverse momentum spectra of different production cross sections. Our framework is suited for such tasks.

After the end of the LHC Run 2 (2015-2018) a torrent of new results is expected. Very recently, new results on boson and diboson production at $\sqrt{s} = 13$ TeV were published [30–32]. As mentioned above, our framework is suitable to compute cross sections for these processes, and they can be compared to experimental data once these become available on HEPData¹.

¹<https://www.hepdata.net>

Our framework could be extended to Higgs production. This process is gluon induced, and beyond NNLL two beam function structures arise. We have implemented the resummation at NNLL accuracy and match to fixed order at $\mathcal{O}(\alpha_s)$. For single-boson processes, the resummation can now be performed up to N³LL accuracy [33–35]. Higher accuracy in α_s requires two-loop ingredients which are not universally known, but could be implemented by hand for single-boson processes and for those double-boson processes where they are available. Furthermore, the matching could be extended to $\mathcal{O}(\alpha_s^2)$ by using MG5_aMC@NLO for an NLO computation of $Z + j$, where j is a hadronic jet. The resummed results could be expanded one order higher in α_s to extract the matching correction $\Delta\sigma$.

I am very much looking forward to applications of the framework in the Standard Model and beyond.

Appendix A

Calculations

A.1 Power counting

To find the scaling of the different fields in SCET, we compute their two-point correlators, e.g. $\langle 0 | \mathbf{T} \{ \xi(x) \bar{\xi}(0) | 0 \rangle$. Use $\gamma^{\mu\dagger} = \gamma^0 \gamma^\mu \gamma^0$, $\bar{\psi} = \psi^\dagger \gamma^0$, $\gamma^0 \gamma^0 = \mathbb{1}$ and note that $n^\dagger = n$ and $\bar{n}^\dagger = \bar{n}$ to find $\bar{\xi}$,

$$\begin{aligned} \bar{\xi} &= \overline{P_+ \psi} \propto \overline{\not{n} \not{\bar{n}} \psi} = (\not{n} \not{\bar{n}} \psi)^\dagger \gamma^0 = \psi^\dagger \not{\bar{n}}^\dagger \not{n}^\dagger \gamma^0 \\ &= \psi^\dagger \gamma^0 \gamma^\nu \gamma^0 \bar{n}_\nu \gamma^0 \gamma^\mu \gamma^0 n_\mu \gamma^0 \\ &= \bar{\psi} \bar{n}_\nu n_\mu \gamma^\nu \gamma^\mu = \bar{\psi} \not{\bar{n}} \not{n} \\ &= \bar{\psi} P_- . \end{aligned} \tag{A.1}$$

Evaluating the correlator

$$\begin{aligned} \langle 0 | \mathbf{T} \{ \xi(x) \bar{\xi}(0) \} | 0 \rangle &= P_+ \langle 0 | \mathbf{T} \{ \psi(x) \bar{\psi}(0) \} | 0 \rangle P_- \sim \not{n} \not{\bar{n}} \langle 0 | \mathbf{T} \{ \psi(x) \bar{\psi}(0) \} | 0 \rangle \not{\bar{n}} \not{n} \\ &\sim \int \frac{d^4 k}{(2\pi)^4} \frac{\not{n} \not{\bar{n}} \not{k} \not{\bar{n}} \not{n}}{k^2 + i\epsilon} e^{-ik \cdot x} \sim \lambda^4 \cdot \frac{1}{\lambda^2} \sim \lambda^2 \end{aligned} \tag{A.2}$$

reveals that $\xi \sim \lambda$. The three contributions related to the momentum in the above expression scale as $k^2 \sim \lambda^2$, $d^4 k \sim \lambda^4$ and $\not{n} \not{\bar{n}} \not{k} \not{\bar{n}} \not{n} \sim 1$. The last scaling follows from relation $n^2 = \bar{n}^2 = 0$ (2.16). Therefore $\not{n} \not{n} = n^2 = 0$ and $\not{\bar{n}} \not{\bar{n}} = \bar{n}^2 = 0$, and only the component with $\not{n} \not{\bar{n}} \not{k} \not{\bar{n}} \not{n}$ survives in the numerator,

$$\not{n} \not{\bar{n}} \not{k} \not{\bar{n}} \not{n} = \not{n} \not{\bar{n}} \left[(n \cdot k) \frac{\not{k}}{2} + (\bar{n} \cdot k) \frac{\not{k}}{2} + k_\perp^\mu \right] \not{\bar{n}} \not{n} = (\bar{n} \cdot k) \frac{\not{k}}{2} \sim 1. \tag{A.3}$$

The calculation for the η field component is identical, save for the exchange of the projection operators. The relevant term is

$$\not{n} \not{k} \not{n} \not{k} = \not{n} \not{k} \left[(n \cdot k) \frac{\not{n}}{2} + (\bar{n} \cdot k) \frac{\not{k}}{2} + \not{k}_\perp^\mu \right] \not{n} \not{k} = (n \cdot k) \frac{\not{n}}{2} \sim \lambda^2. \quad (\text{A.4})$$

The component η thus scales as λ^2 . For the soft field ψ_s we have $k^2 \sim \lambda^4$, $d^4 k \sim \lambda^8$ and $k \sim \lambda^2$, so $\psi_s \sim \lambda^3$. The correlator for the gluon field is

$$\langle 0 | \mathbf{T} \{ A^\mu(x) A^\nu(0) \} | 0 \rangle = \int \frac{d^4 k}{(2\pi)^4} \frac{i}{k^2 + i\epsilon} e^{-ik \cdot x} \left[-g^{\mu\nu} - (1 - \xi) \frac{k^\mu k^\nu}{k^2} \right], \quad (\text{A.5})$$

so each component of the gluon field scales as its momentum. For the collinear gluon field A_c^μ we have

$$n \cdot A_c \sim \lambda^2, \quad \bar{n} \cdot A_c \sim 1, \quad A_{\perp c} \sim \lambda, \quad (\text{A.6})$$

and all components of the soft field A_s^μ scale as λ^2 .

A.2 The Lagrangian of SCET

A field theory is a system with a continuous set of degrees of freedom. It can be defined in terms of a Lagrangian \mathcal{L} . The dynamics of the system are determined by the principle of least action $\frac{\delta S}{\delta \phi} = 0$, where ϕ is a field and S the action,

$$S = \int dt L = \int d^4 x \mathcal{L} \quad \text{with} \quad L = \int d^3 x \mathcal{L}. \quad (\text{A.7})$$

We remind ourselves how these concepts lead to the Euler-Lagrange¹ equations. Given a Lagrangian $\mathcal{L}[\phi, \partial_\mu \phi]$ that depends on a field ϕ and its first derivatives, we vary $\phi \rightarrow \phi + \delta\phi$, such that

$$\begin{aligned} \delta S &= \int d^4 x \left[\frac{\partial \mathcal{L}}{\partial \phi} \delta\phi + \frac{\partial \mathcal{L}}{\partial(\partial_\mu \phi)} \delta(\partial_\mu \phi) \right] \\ &= \int d^4 x \left[\frac{\partial \mathcal{L}}{\partial \phi} - \partial_\mu \frac{\partial \mathcal{L}}{\partial(\partial_\mu \phi)} \right] \delta\phi + \partial_\mu \left[\frac{\partial \mathcal{L}}{\partial(\partial_\mu \phi)} \delta\phi \right]. \end{aligned} \quad (\text{A.8})$$

¹Leonhard Euler (1707-1783) was a Swiss mathematician, physicist and astronomer. Joseph L. Lagrange (1736-1813) was a French mathematician, physicist and astronomer.

Assuming the field vanishes at temporal and spacial infinity, the last term drops out, and the Euler-Lagrange equations follow,

$$\partial_\mu \frac{\partial \mathcal{L}}{\partial(\partial_\mu \phi)} - \frac{\partial \mathcal{L}}{\partial \phi} = 0. \quad (\text{A.9})$$

Using the Euler-Lagrange equations, the equations of motions of a Lagrangian can be derived. In our case, the Lagrangian is given in (2.25), and we start with the collinear Lagrangian (2.26) that we rewrite in light cone coordinates,

$$\begin{aligned} \mathcal{L}_c &= (\bar{\xi} + \bar{\eta}) \left[i(n \cdot D) \frac{\not{n}}{2} + i(\bar{n} \cdot D) \frac{\not{n}}{2} + i\not{D}_\perp \right] (\xi + \eta) \\ &= \bar{\xi} i(n \cdot D) \frac{\not{n}}{2} \xi + \bar{\xi} i\not{D}_\perp \eta + \bar{\eta} i(\bar{n} \cdot D) \frac{\not{n}}{2} \eta + \bar{\eta} i\not{D}_\perp \xi. \end{aligned} \quad (\text{A.10})$$

In the second line we have used the relation $\not{n}\not{n} = 0 = \not{n}\not{\bar{n}}$. We solve the Euler-Lagrange equations (A.9) for $\bar{\xi}$ and $\bar{\eta}$ and find

$$(n \cdot D) \frac{\not{n}}{2} \xi = -\not{D}_\perp \eta, \quad (\bar{n} \cdot D) \frac{\not{n}}{2} \eta = -\not{D}_\perp \xi. \quad (\text{A.11})$$

Next we multiply the second line with $\not{n}/2$, solve for η and deduce $\bar{\eta}$,

$$\eta = -\frac{\not{n}}{2\bar{n} \cdot D} \not{D}_\perp \xi, \quad \bar{\eta} = -\bar{\xi} \overleftarrow{\not{D}}_\perp \frac{\not{n}}{2\bar{n} \cdot D}, \quad (\text{A.12})$$

that are now inserted into Eq. (A.10), which after the necessary transformations simplifies considerably,

$$\begin{aligned} \mathcal{L}_c &= \bar{\xi} i(n \cdot D) \frac{\not{n}}{2} \xi + \bar{\xi} i\not{D}_\perp \eta + \bar{\eta} i(\bar{n} \cdot D) \frac{\not{n}}{2} \eta + \bar{\eta} i\not{D}_\perp \xi \\ &= \bar{\xi} i(n \cdot D) \frac{\not{n}}{2} \xi - \bar{\xi} i\not{D}_\perp \frac{\not{n}}{2\bar{n} \cdot D} \not{D}_\perp \xi + \bar{\xi} \overleftarrow{\not{D}}_\perp \frac{\not{n}}{2\bar{n} \cdot D} i(\bar{n} \cdot D) \frac{\not{n}}{2} \frac{\not{n}}{2\bar{n} \cdot D} \not{D}_\perp \xi \\ &\quad - \bar{\xi} \overleftarrow{\not{D}}_\perp \frac{\not{n}}{2\bar{n} \cdot D} i\not{D}_\perp \xi \\ &= \bar{\xi} i(n \cdot D) \frac{\not{n}}{2} \xi - \bar{\xi} i\not{D}_\perp \frac{\not{n}}{2} \frac{1}{\bar{n} \cdot D} \not{D}_\perp \xi + \bar{\xi} \overleftarrow{\not{D}}_\perp \frac{\not{n}}{2\bar{n} \cdot D} \left[i(\bar{n} \cdot D) \frac{\not{n}}{2} \frac{\not{n}}{2\bar{n} \cdot D} - i \right] \not{D}_\perp \xi \\ &= \bar{\xi} i(n \cdot D) \frac{\not{n}}{2} \xi - \bar{\xi} i\not{D}_\perp \frac{\not{n}}{2} \frac{1}{i\bar{n} \cdot D} i\not{D}_\perp \xi + \bar{\xi} \overleftarrow{\not{D}}_\perp \frac{\not{n}}{2\bar{n} \cdot D} [iP_+ - i] \not{D}_\perp \xi \\ &= \bar{\xi} \left[i(n \cdot D) + i\not{D}_\perp \frac{1}{i\bar{n} \cdot D} i\not{D}_\perp \right] \frac{\not{n}}{2} \xi. \end{aligned} \quad (\text{A.13})$$

In the second last line we have inserted a factor $i/i = 1$ in the second term. The last line follows using $(P_+)^2 = P_+$, and the sign change in the second term stems from the permutation of \not{p} and \not{D}_\perp .

A.3 Gauge invariance and gauge transformations

A gauge theory is a field theory with a Lagrangian that is invariant under a continuous group of local transformations. These transformations form a Lie group, known as the gauge group. If the symmetry group is non-commutative, the corresponding gauge theory is non-Abelian. Quantum Chromodynamics (QCD) is the theory of strong interactions between quarks and gluons. It is a quantum field theory and as such a non-Abelian gauge theory with gauge group $SU(3)$.

When encoding the properties of physical objects and their dynamics – in our case the elementary particles as well their mutual interactions – using a Lagrangian, fields and their derivatives, it can be quite tricky to reconcile the mathematical framework with the physical degrees of freedom. We describe the massless spin 1 gluon field using a field with four components. This description is useful as it is well adapted to the formalism of relativistic physics. But gluons have only two physical polarizations, so our formalism is redundant. The following procedure has been established to deal with this situation. For fermion fields a symmetry transformation is defined that leaves the physical degrees of freedom and thus the measurable quantities of the field invariant. A gauge field is introduced which is related to the physical gauge boson of the interaction. A transformation for the gauge field is defined that includes an extra term which can be constrained for gauge fixing. Finally a covariant derivative, required to transform like the (fermion) field, is constructed. This procedure has the effect that the Lagrangian is invariant under these *gauge transformations* - the Lagrangian is *gauge-invariant*.

The gauge transformations of SCET are identical to those of QCD. But we need to respect the scalings of the fields, so each sector has its own gauge transformations. Under a *soft gauge transformation* the soft fields transform as

$$\begin{aligned} \psi_s(x) &\rightarrow V_s(x)\psi_s(x), & V_s(x) &= \exp[i\alpha_s^a(x)t^a], & \partial\alpha_s^a(x) &\sim (\lambda^2, \lambda^2, \lambda^2), \\ A_s^\mu(x) &\rightarrow V_s(x) \left[A_s^\mu(x) + \frac{i}{g}\partial^\mu \right] V_s^\dagger(x), \end{aligned} \tag{A.14}$$

and the collinear fields transform as

$$\begin{aligned}\xi(x) &\rightarrow V_s(x_-)\xi(x), \\ A_c^\mu(x) &\rightarrow V_s(x_-)A_c^\mu(x)V_s^\dagger(x_-).\end{aligned}\tag{A.15}$$

Note that $V_s(x)$ has been multipole expanded when acting on the collinear fields. For details see the corresponding expansion of $A_s(x)$ in (2.33). The soft fields do not transform under a *collinear gauge transformation*,

$$\psi_s(x) \rightarrow \psi_s(x), \quad A_s^\mu(x) \rightarrow A_s^\mu(x).\tag{A.16}$$

The collinear fields transform as

$$\begin{aligned}\xi(x) &\rightarrow V_c(x)\xi(x), \quad V_c(x) = \exp[i\alpha_c^a(x)t^a], \quad \partial\alpha_c^a(x) \sim (\lambda^2, 1, \lambda), \\ A_c^\mu(x) &\rightarrow V_c(x) \left[A_c^\mu(x) + \frac{i}{g}(\partial^\mu V_c^\dagger(x)) + \frac{\bar{n}_\mu}{2}[n \cdot A_s(x_-), V_c^\dagger(x)] \right].\end{aligned}\tag{A.17}$$

A.4 Wilson lines

We consider a generic Wilson line connecting two spacetime points y and z for an Abelian theory such as QED. Under a gauge transformation $V(x) = e^{i\alpha(x)}$, the gauge field $A_\mu(x)$ transforms as $A_\mu(x) \rightarrow A'_\mu(x) = A_\mu(x) - \frac{1}{e}\partial_\mu\alpha(x)$. We now investigate how the Wilson line $[z, y]$ transforms under $V(x)$,

$$\begin{aligned}[z, y] &= \exp \left[-ie \int_C dx_\mu A^\mu(x) \right] \\ &\rightarrow \exp \left[-ie \int_C dx_\mu \left(A^\mu(x) - \frac{1}{e}\partial^\mu\alpha(x) \right) \right] \\ &= \exp \left[-ie \int_C dx_\mu A^\mu(x) + i \int_C dx_\mu \partial^\mu\alpha(x) \right] \\ &= [z, y] \exp \left[i \int_C dx_\mu \partial^\mu\alpha(x) \right].\end{aligned}\tag{A.18}$$

Now we parametrize the curve C with the variable s , $x^\mu = x^\mu(s)$, and choose $y = x(s_y)$, $z = x(s_z)$, so that

$$\begin{aligned}
\exp \left[i \int_C dx_\mu \partial^\mu \alpha(x) \right] &= \exp \left[i \int_{s_y}^{s_z} ds \frac{dx_\mu}{ds} \frac{d}{dx^\mu} \alpha(x(s)) \right] \\
&= \exp \left[i \alpha(x(s)) \Big|_{s_y}^{s_z} \right] \\
&= \exp [i\alpha(z)] \exp [-i\alpha(y)].
\end{aligned} \tag{A.19}$$

Using the fact that $V(z)$ and $[z, y]$ commute, we have

$$\begin{aligned}
[z, y] &\rightarrow [z, y] \exp \left[i \int_C dx_\mu \partial_\mu \alpha(x) \right] \\
&= \exp [i\alpha(z)] [z, y] \exp [-i\alpha(y)] \\
&= V(z)[z, y]V^\dagger(y).
\end{aligned} \tag{A.20}$$

If the path is closed, $y = z$, the Wilson line is gauge invariant. Next we show that the covariant derivative along the curve C vanishes, i.e. $\dot{x}^\mu(t)D_\mu[x(t), y] = 0$. Consider the intermediate point $x^\mu = x^\mu(t)$ and parametrize the curve C using the variable t , with $y = x(t_y)$, $z = x(t)$. Then

$$\begin{aligned}
\frac{d}{dt} \int_C dx_\mu A^\mu(x) &= \frac{d}{dt} \int_{t_y}^t dt' \frac{dx_\mu}{dt'} A^\mu(x(t')) \\
&= \frac{d}{dt} \left[F(x(t')) \Big|_{t'=t_y}^{t'=t} \right] \\
&= \frac{d}{dt} (F(x(t)) - F(x(t_y))) \\
&= f(x(t)) \\
&= \frac{dx_\mu}{dt} A^\mu(x(t)).
\end{aligned} \tag{A.21}$$

We have used $f(x(t)) = \frac{dx_\mu}{dt} A^\mu(x(t))$ and the antiderivative $F(x(t))$. So

$$\begin{aligned}
\dot{x}^\mu(t)D_\mu[x(t), y] &= \frac{dx^\mu}{dt} \left(\partial_\mu + ieA_\mu(x(t)) \right) [x(t), y] \\
&= \frac{dx^\mu}{dt} \frac{d}{dx^\mu} \exp \left[-ie \int_{t_y}^t dt' \frac{dx_\mu}{dt'} A^\mu(x(t')) \right] + ie \frac{dx^\mu}{dt} A_\mu(x(t)) [x(t), y] \\
&= -ie \left(\frac{d}{dt} \int_{t_y}^t dt' \frac{dx_\mu}{dt'} A^\mu(x(t')) \right) [x(t), y] + ie \frac{dx^\mu}{dt} A_\mu(x(t)) [x(t), y] \\
&= -ie \frac{dx_\mu}{dt} A^\mu(x(t)) [x(t), y] + ie \frac{dx^\mu}{dt} A_\mu(x(t)) [x(t), y] \\
&= 0.
\end{aligned} \tag{A.22}$$

In the non-Abelian case, the exponent is matrix-valued, and we therefore need to specify an ordering prescription. In this case, we write the Wilson line as

$$[x + s\bar{n}, x] = \mathbf{P} \exp \left[ig \int_0^s ds' \bar{n} \cdot A(x + s'\bar{n}) \right]. \quad (\text{A.23})$$

The operator \mathbf{P} indicates path ordering such that

$$\mathbf{P}[A(x)A(x + s\bar{n})] = \begin{cases} A(x + s\bar{n})A(x), & \text{for } s > 0, \\ A(x)A(x + s\bar{n}), & \text{for } s < 0. \end{cases} \quad (\text{A.24})$$

As derived in (A.20) the Wilson lines transform as

$$[x + s\bar{n}, x] \rightarrow V(x + s\bar{n})[x + s\bar{n}, x]V^\dagger(x), \quad (\text{A.25})$$

so that products of the form

$$\bar{\psi}(x + s\bar{n})[x + s\bar{n}, x]\psi(x) \quad (\text{A.26})$$

are gauge invariant. One can also work with Wilson lines that go to infinity,

$$W(x) = [x, -\infty\bar{n}] = \mathbf{P} \exp \left[ig \int_{-\infty}^0 ds \bar{n} \cdot A(x + s\bar{n}) \right], \quad (\text{A.27})$$

such that the Wilson line along a finite segment can be written as a product of two Wilson lines extending to infinity,

$$\begin{aligned} [x + s\bar{n}, x] &= W(x + s\bar{n})W^\dagger(x) \\ &= \mathbf{P} \exp \left[ig \int_{-\infty}^0 dt \bar{n} \cdot A(x + s\bar{n} + t\bar{n}) \right] \mathbf{P} \exp \left[-ig \int_{-\infty}^0 dt \bar{n} \cdot A(x + t\bar{n}) \right] \\ &= \mathbf{P} \exp \left[ig \int_0^s dt \bar{n} \cdot A(x + t\bar{n}) \right]. \end{aligned} \quad (\text{A.28})$$

The Wilson lines extending to infinity transform as follows under gauge transformations,

$$W(x) \rightarrow V(x)W(x)V^\dagger(-\infty\bar{n}). \quad (\text{A.29})$$

Considering gauge functions that vanish at infinity, $V(-\infty\bar{n}) = 1$, the combinations

$$\chi(x) = W^\dagger(x)\psi(x), \quad \bar{\chi}(x) = \bar{\psi}(x)W(x), \quad (\text{A.30})$$

are gauge invariant. It has been shown above that the covariant derivative along the curve C vanishes. In our particular case this implies that

$$\bar{n} \cdot DW(x) = 0. \quad (\text{A.31})$$

Taking into account collinear and soft gauge fields, the corresponding Wilson lines are denoted as follows,

$$\begin{aligned} W_c(x) &= \mathbf{P} \exp \left[ig \int_{-\infty}^0 ds \bar{n} \cdot A_c(x + s\bar{n}) \right], \\ S_n(x) &= \mathbf{P} \exp \left[ig \int_{-\infty}^0 ds n \cdot A_s(x + sn) \right]. \end{aligned} \quad (\text{A.32})$$

A.5 Computation of the two-loop functions $\mathcal{D}_{i \leftarrow j}(z)$

To implement the factorization formula, we need to have all components at hand in numerical form. We have chosen to tabulate the beam function coefficients $B_j^{(k)}$ (3.34) and use an existing PDF code for their interpolation. Working out the two-loop functions $\mathcal{D}_{i \leftarrow j}(z)$, corresponding to the coefficient $B_j^{(3)}$, requires an elaborate but attractive analytical calculation. I therefore evaluate one example explicitly in the following. Starting with the plus distribution I derive the needed identities. Next I show how plus distributions can be convolved. Finally I compute $\mathcal{D}_{q \leftarrow q \leftarrow g}(z)$.

The plus distribution is defined as follows:

$$\int_0^1 \left(\frac{g(z)}{1-z} \right)_+ f(z) = \int_0^1 \frac{g(z)}{1-z} (f(z) - f(1)). \quad (\text{A.33})$$

Consider the following term, needed for the Altarelli-Parisi coefficient $\mathcal{P}_{q \leftarrow q}$,

$$\begin{aligned}
\int_0^1 dz \left[\frac{1+z^2}{1-z} \right]_+ f(z) &= \int_0^1 dz \left[\frac{(1-z)^2 + 2z}{1-z} \right]_+ f(z) \\
&= \int_0^1 dz \left[1-z + \frac{2(z-1)+2}{1-z} \right]_+ f(z) \\
&= \int_0^1 dz \left[1-z-2 + \frac{2}{1-z} \right]_+ f(z) \\
&= \int_0^1 dz \left(-1-z + \frac{2}{1-z} \right) (f(z) - f(1)) \\
&= - \int_0^1 dz (1+z) f(z) + f(1) \int_0^1 dz (1+z) \\
&\quad + 2 \int_0^1 dz \left[\frac{1}{1-z} \right]_+ f(z).
\end{aligned} \tag{A.34}$$

Now use the transformation

$$\begin{aligned}
f(1) \int_0^1 dz (1+z) &= \delta(1-z) f(z) \int_0^1 dz (1+z) \\
&= \frac{3}{2} \delta(1-z) f(z),
\end{aligned} \tag{A.35}$$

resulting in

$$\left[\frac{1+z^2}{1-z} \right]_+ = -1-z + \frac{3}{2} \delta(1-z) + 2 \left[\frac{1}{1-z} \right]_+. \tag{A.36}$$

To evaluate the following expression, integrate over the logarithmic term,

$$\begin{aligned}
\int_0^1 dz \left[\frac{\ln(z)}{1-z} \right]_+ f(z) &= \int_0^1 dz \left(\frac{\ln(z)}{1-z} \right) (f(z) - f(1)) \\
&= \int_0^1 dz \left(\frac{\ln(z)}{1-z} + \frac{\pi^2}{6} \delta(1-z) \right) f(z),
\end{aligned} \tag{A.37}$$

so

$$\left[\frac{\ln(z)}{1-z} \right]_+ = \left(\frac{\ln(z)}{1-z} + \frac{\pi^2}{6} \delta(1-z) \right). \tag{A.38}$$

Finally consider

$$\begin{aligned}
 \int_0^1 dz \frac{z}{[1-z]_+} f(z) &= \int_0^1 dz \left(\frac{1}{1-z} \right)_+ g(z) \\
 &= \int_0^1 dz \frac{1}{1-z} (zf(z) - f(1)) \\
 &= \int_0^1 dz \frac{1}{1-z} ((z+1-1)f(z) - f(1)) \\
 &= \int_0^1 dz \frac{1}{1-z} (f(z) - f(1) + (z-1)f(z)) \\
 &= \int_0^1 dz \left(\frac{1}{[1-z]_+} + \frac{z-1}{1-z} \right) f(z) \\
 &= \int_0^1 dz \left(\frac{1}{[1-z]_+} - 1 \right) f(z),
 \end{aligned} \tag{A.39}$$

such that

$$\frac{z}{[1-z]_+} = \frac{1}{[1-z]_+} - 1. \tag{A.40}$$

For the products of Altarelli-Parisi distributions we will need the following convolutions,

$$\left(\frac{1}{1-z} \right)_+ \otimes \delta(1-z/u), \quad \left(\frac{1}{1-z} \right)_+ \otimes \left(\frac{1}{1-z/u} \right)_+. \tag{A.41}$$

For this purpose, consider the expression

$$f(\beta) = (1-z)^{\beta-1}, \tag{A.42}$$

that we Taylor-expand around β_0 to get

$$f(\beta) = \sum_{n=0}^{\infty} \frac{(\beta - \beta_0)^n}{n!} \frac{\ln^n(1-z)}{1-z} (1-z)^{\beta_0}. \tag{A.43}$$

Now integrate,

$$\begin{aligned}
\int_0^1 \frac{dz}{z} f(\beta) &= \sum_{n=0}^{\infty} \frac{(\beta - \beta_0)^n}{n!} \int_0^1 \frac{dz}{z} \frac{\ln^n(1-z)}{1-z} (1-z)^{\beta_0} \\
&= \sum_{n=0}^{\infty} \frac{(\beta - \beta_0)^n}{n!} \int_0^1 dz \frac{\ln^n(1-z)}{1-z} \left[\underbrace{\frac{1}{z}(1-z)^{\beta_0}}_{f(z)} - \underbrace{0}_{f(1)} \right] \\
&= \sum_{n=0}^{\infty} \frac{(\beta - \beta_0)^n}{n!} \int_0^1 \frac{dz}{z} \left(\frac{\ln^n(1-z)}{1-z} \right)_+ (1-z)^{\beta_0}.
\end{aligned} \tag{A.44}$$

Choosing $\beta_0 = 0$ we have found the relation

$$(1-z)^{\beta-1} = \frac{1}{\beta} \delta(1-z) + \sum_{n=0}^{\infty} \frac{\beta^n}{n!} \left(\frac{\ln^n(1-z)}{1-z} \right)_+. \tag{A.45}$$

The first term is needed to account for the pole at $z = 1$. The relation is readily differentiated,

$$\frac{\partial}{\partial \beta} (1-z)^{\beta-1} = \ln(1-z) (1-z)^{\beta-1} = -\frac{1}{\beta^2} \delta(1-z) + \sum_{n=1}^{\infty} \frac{n \beta^{n-1}}{n!} \left(\frac{\ln^n(1-z)}{1-z} \right)_+. \tag{A.46}$$

Now we convolve relation (A.45) with the plus distribution,

$$\begin{aligned}
\int_z^1 \frac{du}{u} \left(\frac{1}{1-u} \right)_+ (1-z/u)^{\beta-1} &= \int_z^1 du \left(\frac{1}{1-u} \right) \left[\frac{1}{u} (1-z/u)^{\beta-1} - (1-z)^{\beta-1} \right] \\
&\quad - \int_0^z du \left(\frac{1}{1-u} \right) (1-z)^{\beta-1}.
\end{aligned} \tag{A.47}$$

For the second term,

$$- \int_0^z du \left(\frac{1}{1-u} \right) (1-z)^{\beta-1} = (1-z)^{\beta-1} \ln(1-z), \tag{A.48}$$

we use the derivative (A.46). Note that

$$\begin{aligned}
 \int_z^1 du \left(\frac{1}{1-u} \right)_+ f(u) &= \int_0^1 du \left(\frac{1}{1-u} \right)_+ f(u) - \int_0^z du \left(\frac{1}{1-u} \right) f(u) \\
 &= \int_z^1 du \left(\frac{1}{1-u} \right) [f(u) - f(1)] - \int_0^z du \left(\frac{1}{1-u} \right) f(1),
 \end{aligned}
 \tag{A.49}$$

since the plus distribution is identical to the fraction itself if $z < 1$. After carrying out the integrals in (A.47), the convolutions can be computed. We see that the Delta-function in (A.45) has coefficient β^{-1} . By picking the term with the same coefficient from the solution of (A.47), we find

$$\left(\frac{1}{1-u} \right)_+ \otimes \delta(1-z/u) = \left(\frac{1}{1-z} \right)_+. \tag{A.50}$$

Analogously, by noting that the coefficient of the Plus-distribution in (A.45) has coefficient β^0 , we find

$$\left(\frac{1}{1-u} \right)_+ \otimes \left(\frac{1}{1-z/u} \right)_+ = -\frac{\pi^2}{6} \delta(1-z) - \frac{\ln(z)}{1-z} + 2 \left(\frac{\ln(1-z)}{1-z} \right)_+. \tag{A.51}$$

Using the relations above the convolutions of the AP 1-loop coefficients that are listed in B.3 can be evaluated. I now evaluate $\mathcal{D}_{q \leftarrow q \leftarrow g}(z)$ explicitly.

$$\begin{aligned}
\mathcal{D}_{q \leftarrow q \leftarrow g}(z) &= \int_z^1 \frac{du}{u} \mathcal{P}_{q \leftarrow q}^{(1)}(u) \mathcal{P}_{q \leftarrow g}^{(1)}(z/u) \\
&= 16C_F T_F \int_z^1 \frac{du}{u} \left(\frac{1+u^2}{1-u} \right)_+ \left[\left(\frac{z}{u} \right)^2 + \left(1 - \frac{z}{u} \right)^2 \right] \\
&= 16C_F T_F \int_z^1 \frac{du}{u} \left(-1 - u + \frac{3}{2} \delta(1-u) + 2 \left[\frac{1}{1-u} \right]_+ \right) \left[\left(\frac{z}{u} \right)^2 + \left(1 - \frac{z}{u} \right)^2 \right] \\
&= -16C_F T_F \underbrace{\int_z^1 du \frac{1}{u} \left[\left(\frac{z}{u} \right)^2 + \left(1 - \frac{z}{u} \right)^2 \right]}_{\text{term 1}} \\
&\quad - 16C_F T_F \underbrace{\int_z^1 du \left[\left(\frac{z}{u} \right)^2 + \left(1 - \frac{z}{u} \right)^2 \right]}_{\text{term 2}} \\
&\quad + 24C_F T_F \underbrace{\int_z^1 du \delta(1-u) \frac{1}{u} \left[\left(\frac{z}{u} \right)^2 + \left(1 - \frac{z}{u} \right)^2 \right]}_{\text{term 3}} \\
&\quad + 32C_F T_F \underbrace{\int_z^1 du \frac{1}{u} \left(\frac{1}{1-u} \right)_+ \left[\left(\frac{z}{u} \right)^2 + \left(1 - \frac{z}{u} \right)^2 \right]}_{\text{term 4}}
\end{aligned} \tag{A.52}$$

Evaluate each term separately. Terms 1 – 3 can be integrated,

$$\int_z^1 du \frac{1}{u} \left[\left(\frac{z}{u} \right)^2 + \left(1 - \frac{z}{u} \right)^2 \right] = -z^2 + 2z - \ln(z) - 1, \tag{A.53}$$

$$\int_z^1 du \left[\left(\frac{z}{u} \right)^2 + \left(1 - \frac{z}{u} \right)^2 \right] = -2z^2 + z + 2z \ln(z) + 1, \tag{A.54}$$

$$\int_z^1 du \frac{1}{u} \delta(1-u) \left[\left(\frac{z}{u} \right)^2 + \left(1 - \frac{z}{u} \right)^2 \right] = z^2 + (1-z)^2. \tag{A.55}$$

In term 4 we have

$$f(u) = \left[\left(\frac{z}{u} \right)^2 + \left(1 - \frac{z}{u} \right)^2 \right] \frac{1}{u} \tag{A.56}$$

and

$$f(1) = z^2 + (1-z)^2, \tag{A.57}$$

such that it evaluates to

$$\begin{aligned}
& \int_z^1 du \left(\frac{1}{1-u} \right)_+ \left[\left(\frac{z}{u} \right)^2 + \left(1 - \frac{z}{u} \right)^2 \right] \frac{1}{u} \\
&= \int_z^1 du \left(\frac{1}{1-u} \right) \left[\left(\frac{z}{u} \right)^2 + \left(1 - \frac{z}{u} \right)^2 - z^2 - (1-z)^2 \right] \\
&- \int_0^z du \left(\frac{1}{1-u} \right) (z^2 + (1-z)^2) \\
&= -3z^2 - 2z^2 \ln(z) + 4z + 2z \ln(z) - \ln(z) - 1 + (2z^2 - 2z + 1) \ln(1-z).
\end{aligned} \tag{A.58}$$

Collecting all terms and simplifying, we get

$$\mathcal{D}_{q \leftarrow q \leftarrow g}(z) = 16C_F T_F \left[(z^2 + (1-z)^2)^2 \ln \left(\frac{(1-z)^2}{z} \right) - 2z^2 \ln z - \frac{1}{2} + 2z \right]. \tag{A.59}$$

A.6 NLO-expansion of the resummed cross section

To expand the resummed result to NLO, we consider the leading-order approximation of \mathcal{F}_{ij} (3.34) in L_\perp , starting at $\mathcal{O}(\alpha_s)$. The relevant terms are

$$\mathcal{M}_0 B_i^{(0)} B_j^{(0)} \quad \text{and} \quad -\frac{a_s}{2} \mathcal{M}_1 \left[B_i^{(0)} B_j^{(2)} + B_i^{(2)} B_j^{(0)} \right]$$

in \mathcal{F}_{ij} and

$$-\eta L_\perp = -\frac{C_F \alpha_s}{\pi} \ln \frac{Q^2}{q_T^2} L_\perp \quad \text{and} \quad -2a_s \gamma_0^q L_\perp$$

in the exponent g_F (B.2). We use the relations [2]

$$\frac{1}{2} \int_0^\infty dx_T x_T J_0(x_T q_T) e^{-\eta L_\perp} = \frac{1}{q_T^2} \left(\frac{q_T^2}{\mu^2} \right)^\eta \frac{\Gamma(1-\eta)}{e^{2\eta\gamma_E} \Gamma(\eta)} \xrightarrow{\eta \rightarrow 0} \frac{\eta}{q_T^2} \tag{A.60}$$

and

$$\begin{aligned}
\frac{d}{d\eta} \frac{1}{2} \int_0^\infty dx_T x_T J_0(x_T q_T) e^{-\eta L_\perp} &= -\frac{1}{2} \int_0^\infty dx_T x_T J_0(x_T q_T) e^{-\eta L_\perp} L_\perp \\
&\stackrel{(A.60)}{=} \frac{1}{q_T^2}.
\end{aligned} \tag{A.61}$$

Now we can collect the contributions,

$$\begin{aligned}
\frac{1}{2} \int_0^\infty dx_T x_T J_0(x_T q_T) e^{-\eta L_\perp - 2a_s \gamma_0^q L_\perp} &= \frac{1}{2} \int_0^\infty dx_T x_T J_0(x_T q_T) e^{-\eta L_\perp} (1 - 2a_s \gamma_0^q L_\perp) \\
&= \frac{\eta}{q_T^2} + 2a_s \gamma_0^q \frac{1}{q_T^2},
\end{aligned} \tag{A.62}$$

so that

$$\mathcal{M}_0 B_i^{(0)} B_j^{(0)} = \frac{a_s}{q_T^2} \left(\Gamma_0^F \ln \frac{Q^2}{q_T^2} + 2\gamma_0^q \right) B_i^{(0)} B_j^{(0)} \tag{A.63}$$

and

$$-\frac{a_s}{2} \mathcal{M}_1 \left[B_i^{(0)} B_j^{(2)} + B_i^{(2)} B_j^{(0)} \right] = \frac{a_s}{2q_T^2} \left[B_i^{(0)} B_j^{(2)} + B_i^{(2)} B_j^{(0)} \right]. \tag{A.64}$$

For the hard function we can use the leading order result $\mathcal{H}_{ij} = 1$. The expansion of the resummed cross section for quark-induced processes and $q_T > 0$ to $\mathcal{O}(\alpha_s)$ is given by

$$\begin{aligned}
\left. \frac{d\sigma_{ij}^{\text{NNLL}}}{dq_T^2} \right|_{\text{exp. to NLO}} &= d\sigma_{ij}^0 \frac{a_s}{q_T^2} \left[\left(\Gamma_0^F \ln \frac{Q^2}{q_T^2} + 2\gamma_0^q \right) \delta(1-z_1) \delta(1-z_2) \delta_{qi} \delta_{\bar{q}j} \right. \\
&\quad \left. + \frac{1}{2} \left(\mathcal{P}_{q \leftarrow i}^{(1)} \delta(1-z_2) \delta_{\bar{q}j} + \mathcal{P}_{\bar{q} \leftarrow j}^{(1)} \delta(1-z_1) \delta_{qi} \right) \right] \phi_i(\xi_1/z_1, \mu) \phi_j(\xi_2/z_2, \mu).
\end{aligned} \tag{A.65}$$

A.7 Correlation of q_T and ϕ^*

We consider a boson with mass M and transverse momentum q_T decaying to two leptons and want to find the maximum value of ϕ^* for the leptons. For $\Delta\eta = 0$, we can parametrize this situation as

$$\begin{aligned}
q &= (\sqrt{M^2 + q_T^2}, 0, q_T, 0), \\
p_1 &= (p_T, p_T \sin \alpha, p_T \cos \alpha, 0), \\
p_2 &= (p_T, -p_T \sin \alpha, p_T \cos \alpha, 0),
\end{aligned} \tag{A.66}$$

with $\alpha = \Delta\phi/2$, such that $q = p_1 + p_2$, $q_T = 2p_T \cos \alpha$ and $\sqrt{M^2 + q_T^2} = 2p_T$. Now

$$\cos \alpha = \cos \left(\frac{\Delta \phi}{2} \right) = \frac{q_T}{\sqrt{M^2 + q_T^2}} \quad (\text{A.67})$$

and

$$\phi^* = \tan \left(\frac{\pi}{2} - \arccos \left(\frac{q_T}{\sqrt{M^2 + q_T^2}} \right) \right). \quad (\text{A.68})$$

For $q_T = 0$, we have $\Delta \phi = \pi$ and $\phi^* = 0$, and for $q_T \gg M$, $\Delta \phi = 0$ and $\phi^* \rightarrow \infty$. Expanding the right-hand side of (A.68), we find that for a given q_T

$$\phi^* \leq \frac{q_T}{M}. \quad (\text{A.69})$$

Appendix B

Ingredients for the resummed cross section

B.1 Evolution of the hard function

The evolution factor $U(\hat{s}, \mu_h, \mu)$ (3.11) needed to evolve the Wilson coefficient from a high scale $\mu_h \sim Q$ down to a low scale $\mu \sim q_T$ has the analytic form

$$U(\hat{s}, \mu_h, \mu) = e^{4C_F S(\mu_h, \mu) - 4a_\gamma(\mu_h, \mu)} \left(\frac{\hat{s}}{\mu_h^2} \right)^{-2C_F a_\Gamma(\mu_h, \mu)}, \quad (\text{B.1})$$

where $r = \alpha_s(\mu)/\alpha_s(\mu_h)$,

$$a_\gamma(\mu_h, \mu) = \frac{\gamma_0^q}{2\beta_0} \left[\ln r + \left(\frac{\gamma_1^q}{\gamma_0^q} - \frac{\beta_1}{\beta_0} \right) \frac{\alpha_s(\mu) - \alpha_s(\mu_h)}{4\pi} + \dots \right], \quad (\text{B.2})$$

$$a_\Gamma(\mu_h, \mu) = \frac{\Gamma_0}{2\beta_0} \left[\ln r + \left(\frac{\Gamma_1}{\Gamma_0} - \frac{\beta_1}{\beta_0} \right) \frac{\alpha_s(\mu) - \alpha_s(\mu_h)}{4\pi} + \dots \right], \quad (\text{B.3})$$

and

$$\begin{aligned}
S(\mu_h, \mu) = \frac{\Gamma_0}{4\beta_0^2} & \left\{ \frac{4\pi}{\alpha_s(\mu_h)} \left(1 - \frac{1}{r} - \ln r \right) + \left(\frac{\Gamma_1}{\Gamma_0} - \frac{\beta_1}{\beta_0} \right) (1 - r + \ln r) + \frac{\beta_1}{2\beta_0} \ln^2 r \right. \\
& + \frac{\alpha_s(\mu_h)}{4\pi} \left[\left(\frac{\Gamma_1\beta_1}{\Gamma_0\beta_0} - \frac{\beta_2}{\beta_0} \right) (1 - r + r \ln r) + \left(\frac{\beta_1^2}{\beta_0^2} - \frac{\beta_2}{\beta_0} \right) (1 - r) \ln r \right. \\
& \quad \left. \left. - \left(\frac{\beta_1^2}{\beta_0^2} - \frac{\beta_2}{\beta_0} - \frac{\Gamma_1\beta_1}{\Gamma_0\beta_0} + \frac{\Gamma_2}{\Gamma_0} \right) \frac{(1-r)^2}{2} \right] + \dots \right\}.
\end{aligned} \tag{B.4}$$

Here we have used the coefficients β_i of the QCD β -function, the Casimir operator $C_F = 4/3$ and the anomalous dimensions Γ_i and γ_i^q .

B.2 Exponent to absorb dependencies

Using the coefficients β_i of the QCD β -function, the anomalous dimensions Γ_i^F and γ_i^q as well as $d_2 = \left(\frac{202}{27} - 7\zeta_3 \right) C_A - \frac{56}{27} T_F n_f$, where the Casimir operators $C_A = 4$ and $T_F = 1/2$ and n_f is the number of flavors, we write the exponent $g_F(L_\perp, a_s)$ (3.22) as

$$\begin{aligned}
g_F(\eta, L_\perp, a_s) = & -[\eta L_\perp]_{\epsilon^{-1/2}} - \left[a_s (\Gamma_0^F + \eta\beta_0) \frac{L_\perp^2}{2} \right]_{\epsilon^0} \\
& - \left[a_s \left(2\gamma_0^q + \eta \frac{\Gamma_1^F}{\Gamma_0^F} \right) L_\perp + a_s^2 (\Gamma_0^F + \eta\beta_0) \beta_0 \frac{L_\perp^3}{3} \right]_{\epsilon^{1/2}} \\
& - \left[a_s \eta d_2 + a_s^2 \left(\Gamma_1^F + 2\gamma_0^q \beta_0 + \eta \left(\beta_1 + 2\beta_0 \frac{\Gamma_1^F}{\Gamma_0^F} \right) \right) \frac{L_\perp^2}{2} \right. \\
& \quad \left. + a_s^3 (\Gamma_0^F + \eta\beta_0) \beta_0^2 \frac{L_\perp^4}{4} \right]_{\epsilon} \\
& - \mathcal{O}(\epsilon^{3/2}).
\end{aligned} \tag{B.5}$$

We have used the abbreviation $a_s = \alpha_s(\mu)/4\pi$.

B.3 DGLAP splitting functions, convolutions and remainder functions

The perturbative kernels $\bar{I}_{i \leftarrow j}$ involve the Dokshitzer-Gribov-Lipatov-Altarelli-Parisi (DGLAP) splitting functions $\mathcal{P}_{i \leftarrow j}^{(1)}$, the remainder functions $\mathcal{R}_{i \leftarrow j}$ and the convolutions $\mathcal{D}_{i \leftarrow j}$ given below.

$$\mathcal{P}_{q \leftarrow q}^{(1)}(z) = 4C_F \left(\frac{1+z^2}{1-z} \right)_+, \quad \mathcal{P}_{q \leftarrow g}^{(1)}(z) = 4T_F [z^2 + (1-z)^2], \quad (\text{B.6})$$

$$\mathcal{R}_{q \leftarrow q}(z) = C_F \left[2(1-z) - \frac{\pi^2}{6} \delta(1-z) \right], \quad \mathcal{R}_{q \leftarrow g}(z) = 4T_F z(1-z), \quad (\text{B.7})$$

$$\begin{aligned} \mathcal{D}_{q \leftarrow q \leftarrow q}(z) &= 16C_F^2 \left[4 \left(\frac{\ln \frac{(1-z)^2}{z}}{1-z} \right)_+ + 3 \left(\frac{1+z^2}{1-z} \right)_+ - 4(1+z) \ln(1-z) + 3(1+z) \ln z \right. \\ &\quad \left. - 2(1-z) - \frac{9}{4} \delta(1-z) \right], \\ \mathcal{D}_{q \leftarrow g \leftarrow q'}(z) &= 16C_F T_F \left[\frac{4}{3z} + 1 - z - \frac{4z^2}{3} - 2(1+z) \ln z \right], \\ \mathcal{D}_{q \leftarrow q \leftarrow g}(z) &= 16C_F T_F \left[(z^2 + (1-z)^2) \ln \frac{(1-z)^2}{z} - 2z^2 \ln z - \frac{1}{2} + 2z \right], \\ \mathcal{D}_{q \leftarrow g \leftarrow g}(z) &= 32C_A T_F \left[(z^2 + (1-z)^2) \ln(1-z) + (1+4z) \ln z + \frac{2}{3z} + \frac{1}{2} + 4z - \frac{31z^2}{6} \right] \\ &\quad + 8\beta_0 T_F [z^2 + (1-z)^2]. \end{aligned} \quad (\text{B.8})$$

B.4 Boost

The four-momentum of the intermediate state at tree level is given by $\hat{q}^\mu = (q^0, 0, 0, q_z)$. A boost transformation, parametrized by a transverse momentum q_T and an angle ϕ leads to new coordinates $q^{\mu'} = (q'_0, q_T \cos \phi, q_T \sin \phi, q'_z)$. Conservation of momentum $\hat{q}^2 = q'^2$ is ensured by imposing

$$q_z' = q_z \quad \text{and} \quad q'_0 = \sqrt{q_0^2 + q_T^2}. \quad (\text{B.9})$$

The boost matrix for the transformation $L \hat{q}^\mu = (q'_0, q_T \cos \phi, q_T \sin \phi, q'_z)$ then reads

$$L = \begin{pmatrix} \gamma & -\beta_x \gamma & -\beta_y \gamma & 0 \\ -\beta_x \gamma & L_{xx} & L_{xy} & 0 \\ -\beta_y \gamma & L_{xy} & L_{yy} & 0 \\ 0 & 0 & 0 & 1 \end{pmatrix}, \quad (\text{B.10})$$

where

$$\begin{aligned}
\gamma &= \sqrt{\frac{1}{1 - \beta_x^2 - \beta_y^2}}, & \beta_x &= \frac{q_T \cos \phi}{\sqrt{q_0^2 + q_T^2}}, & \beta_y &= \frac{q_T \sin \phi}{\sqrt{q_0^2 + q_T^2}}, \\
L_{xx} &= 1 + \frac{\beta_x^2(\gamma - 1)}{\beta_x^2 + \beta_y^2}, & L_{yy} &= 1 + \frac{\beta_y^2(\gamma - 1)}{\beta_x^2 + \beta_y^2}, & L_{xy} &= \frac{\beta_x \beta_y(\gamma - 1)}{\beta_x^2 + \beta_y^2}.
\end{aligned} \tag{B.11}$$

Bibliography

- [1] Thomas Becher and Matthias Neubert. Drell-Yan Production at Small q_T , Transverse Parton Distributions and the Collinear Anomaly. *Eur. Phys. J.*, C71:1665, 2011. doi: 10.1140/epjc/s10052-011-1665-7.
- [2] Thomas Becher, Matthias Neubert, and Daniel Wilhelm. Electroweak Gauge-Boson Production at Small q_T : Infrared Safety from the Collinear Anomaly. *JHEP*, 02:124, 2012. doi: 10.1007/JHEP02(2012)124.
- [3] Thomas Becher, Matthias Neubert, and Daniel Wilhelm. Higgs-Boson Production at Small Transverse Momentum. *JHEP*, 05:110, 2013. doi: 10.1007/JHEP05(2013)110.
- [4] Thomas Becher, Alessandro Broggio, and Andrea Ferroglia. Introduction to Soft-Collinear Effective Theory. *Lect. Notes Phys.*, 896:pp.1–206, 2015. doi: 10.1007/978-3-319-14848-9.
- [5] K. Simonyi. Kulturgeschichte der Physik. *Edition Harri Deutsch*, ISBN 978-3-8085-5760-0: Abb. 1.1–4, Abb. 1.4–15, 2001.
- [6] T. Padmanabhan. Sleeping Beauties in Theoretical Physics. *Springer*, ISBN 978-3-319-13442-0, 2015.
- [7] <https://www.ligo.caltech.edu/gallery>.
- [8] <https://github.com/mlubej/standard model>.
- [9] A. Ariga. Cloud chamber experiment. *University of Bern*, Lab course Modern physics: Lab manual Cloud chamber, 2017.
- [10] A. Bettini. Introduction to Elementary Particle Physics. *Cambridge University Press*, ISBN 0-553-26379-X, 2008.
- [11] F. Capra. The Tao of Physics. *Bantam Books*, ISBN 0-553-26379-X: p. 211 ff., 1977.
- [12] https://en.wikipedia.org/wiki/Oort_constants.

- [13] https://en.wikipedia.org/wiki/Stern-Gerlach_experiment.
- [14] Marco Ciuchini, António M. Coutinho, Marco Fedele, Enrico Franco, Ayan Paul, Luca Silvestrini, and Mauro Valli. New Physics in $b \rightarrow s\ell^+\ell^-$ confronts new data on Lepton Universality. 2019.
- [15] Georges Aad et al. Measurement of the transverse momentum and ϕ_η^* distributions of Drell–Yan lepton pairs in proton–proton collisions at $\sqrt{s} = 8$ TeV with the ATLAS detector. *Eur. Phys. J.*, C76(5):291, 2016. doi: 10.1140/epjc/s10052-016-4070-4.
- [16] M. E. Peskin and D. V. Schroeder. An Introduction to Quantum Field Theory. *Westview Press*, ISBN 13978-0-201-50397-5: Fig. 14.2, Fig. 17.6, 1995.
- [17] M. Vesterinen and T. R. Wyatt. A Novel Technique for Studying the Z Boson Transverse Momentum Distribution at Hadron Colliders. *Nucl. Instrum. Meth.*, A602:432–437, 2009. doi: 10.1016/j.nima.2009.01.203.
- [18] Andrea Banfi, Mrinal Dasgupta, and Rosa Maria Duran Delgado. The $a(T)$ distribution of the Z boson at hadron colliders. *JHEP*, 12:022, 2009. doi: 10.1088/1126-6708/2009/12/022.
- [19] A. Banfi, S. Redford, M. Vesterinen, P. Waller, and T. R. Wyatt. Optimisation of variables for studying dilepton transverse momentum distributions at hadron colliders. *Eur. Phys. J.*, C71:1600, 2011. doi: 10.1140/epjc/s10052-011-1600-y.
- [20] Andrea Banfi, Mrinal Dasgupta, and Simone Marzani. QCD predictions for new variables to study dilepton transverse momenta at hadron colliders. *Phys. Lett.*, B701:75–81, 2011. doi: 10.1016/j.physletb.2011.05.028.
- [21] Andrea Banfi, Mrinal Dasgupta, Simone Marzani, and Lee Tomlinson. Probing the low transverse momentum domain of Z production with novel variables. *JHEP*, 01:044, 2012. doi: 10.1007/JHEP01(2012)044.
- [22] Andrea Banfi, Mrinal Dasgupta, Simone Marzani, and Lee Tomlinson. Predictions for Drell-Yan ϕ^* and Q_T observables at the LHC. *Phys. Lett.*, B715:152–156, 2012. doi: 10.1016/j.physletb.2012.07.035.
- [23] Stefano Catani, Daniel de Florian, Giancarlo Ferrera, and Massimiliano Grazzini. Vector boson production at hadron colliders: transverse-momentum resummation and leptonic decay. *JHEP*, 12:047, 2015. doi: 10.1007/JHEP12(2015)047.

- [24] J. Alwall, R. Frederix, S. Frixione, V. Hirschi, F. Maltoni, O. Mattelaer, H. S. Shao, T. Stelzer, P. Torrielli, and M. Zaro. The automated computation of tree-level and next-to-leading order differential cross sections, and their matching to parton shower simulations. *JHEP*, 07:079, 2014. doi: 10.1007/JHEP07(2014)079.
- [25] Johan Alwall et al. A Standard format for Les Houches event files. *Comput. Phys. Commun.*, 176:300–304, 2007. doi: 10.1016/j.cpc.2006.11.010.
- [26] Thomas Becher, Rikkert Frederix, Matthias Neubert, and Lorena Rothen. Automated NNLL + NLO resummation for jet-veto cross sections. *Eur. Phys. J.*, C75(4):154, 2015. doi: 10.1140/epjc/s10052-015-3368-y.
- [27] L. A. Harland-Lang, A. D. Martin, P. Motylinski, and R. S. Thorne. Parton distributions in the LHC era: MMHT 2014 PDFs. *Eur. Phys. J.*, C75(5):204, 2015. doi: 10.1140/epjc/s10052-015-3397-6.
- [28] Morad Aaboud et al. Precision measurement and interpretation of inclusive W^+ , W^- and Z/γ^* production cross sections with the ATLAS detector. *Eur. Phys. J.*, C77(6):367, 2017. doi: 10.1140/epjc/s10052-017-4911-9.
- [29] Georges Aad et al. Measurement of WZ production in proton-proton collisions at $\sqrt{s} = 7$ TeV with the ATLAS detector. *Eur. Phys. J.*, C72:2173, 2012. doi: 10.1140/epjc/s10052-012-2173-0.
- [30] Albert M Sirunyan et al. Measurements of the $pp \rightarrow WZ$ inclusive and differential production cross section and constraints on charged anomalous triple gauge couplings at $\sqrt{s} = 13$ TeV. 2019.
- [31] Morad Aaboud et al. Measurement of $W^\pm Z$ production cross sections and gauge boson polarisation in pp collisions at $\sqrt{s} = 13$ TeV with the ATLAS detector. 2019.
- [32] Morad Aaboud et al. Measurement of the four-lepton invariant mass spectrum in 13 TeV proton-proton collisions with the ATLAS detector. 2019.
- [33] Wojciech Bizon, Pier Francesco Monni, Emanuele Re, Luca Rottoli, and Paolo Torrielli. Momentum-space resummation for transverse observables and the Higgs p_\perp at N³LL+NNLO. *JHEP*, 02:108, 2018. doi: 10.1007/JHEP02(2018)108.
- [34] Wojciech Bizoń, Xuan Chen, Aude Gehrmann-De Ridder, Thomas Gehrmann, Nigel Glover, Alexander Huss, Pier Francesco Monni, Emanuele Re, Luca Rottoli, and Paolo Torrielli. Fiducial distributions in Higgs and Drell-Yan production at N³LL+NNLO. *JHEP*, 12:132, 2018. doi: 10.1007/JHEP12(2018)132.

-
- [35] Xuan Chen, Thomas Gehrmann, E. W. Nigel Glover, Alexander Huss, Ye Li, Duff Neill, Markus Schulze, Iain W. Stewart, and Hua Xing Zhu. Precise QCD Description of the Higgs Boson Transverse Momentum Spectrum. *Phys. Lett.*, B788: 425–430, 2019. doi: 10.1016/j.physletb.2018.11.037.
- [36] Thomas Becher and Monika Hager. Event-Based Transverse Momentum Resummation. 2019.

Erklärung

gemäss Art. 30 RSL Phil.-nat. 18

Name, Vorname: Hager Monika

Matrikelnummer: 90-180-374

Studiengang: Physik

Bachelor ☐ Master ☐ Dissertation ☐

Titel der Arbeit: Automated Transverse Momentum Resummation
for Electroweak Boson Production

Leiter der Arbeit: Prof. Dr. Thomas Becher

Ich erkläre hiermit, dass ich diese Arbeit selbständig verfasst und keine anderen als die angegebenen Quellen benutzt habe. Alle Stellen, die wörtlich oder sinngemäss aus Quellen entnommen wurden, habe ich als solche gekennzeichnet. Mir ist bekannt, dass andernfalls der Senat gemäss Artikel 36 Absatz 1 Buchstabe r des Gesetzes vom 5. September 1996 über die Universität zum Entzug des auf Grund dieser Arbeit verliehenen Titels berechtigt ist.

Für die Zwecke der Begutachtung und der Überprüfung der Einhaltung der Selbständigkeitserklärung bzw. der Reglemente betreffend Plagiate erteile ich der Universität Bern das Recht, die dazu erforderlichen Personendaten zu bearbeiten und Nutzungshandlungen vorzunehmen, insbesondere die schriftliche Arbeit zu vervielfältigen und dauerhaft in einer Datenbank zu speichern sowie diese zur Überprüfung von Arbeiten Dritter zu verwenden oder hierzu zur Verfügung zu stellen.

Ort, Datum

Unterschrift

Curriculum Vitae

Monika Hager

Albert Einstein Center for Fundamental Physics
Institute for Theoretical Physics
Sidlerstrasse 5, CH-3012 Bern
Switzerland
+41 31 631 86 04
Email: hager@itp.unibe.ch

Born: 07/04/1968
Citizenship: Swiss
Tellplatz 5
CH-3014 Bern
Switzerland
+41 31 351 41 64

EDUCATION AND RESEARCH**University of Bern, Switzerland**

Ph.D. in Theoretical Physics 2015 - 2019

Advisor: Prof. Dr. Thomas Becher
Thesis: Automated Transverse Momentum Resummation
for Electroweak Boson Production

Master of Science in Theoretical Physics 2013 - 2015

Advisor: Prof. Dr. Uwe-Jens Wiese
Thesis: The SU(2) Quantum Link Model

Bachelor of Science in Physics 2013 - 2015

Major: Physics *Minor:* Astronomy
Advisor Thesis: Dr. Sigve Haug
Bachelor Thesis: Audification of ATLAS Data

PUBLICATIONS

T. Becher and M. Hager, "Event-Based Transverse Momentum Resummation" [36].

Conference Talk T. Becher, M. Hager, "Event-based Transverse Momentum Resummation", SCET 2018, <https://indico.cern.ch/event/628868/contributions/2910467/>.
